A Micromechanics-Inspired Three-Dimensional Constitutive Model for The Thermomechanical Response of Shape-Memory Alloys

Thesis by

Amir Sadjadpour

In Partial Fulfillment of the Requirements

for the Degree of

Doctor of Philosophy

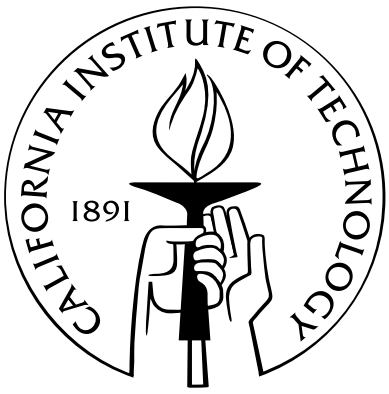

California Institute of Technology

Pasadena, California

2006

(Submitted May 01, 2006)

To Him whom I owe my whole life.

To my parents, my wife, and my two sisters.

Acknowledgements

I would like to thank my advisor, Professor Kaushik Bhattacharya, for his great support throughout the past four years of my life at Caltech. I came to Caltech as a civil engineering major and it was through Kaushik's solid mechanics course that I almost fell in love with the science of mechanics and decided to pursue my PhD in the applied mechanics department of Caltech. Kaushik's high academic standards and great vision will always be a source of inspiration to me.

I would also like to thank Professor James K. Knowles, Professor Guruswami Ravichandran and Professor Nadia Lapusta for serving in my committee. I am grateful for their support, guidance, and insight. They have been great mentors and dear friends and I wish for many more opportunities to learn from them. I am also thankful to Professor Daniel Rittel for our many interesting discussions on addressing the phase transformation in pure iron.

I have been very lucky to serve as the chairman of the graduate council of Caltech as it was through this opportunity that I became acquainted with Margo Marshak, the Vice President in student affairs. I can not put in words my sincere appreciation of her great personality, her generous support and her hearty friendship. I will always think of her so highly and send her my highest regards and wishes.

I also want to thank my past and current group members, Isaac Chenchiah, Samantha Daly, Kaushik Dayal, Patrick Dondl, Vikram Gavini, Mathias Jungen, Alex Kelly, Dnyanesh Pawaskar, Prashant Purohit, Farshid Roumi, Lixiu Tian, Yu Xiao, Arash Yavari, Ling Zheng, and Johannes Zimmer. I have learned much from all of you. Thank you!

I am also thankful for the opportunities to assist Professor David Goodwin, Pro-

fessor Nadia Lapusta, Professor Ken Pickar, Professor Niles Pierce, and Professor Vilupanur Ravi in teaching courses at Caltech. I am influenced by their knowledge, commitment and discipline.

Among many others whom I wish to thank, I particularly send my warmest regards to Jim Endrizzi, Marjory Gooding, Parandeh Kia, Cristi Maetani, and Athena Trentin who make Caltech such a pleasant environment for international students.

I would also like to thank Judy Donohue, Delores Lee, and Gaylord Nichols who run such a progressive program in Caltech's Industrial Relations Center where I obtained my management of Technology and Engineering Management certificates.

I send my warm wishes to Lynn Burgess, William Burrell, Karen Carlson, Rosa Carrasco, Suzette Cummings, Cheryl Geer, Sylvie Gertemanian, Natalie Gilmore, Jerry Houser, Maria Koeper, Tess Legaspi, Sara Loredo, Icy Ma, Linda Miranda, Carolina Oseguera, Edith Quintanilla, Christine Silva, and Angela Wood. I am quite grateful to you all and remember you.

My very special thanks goes to my parents Masoumeh Rafi and Mohammad Saeid Sadjadpour, my wife Azadeh Rassouli, my lovely sisters Maryam and Fatemeh Sadjadpour and all those with whom I have shared my life in the past five years.

In particular I would like to thank Soroush Abbaspour, Ehsan Afshari, Leila Alinaghian, Nazanin and Niaz Angoshtari, Ali Asghari, Hossein Ataei, Meher Ayalasomayajula, Monir Azarmnia, Farnoush BanaieKashani, Hajar Behzadnia, Alireza Doustan, Amir Farajidana, Marmar Ghadiri, Amin Ghaemi, Anna Grosberg, Reza JafarKhani, Mehrdad Jahangiri, MohammadReza Jahanshahi, Hao Jiang, Ehsan Kazemian, Mitra Koochmeshki, Swami Krishnan, Arash Kheradvar, Yashashree Kulkarni, Arghavan Louhghalam, Hadi Meidani, Judith Mitrani, Liza Motahari, Maziar Motahari, Arezoo Momeni, Omid Momeni, Srideep Musuvathy, Ali Nadim, Helia Naeimi, Abbas and Mahya Nasiraei, Arash Noshadravan, Tosin Otitoju, Mazdak PourAbdollah, Mahshid Rahmani, Maryam Sharif, Masoud Sharif, Mehdi Sharifzadeh, Gunjan Sukul, Shervin Taghavi, Mazhar Taghavi, Zahra Tehrani, Min Tao, Fuling Yang, and Hadi Zandi. I wish you a journey full of purpose, meaning and happiness through life. With much affection.

Abstract

The goal of this thesis is to develop a three-dimensional micromechanics-inspired constitutive model for polycrystalline shape-memory alloys. The model is presented in two forms: (1) The one-dimensional framework where we picture the ability of the model to capture the main properties of shape-memory alloys such as superelasticity and the shape-memory effect; (2) the three-dimensional model where micromechanics origins of the model, the concepts that emerged from those analyses and their relation to macroscopic properties in polycrystals are presented.

We use this framework to study the effects of the texture and anisotropy in material behavior. Since phase transformation often competes with plasticity in shape-memory alloys, we incorporate that phenomenon into our model. We also demonstrate the ability of the model to predict the response of the material and track the phase transformation process for multi-axial, proportional and non-proportional loading and unloading experiments. We consider both stress-controlled and strain-controlled experiments and develop the model for isothermal, adiabatic and non-adiabatic thermal conditions. Adiabatic heating and loading rate both lead to apparent hardening at high rates. We also visit this problem and examine the relative role of these two factors.

Finally we extend our model to study the reversible $\alpha \leftrightarrow \varepsilon$ martensitic phase transformation in pure iron. We consider a wide range of loading rates ranging from quasistatic to high rate dynamic loading and use our model to describe the evolution of the microstructure along with the effects of rate hardening and thermal softening.

Contents

Acknowledgements **iv**

Abstract **vi**

1 Introduction **1**

1.1 **Shape-Memory Alloys** 1

2 One-Dimensional Constitutive Model for Shape-Memory Alloys **13**

2.1 Constitutive Model 13

2.1.1 Kinematics 13

2.1.2 Balance laws 16

2.1.3 Constitutive relations, driving forces and kinetic relations . . . 17

2.1.4 Specific constitutive assumptions 18

2.1.5 Temperature evolution 21

2.2 Demonstration 23

2.2.1 Parameters 23

2.2.2 Superelasticity 24

2.2.3 Tension-compression asymmetry 26

2.2.4 Ambient temperature and the shape-memory effect 28

2.2.5 Effect of loading rate on the deformation behavior 34

2.2.6 Effect of plastic yield strength 38

2.2.7 Internal loops 40

2.3 Kolsky bar 42

2.3.1 Kolsky bar 42

2.3.2 Ambient temperature 45
2.3.3 Pulse amplitude, size and shape 45

3 Three-Dimensional Constitutive Model for Shape-Memory Alloys 48

3.1 Constitutive Model 48
3.1.1 Kinematics 48
3.1.2 Balance laws 49
3.1.3 Constitutive relations, driving forces and kinetic relations . . . 50
3.1.4 Set of effective transformation strains 51
3.1.4.1 Isotropic and symmetric transformation 53
3.1.4.2 Isotropic and asymmetric transformation 54
3.1.4.3 Anisotropic and asymmetric transformation 54
3.1.5 Temperature evolution 55
3.1.5.1 Adiabatic conditions 56
3.1.5.2 Non-adiabatic conditions 56
3.1.6 Critical phase transformation stress 57
3.2 Demonstration of the isotropic model 59
3.2.1 Parameters 59
3.2.2 Set of effective transformation strains 59
3.2.3 Proportional loading 63
3.2.4 Non-adiabatic conditions 65
3.2.5 Nonproportional loading 68
3.3 Demonstration of the anisotropic model 73
3.3.1 Parameters 73
3.3.2 Set of effective transformation strains 73
3.3.3 Parameter study 74
3.3.4 Stress-controlled tests 77
3.3.5 Strain-controlled tests 83
3.3.6 Effect of texture 83

4 Phase Transformation in Iron **88**

4.1 Introduction 88

4.2 Model 88

4.2.1 Johnson-Cook 89

4.2.2 Temperature evolution 91

4.2.3 Further approximation 92

4.3 Demonstration 93

4.3.1 Parameters 93

4.3.2 Fitting the model to the experiment 94

4.3.3 Strain-controlled tests 97

5 Conclusion **105**

6 Appendix A **109**

6.1 An example of a MATLAB code for the stress controlled full-dimensional analysis of anisotropic shape-memory alloys 109

List of Figures

1.1 Superelasticity 2
1.2 Austenite-martensite phase transformation 2
1.3 Shape-memory effect 3
1.4 Asymmetry 5
1.5 Rate effect 5
1.6 The effect of texture and anisotropy in stress-strain response (23). . . . 6

2.1 Schematic representation of the Helmholtz energy density. 19
2.2 The kinetic relation between $\dot{\lambda}$ and the driving force d_λ 20
2.3 Comparison between the experiment (31) and the fit to the model. . . 25
2.4 A typical stress-strain curve generated by the model. 26
2.5 Effect of the relative values of the phase transformation strains in the asymmetric response 27
2.6 The stress-strain behavior at different ambient temperatures. 29
2.7 The stress-strain behavior at different ambient temperatures. 30
2.8 The stress-strain behavior at different ambient temperatures. 31
2.9 The stress-strain behavior at different ambient temperatures. 32
2.10 The stress-strain behavior at different ambient temperatures. 33
2.11 Tensile and compressive half-cycles at different loading rates, $\omega \mapsto 0.375\omega$, 0.75ω, 1.25ω, 2.5ω, 5ω, 10ω. 35
2.12 Complete tension-compression cycles at different loading rates, $\omega \mapsto$ 0.375ω, 2.5ω, 5ω. 36

2.13 Comparison of the stress-strain relations for rate-independent (left) and rate-dependent (center) transformation kinetics. The two kinetic relations are shown on the right. 38
2.14 The effect of the power of the kinetic relation on the stress-strain response at loading rates: $\omega \mapsto 1.25\omega, 2.5\omega, 5\omega, 7.5\omega, 10\omega$ for an isothermal condition. 39
2.15 The effect of the power of the kinetic relation on the stress-strain response at loading rates: $\omega \mapsto 1.25\omega, 2.5\omega, 5\omega, 7.5\omega, 10\omega$ for an adiabatic condition. 39
2.16 The stress-strain relations at different yield strength. 40
2.17 The internal hysteresis loops. 41
2.18 Kolsky bar and time-space diagram. 42
2.19 The effect of ambient temperature on stress-strain response. 45
2.20 Pulse amplitude's effect in stress-strain hysteresis. The amplitude and pulse duration are normalized with those described in (2.64). 46
2.21 Pulse duration's effect in stress-strain hysteresis. The amplitude and pulse duration are normalized with those described in (2.64). 46
2.22 The effect of the pulse shape in stress-strain hysteresis. The amplitude and pulse duration are normalized with those described in (2.64). . . . 46
2.23 Design of the strain rate in the specimen. 47

3.1 Initiation of the forward martensitic phase transformation. 57
3.2 Parameter study on the effect of parameter a on the shape of the phase transformation surface. 60
3.3 Parameter study on the effect of parameters a and b on the shape and size of the phase transformation surface. 61
3.4 Phase transformation surfaces of Ni-Ti in stress and strain space. . . . 63
3.5 Uniaxial tension-compression stress-strain curves under proportional loading. 64
3.6 Pure shear stress-strain curves under proportional loading. 64

3.7 Biaxial proportional tension-compression loading of Ni-Ti. 65
3.8 Non-adiabatic conditions. 66
3.9 Non-adiabatic conditions. 67
3.10 Nonproportional stress-controlled test. 69
3.11 Nonproportional stress-controlled test. 70
3.12 Nonproportional stress-controlled test. 71
3.13 Nonproportional stress-controlled test. 72
3.14 The effect of parameter c on the shape of the transformation surface. . 75
3.15 The effect of parameter a on the shape of the transformation surface. . 75
3.16 The effect of parameter c on the shape of the transformation surface. . 76
3.17 The effect of parameter a on the shape of the transformation surface. . 76
3.18 Stress-controlled behavior of an anisotropic NiTi polycrystalline: profile I. 78
3.19 Stress-controlled behavior of an anisotropic NiTi polycrystalline: profile II. 79
3.20 Stress-controlled tension-torsion simulation and the corresponding strain path of an anisotropic NiTi polycrystalline: profile I - Path 1. 80
3.21 Stress-controlled tension-torsion simulation and the corresponding strain path of an anisotropic NiTi polycrystalline: profile I - Path 2. 80
3.22 Stress-controlled tension-torsion simulation and the corresponding strain path of an anisotropic NiTi polycrystalline: profile I - Path 3. 81
3.23 Stress-controlled tension-torsion simulation and the corresponding strain path of an anisotropic NiTi polycrystalline: profile I - Path 4. 81
3.24 Stress-controlled tension-torsion simulation and the corresponding strain path of an anisotropic NiTi polycrystalline: profile I - Path 5. 81
3.25 Stress-controlled tension-torsion simulation and the corresponding strain path of an anisotropic NiTi polycrystalline: profile I - Path 6. 82
3.26 Stress-controlled tension-torsion simulation and the corresponding strain path of an anisotropic NiTi polycrystalline: profile I - Path 7. 82
3.27 Strain-controlled behavior of an anisotropic NiTi polycrystalline: profile I. 84

3.28 Strain-controlled behavior of an anisotropic NiTi polycrystalline: profile II. 85
3.29 Rolled sheet under tensile stress 85
3.30 Analytical model v.s. experiment, PL-CR ($\{1\,1\,1\}< u\,v\,w >$ texture). . 86
3.31 The recoverable torsion vs. the recoverable extension in NiTi polycrystals with isotropic fiber textures. 87

4.1 Strain rate dependence of the flow stress. 90
4.2 Schematic representation of the S function. 91
4.3 Quasistatic stress-strain response of pure iron. 94
4.4 Flow stress dependence on strain rate. 95
4.5 Temperature dependence of the yield stress. 96
4.6 Schematic contribution of plastic work in generating heat as a function of strain and strain rate. 97
4.7 stress-strain response of pure iron for a quasistatic test. 99
4.8 stress-strain response of pure iron for a dynamic test, $\dot{\varepsilon} = 2800(\frac{1}{s})$. . . 99
4.9 stress-strain response of pure iron for a dynamic test, $\dot{\varepsilon} = 5800(\frac{1}{s})$. . . 100
4.10 stress-strain response of pure iron for a dynamic test, $\dot{\varepsilon} = 8400(\frac{1}{s})$. . . 100
4.11 stress-strain response of pure iron for a dynamic test, $\dot{\varepsilon} = 3500(\frac{1}{s})$. . . 101
4.12 stress-strain response of pure iron for a dynamic test, $\dot{\varepsilon} = 6300(\frac{1}{s})$. . . 101
4.13 stress-strain response of pure iron for a dynamic test, $\dot{\varepsilon} = 9500(\frac{1}{s})$. . . 102
4.14 stress-strain response of pure iron for a dynamic test, $\dot{\varepsilon} = 10,000(\frac{1}{s})$. . 102
4.15 Phase transformation growth and temperature profile of pure iron for different strain rate experiments. 103

Chapter 1

Introduction

1.1 Shape-Memory Alloys

Shape-memory alloys are widely used for a variety of applications including micro-actuators, cell phone antennas, energy absorption and biomedical devices. These materials exhibit a strongly nonlinear thermomechanical behavior associated with abrupt changes in their lattice structure called martensitic phase transformation. Two common manifestations of this phase transformation is the *shape-memory effect* wherein an apparently plastic deformation sustained below some critical temperature is recovered on heating above it, and *superelasticity* wherein significant deformations suffered under loading are recovered on unloading. A typical example of the superelastic stress-strain response of a shape-memory alloy is shown in Figure 1.1. (see (35))

The shape-memory effect and superelasticity are consequences of a martensitic phase transformation, which is a diffusionless first-order phase transformation between a high-temperature austenite phase and a low-temperature martensite phase. At zero stress, shape-memory alloys are characterized by four transformation temperatures: austenite start A_s and austenite finish temperature A_f during heating, and martensite start M_s and martensite finish temperature M_f during cooling. Martensite start is the temperature at which a shape-memory specimen completely in the austenite phase begins to transform to martensite during cooling, and A_s is the temperature at which the specimen completely in the martensite begins to transform

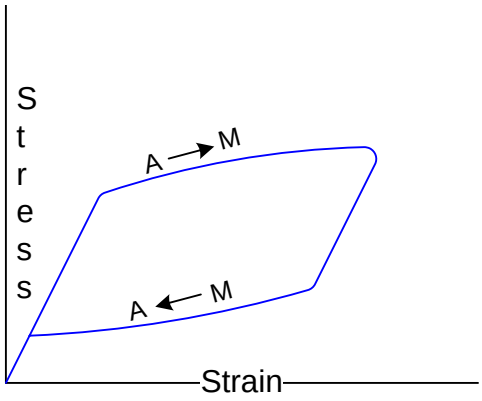

Figure 1.1: Superelasticity

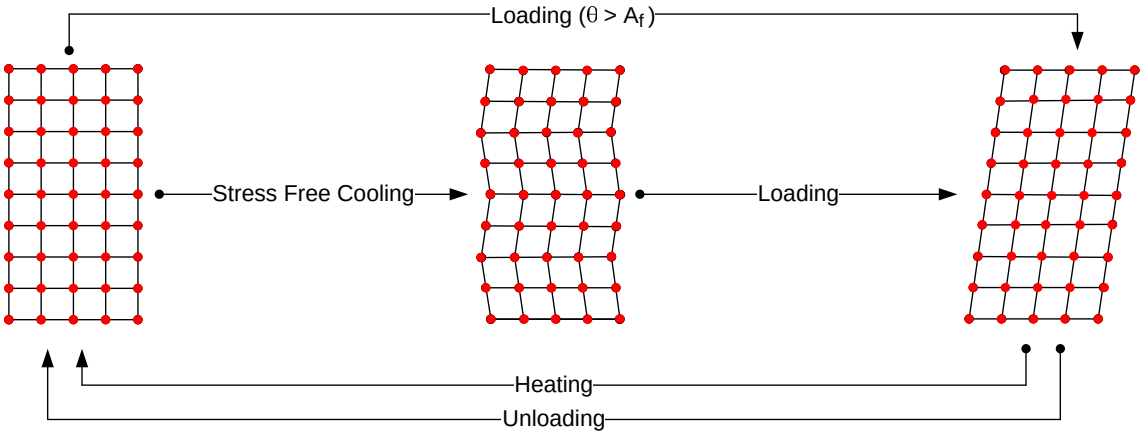

Figure 1.2: Austenite-martensite phase transformation

to austenite during heating. The M_f and A_f indicate the temperatures at which forward and reverse* phase transformation are finished under cooling and heating, respectively. Figure 1.2 gives an overview of the martensitic phase transformation in shape-memory alloys (35).

The shape-memory effect appears when an initially austenitic sample of a shape-memory alloy is tested at a temperature between austenite finish and martensite start. Under loading, the austenite transforms to martensite; in unloading, however, as the stress-free state is reached, there is an apparent residual strain that does not recover

*The austenite to martensite phase transformation is regarded as forward phase transformation in this context. Reverse transformation indicates the transformation of the martensite to austenite phase.

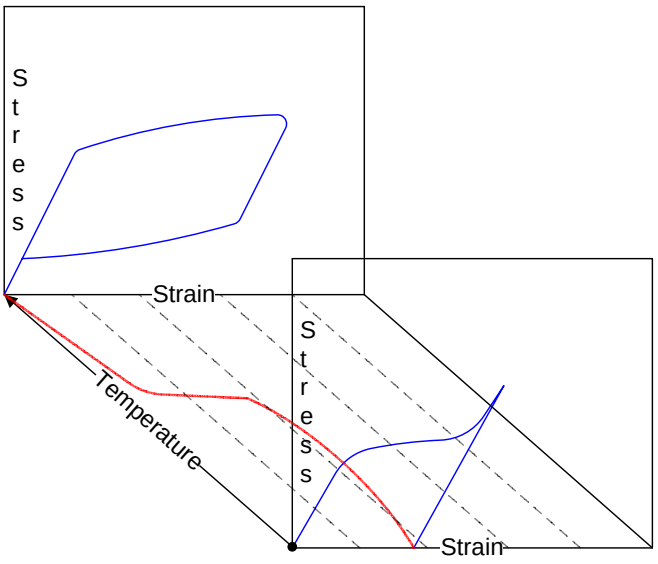

Figure 1.3: Shape-memory effect

until the temperature is subsequently raised above the austenite finish temperature. Figure 1.3 schematically demonstrates this effect for a typical shape-memory alloy (46).

The applications of shape-memory alloys and the need for a design tool have motivated a number of macroscopic constitutive models for these materials. Several of the existing models are developed in one dimension and capture the main characteristics of SMAs such as the shape-memory effect and superelasticity. Prominent among the earlier one-dimensional models are models developed by Tanaka (1986), Liang and Rogers (1990), Abeyaratne and Knowles (1993) and Brinson (1993).

Tanaka (51) proposed a model to describe the thermomechanic response of shape-memory alloys qualitatively. The model developed by Liang and Rogers (28) is based on the Tanaka's model. They proposed a new set of cosine functions to describe the kinetics of phase transformation and to reproduce the behavior of these materials quantitatively. This model does not properly capture the material response at temperatures below the martensite start temperature. It also fails at higher temperatures where temperature-induced martensite is present. Brinson (14) and (16) improved the Liang model by dividing the martensite volume fraction to stress-induced

and temperature-induced martensite. Abeyaratne and Knowles (2) explicitly constructed a Helmholtz free energy, a kinetic relation and a nucleation criterion for a one-dimensional thermoelastic solid, capable of undergoing either mechanically- or thermally-induced phase transitions and conducted a qualitative study of the macroscopic response predicted by their model in comparison to experimental results.

There have also been worldwide activities to simulate some of many characteristics of SMAs effectively. A. Bhattacharyya et al. (1995) presented a one-dimensional model to simulate the thermoelectric heat transfer of SMA actuators. This model (12) takes into account the change in the heat capacity of a shape-memory alloy as phase transformation proceeds. Naito et al. (2004) developed a one-dimensional model to analyze the quasistatic behavior of the phase rearrangement and transformation of the shape-memory alloys for a wire. This model (32) does not adequately capture the tension-compression asymmetry of shape-memory alloys. Figure 1.4 is a schematic demonstration of this feature. This is a typical loading-unloading experiment under tension and compression where the stress level is assumed to be smaller than the plastic yield stress. The loading is quasistatic and the ambient temperature is assumed constant and above the austenite finish temperature. Notice in this figure that under compression a wider hysteresis loop along the stress axis is observed. The stress level required to start the forward phase transformation under compression is also higher than that of the tension experiment and the size of the stress-strain hysteresis along the strain axis is considerably smaller under compression.

Paiva et al. (2005) presented a model (36) to capture tension-compression asymmetry and plasticity effects; however as it is developed for quasistatic conditions, it does not capture the effect of dynamic loading and unloading rates as shown in Figure 1.5 (see (33)).

Among the three-dimensional models there have been models adapted from other phenomena like plasticity. The three-dimensional constitutive model of Auricchio et al. (1995) (3) is one such example that is able to reproduce some of the basic features of SMAs such as superelasticity and asymmetry.

Among others there are: The Lexcellent et al. (1996) (26) constitutive model

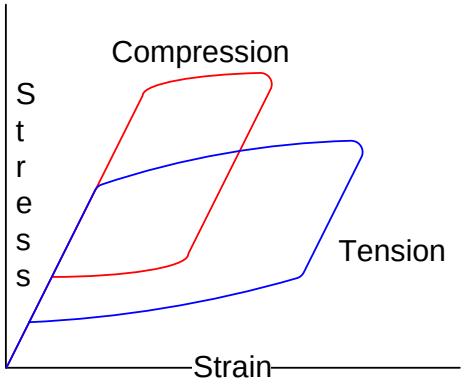

Figure 1.4: Asymmetry

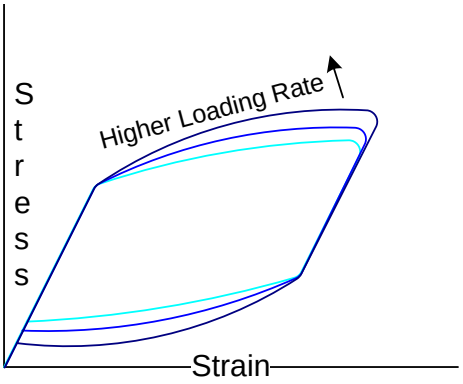

Figure 1.5: Rate effect

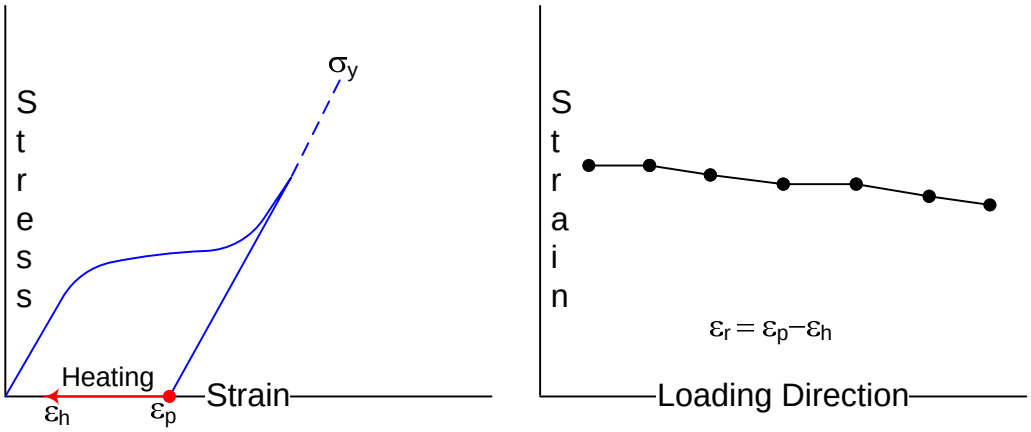

Figure 1.6: The effect of texture and anisotropy in stress-strain response (23).

for shape-memory Cu-Zn-Al single crystals, where the asymmetry in the superelastic stress-strain response of the alloy is reproduced; Brocca et al.'s (2002) (17) three-dimensional phenomenological constitutive model for polycrystalline SMAs, which is based on the microplane theory; Zhu et al.'s (2002) (56) constitutive model for stress-induced phase transformation, capable of simulating thermomechanical behavior of SMAs under proportional, non-proportional and cyclic loads; and Wang et al.'s (2003) (55) extension of Brinson's (1993) one-dimensional model into three dimensions where both shape-memory effect and superelasticity are captured.

None of the aforementioned models capture the anisotropy in the shape-memory alloy's response and the effect of texture as experimentally observed by Inoue et al. (23). To address micromechanical features such as texture, we need to understand the microstructure of the material and its relation to macroscopic properties in both single and polycrystals. Ball and James (1987) (5) developed a theoretical approach fine based on minimization of free energy, which characterizes the microstructural features involving fine mixtures of the phases. Experimental results show that some materials have good shape-memory behavior as single crystals but little or none as polycrystals, while others have good shape-memory behavior even as polycrystals. Bhattacharya and Kohn (1997) (5) developed an analytical model based on elastic energy minimization to study the effect of the texture on the amount of the recoverable

transformation strains. This model explains why materials such as NiAl and FeNiC, which undergo cubic-tetragonal transformations, make poor shape-memory polycrystals and why specially textured CuAlNi polycrystals have much larger recoverable strains than untextured ones. Abeyaratne and Knowles (1993) (2) studied the phase transition from a continuum perspective. They explicitly constructed a Helmholtz free energy, a kinetic relation and a nucleation criterion for a one-dimensional thermoelastic solid, capable of undergoing either mechanically or thermally induced phase transitions. Sun and Hwang (1993) (50) constructed a micromechanics constitutive model to describe the superelasticity and shape-memory behavior of polycrystalline shape-memory alloys in uniaxial mechanical loading.

Marketz and Fischer (1996) (30) developed a micromechanical approach to predict the effect of microstructural rearrangements in a Cu-Al-Ni shape-memory alloy in the fully martensitic state on the macroscopic mechanical behavior in uniaxial tension. Boyd and Lagoudas (1996) (13) developed a thermodynamic constitutive model for isotropic shape-memory alloys using a free energy function and a dissipation potential. They considered three different cases based on the number of internal state variables in the free energy: (1) austenite plus a variable number of martensite variants; (2) austenite plus two types of martensite; and (3) austenite and one type of martensite. The single-martensite model was chosen for detailed study because of its simplicity and its ease of experimental verification. Lu and Weng (1997) (29) developed a constitutive relation based upon the relationship between the shape-memory behavior and the crystallographic origin of the martensite transformation. Their theory is able to simulate the martensitic transformation and stress-strain relations of shape-memory alloys. Huang and Brinson (1998) (22) proposed a three-dimensional multivariant model for single crystal shape-memory alloy behavior. A key component of the model is the formation of *groups* of variants, which represent the tendency of the martensite plates to form self-accommodated groups to minimize energy. The single crystal behavior of the material to temperature and mechanical loads is derived using the concept of a thermodynamic driving force. The model exhibits appropriate responses for uniaxial results on single crystals.

Thamburaja and Anand (2001) (53) developed a crystal-mechanics-based constitutive model for polycrystalline shape-memory materials to study the effect of crystallographic texture. Niclaeys et al.(2002) (34) described the self-accommodation structure observed in NiTi alloys by developing an interaction matrix for a single crystal of austenite at a crystallographical scale. They also applied this model to simulate cooling Cu-based SMAs at low stress levels. Lexcellent et al. (2002) (27) proposed a phenomenological model and a micro-macro model to simulate the experimental measurements of the phase transformation yield surface[†] in the principal stress space under biaxial polycrystalline shape-memory alloys. The model describes well this surface for CuAlBe, CuAlZn (where a cubic to monoclinic phase transformation occurs) and CuAlNi (where cubic to orthorhombic phase transformation happens). The prediction is not efficient in the important case of TiNi however.

The purpose of this thesis is to present a three-dimensional constitutive model that builds on the concepts that have emerged from micromechanical analysis. For a model to be usable in the context of design, it has to be relatively simple, and it should be capable of being implemented in standard stress-analysis software. At the same time, it has to incorporate realistic physics. Indeed, each object and function in the model should in principle be computable from a lower-scale model, but possible to fit to empirical data. For the model to be widely applicable it should have the following characteristics: it has to be applicable in a wide range of temperatures so that it captures both the shape-memory effect and superelasticity; it has to be adaptable to a wide range of materials and textures; it has to hold for a wide range of loading rates; it has to be able to work with multi-axial proportional and non-proportional loadings. Finally, since phase transformation often competes with plasticity in shape-memory alloys, the model should incorporate that phenomenon as well.

The plan of this thesis is as follows: Chapter 2 presents a constitutive model for shape-memory alloys that builds on ideas generated from recent micromechanical studies of the underlying microstructure of these materials. This chapter focuses on

[†]The surface in the stress space that determines the onset of stress-induced martensitic phase transformations.

development of the theory in one dimension. The model is valid for a wide range of strain rates and incorporates plasticity. It is applicable in a wide temperature range that covers both the shape-memory effect and superelasticity, which are consequences of the martensitic phase transformation between a high-temperature austenite phase and a low-temperature martensite phase. The crystallographic symmetry of the austenite is higher than that of the martensite, and consequently one can have a number of symmetry-related variants of martensite. The different variants of martensite, along with the austenite, form complex microstructures that can evolve with load and temperature. A key difficulty in the constitutive modeling of these materials is to find an effective means of describing this evolution, especially in polycrystals. This issue is addressed here by introducing the idea of the *effective transformation strain*. It is the average transformation strain of the different variants averaged over a representative volume containing multiple grains after the material has formed an allowable microstructure. It is allowed to take any value in the set of effective transformation strains, or set of effective recoverable strains. The micromechanical basis for this set can be found in Bhattacharya and Kohn (9) (also see (11)). This set depends on the material and the texture of the specimen, and can be easily fit to experiment. In one dimension, it is the interval from the recoverable compressive to the recoverable tensile strain as presented in (43). In full dimensions it is a five-dimensional surface in the transformation strain space (44). It is also the convex dual of the transformation yield set introduced by Lexcellent and his coworkers (27). Another important idea in this model is the use of kinetic relations that cover a wide range of strain rates. The usual balance laws do not fully determine the phase transformation growth and there is a need for additional constitutive information in the form of a kinetic relation. The kinetic relation is constructed such that the growth rate of the volume fraction of the martensitic phase is a constitutive function of the thermodynamic driving force and effectively stress. We need a relation that is characterized by a stick-slip behavior at small driving forces. The kinetic relation needs to be rate-dependent at larger driving forces and rate-independent at smaller driving forces to be consistent with the experimental observations.

This chapter is organized as follows: First we discuss the kinematics, we introduce our field (internal) variables and explain the intervals that they belong to. Then it comes to the balance laws. We assume the balance of linear momentum and balance of energy hold. We use the second law of thermodynamics and derive the constitutive relations in a one-dimensional setting. We then formulate the driving forces and kinetic relations governing the evolution of our internal variables. The chapter continues with a thorough study of the capabilities of the model. First the ability of the model to simulate the superelastic behavior as well as the tension-compression asymmetry is demonstrated. Then the effect of loading rates, ambient temperature and the yield strength is discussed. Simulations also show the ability of the model to reproduce the shape-memory effect. We take a close look at the stress-strain hysteresis and discuss internal loops of the hysteresis for a simple applied stress. All of the above are demonstrated under stress-control, which is rather difficult to attain experimentally. In materials like shape-memory alloys that involve the evolution of internal variables, the stress-strain curve varies with the methodology of the experiment. A particularly popular means of measuring material properties at high deformation rates is the Kolsky or split-Hopkinson bar. The chapter concludes with a brief introduction to the methodology of this experiment followed by strain-controlled simulations, emphasizing the sensitivity of the stress-strain response to parameters such as ambient temperature, pulse amplitude, pulse size and pulse shape.

Chapter 3 presents our micromechanics-inspired constitutive model for polycrystalline shape-memory alloys in three dimensions. The model is a generalization of the one-dimensional model and remains applicable in a wide range of temperatures and strain rates. It is able to reproduce the stress-strain response for complex proportional and nonproportional loading patterns and can simulate the effect of texture on a polycrystal of shape-memory alloy. The kinematics of the three-dimensional model is discussed first, then the constitutive relations, thermodynamic driving forces and kinetic relations are derived. In this chapter we consider two types of temperature evolutions: adiabatic and non-adiabatic. Under non-adiabatic conditions we demonstrate how the stress-strain behavior is affected by the changes in the thermal

parameters such as convective heat transfer coefficient.

A major player in the present model is the idea of the effective transformation strain. Transformation strain is postulated to live inside or on the boundary of a set that is called the set of the recoverable strains or phase transformation yield surface. In this chapter we present a form for such a set and carefully explain how to estimate the parameters of the set for different materials and textures. The role of the phase transformation surface in this context is similar to that of the yield surface in elasto-plastic materials. It is to be noted that the phase transformation locus is path-independent in the sense that a point on it may be approached by many different loading paths within the untransformed region inside. We consider three different cases for the transformation criterion: the isotropic and symmetric case, the isotropic and asymmetric case, and the anisotropic and asymmetric case.

In the demonstration section, we first focus on the isotropic case and show how to derive the phase transformation locus for an isotropic specimen. We start the analysis by studying the stress-strain response of a set of proportional loading and unloading experiments. We demonstrate thermomechanical coupling by studying stress-strain behavior of uniaxial tension, uniaxial compression, pure shear and biaxial tension-compression tests at different initial temperatures. We also study this coupling by demonstrating the sensitivity of the stress-strain response to the changes of the convective heat transfer coefficient of the air for non-adiabatic thermal conditions. To show the applicability of model in complex loading experiments we demonstrate a nonproportional loading experiment on a NiTi shape-memory alloy.

In this chapter we also show the ability of this model to reproduce Inoue and coworkers' (23) experimental observations on the effect of initial texture on the shape-memory response. We study Shu and Bhattacharya's (1998) (47) analytical model and show how our model is able to capture the qualitative behavior of a polycrystal alloy and its dependence on texture. We choose an anisotropic framework and demonstrate a full parameter study for the phase transformation yield surface of an anisotropic NiTi polycrystal. We carefully study the phase transformation process, evolution of the internal variables and the stress-strain response for a number

of non-proportional loading experiments under stress-controlled and strain-controlled conditions. We compare these results for two different phase transformation surface profiles. The chapter is completed by a demonstration of the effect of texture on recoverable strains of a polycrystalline thin sheet of NiTi under uniaxial tensile stress. It is also shown how the qualitative behavior of the combined tension-torsion can depend on the texture. The results are in good agreement with experimental observations.

Chapter 4 presents an extension of the aforementioned constitutive model to formulate and study the martensitic phase transformations in pure iron under dynamic loading. There is extensive literature on the experimental study of rate sensitivity of iron and its deformation mechanisms. In this chapter we use our framework to describe the evolution of the microstructure as a reversible phase transformation occurs from a (bcc) structure α to an (hcp) crystallographic structure ε over strain rates ranging from $\dot{\varepsilon} = 10^{-4}(1/s)$ to $\dot{\varepsilon} = 10^{4}(1/s)$.

Conclusions and future directions are given in Chapter 5.

Appendix A presents an example of a MATLAB code for the stress-controlled three-dimensional analysis of anisotropic shape-memory alloys.

Chapter 2

One-Dimensional Constitutive Model for Shape-Memory Alloys

2.1 Constitutive Model

In this chapter, we develop and discuss a one-dimensional thermodynamically consistent constitutive framework for the dynamic behavior of polycrystalline shape-memory alloys. Our model builds on the concepts that have emerged from analysis of the microstructure of shape-memory alloys and its relation to macroscopic properties in both single and polycrystals. A generalization of the model in multiple dimensions with both proportional and non-proportional loading conditions is presented in the next chapter.

2.1.1 Kinematics

We are interested in a model that can be used at the macroscopic scale for the design of devices and structures. So we take a multiscale point of view and think of each material point of our continuum to correspond to a representative volume element (RVE) consisting of a number of grains, each containing a complex microstructure of austenite and variants of martensite. We introduce two kinematic or field or internal variables to represent the consequence of microstructure in an RVE: the *volume fraction of martensite*, $\lambda(x,t)$, and the *effective transformation strain of the martensite*, $\varepsilon_m(x,t)$.

$\lambda(x,t)$ denotes the net or average volume fraction of the martensite, i.e., this would be the value we would obtain if we were to visit each grain in the RVE corresponding to the material point x at time t, add up the volume of all variants of martensite (self-accommodating, internally twinned, detwinned etc.) and divide by the total volume of the RVE. To be precise, let χ^{ij} denote the characteristic function of the jth correspondence variant of martensite in the ith grain of the RVE. This function is equal to 1 at all positions occupied by the jth variant in the i grain and is equal to 0 otherwise. Then $\chi^i = \sum_{j=1}^{N} \chi^{ij}$ is the characteristic function of martensite in the ith grain where N, the number of variants, is given by the crystallography of the transformation. We define the volume fraction as

$$\lambda = \langle \chi^i \rangle = \left\langle \sum_{j=1}^{N} \chi^{ij} \right\rangle \tag{2.1}$$

where $\langle \cdot \rangle$ denotes mean or expected value over all grains in the RVE, i.e., over all i. λ is constrained to lie between 0 and 1, with 0 signifying that the entire RVE is in the austenite phase and 1 signifying that the entire element is in the martensite phase.

Since λ can not differentiate between the different microstructures of martensite like self-accommodating, internally twinned, detwinned etc., we introduce the second internal variable $\varepsilon_m(x,t)$. This is the strain we would obtain if we were to visit every grain in the RVE corresponding to the material point x at time t and average over the transformation or stress-free strain of all the variants of martensite. To be precise, let ε_m^{ij} denote the transformation or stress-free strain of the jth variant of martensite in the ith grain in the RVE. It is given by

$$\varepsilon_m^{ij} = R_i^T \varepsilon_m^j R_i \tag{2.2}$$

where ε_m^j is the transformation strain of the jth correspondence variant in a reference crystal and is given by crystallography of the transformation, while R_i is the rotation matrix that gives the orientation of the ith grain and is given by the texture of the

material. We define the effective transformation strain as

$$\varepsilon_m = \left\langle \sum_{j=1}^{N} \chi^{ij} \varepsilon_m^{ij} \right\rangle . \tag{2.3}$$

As the material forms different microstructures, the arrangement of variants and thus χ^{ij} changes, and $\varepsilon_m(x,t)$ takes different values. We are only interested in compatible microstructures, and thus we can not form any arbitrary mixture of variants. Consequently ε_m can not take any arbitrary average value, but is restricted to those that are obtained from compatible arrangements. We denote the set of all possible values of ε_m as the *set of effective transformation strains* or the *set of effective recoverable strains*, P. This set P depends on the crystallography of the material and the texture of the specimen. In a single crystal, P is the set of all possible average transformation strains associated with compatible microstructures of the different variants of martensite. In a polycrystal, the set P is the macroscopic averages of locally varying strain fields, which can be accommodated within each grain by a compatible arrangement of the martensite variants. One can calculate this set in various examples of interest and estimate them in others (9; 8; 11). Alternately, one can use experimental measurements of recoverable strain to fit this set.

Note that we do not track the individual volume fractions of the different volumes of martensite. This is too difficult, especially in a polycrystal where the different grains behave differently depending on orientation, inter-granular constraints and long-range cooperative effects. However, we implicitly account for these effects by tracking the effective transformation strain and confining it to the set P, which depends on material and texture. In other words, the set P incorporates information about the material crystallography, specimen texture and also inter-granular constraints.

The set P can be quite complicated in multiple dimensions, but it is relatively simple in one dimension. It is an interval $[\varepsilon_m^c, \varepsilon_m^t]$ where $\varepsilon_m^c < 0$ denotes the largest recoverable compressive strain and $\varepsilon_m^t > 0$ denotes the largest recoverable tensile strain.

In summary, the consequences of the microstructure at a material point is specified by two internal variables λ and ε_m, which are subject to the following constraints.

$$\lambda \in [0,1] \quad \text{and} \quad \varepsilon_m \in P = [\varepsilon_m^c, \varepsilon_m^t]. \tag{2.4}$$

Finally, we introduce the plastic strain ε_p as an additional field variable. Putting everything together, we say that the total strain can be divided into three parts, elastic, transformation and plastic:

$$\varepsilon(x,t) = \frac{\partial u}{\partial x} = \varepsilon_e(x,t) + \lambda(x,t)\varepsilon_m(x,t) + \varepsilon_p(x,t). \tag{2.5}$$

It is worth noting that the effective transformation strain of the RVE is $\lambda\varepsilon_m$ since λ is the volume fraction of martensite, ε_m is the effective transformation strain of the martensite and the transformation strain of the austenite is 0 by choice of reference configuration.

2.1.2 Balance laws

We assume that the usual balance laws hold. First is the balance of linear momentum

$$\rho u_{tt} = \sigma_x \tag{2.6}$$

where ρ is the (referential) mass per unit length and σ is the (Piola-Kirchhoff) stress.

Second, we assume the balance of energy. Writing the balance of energy for any part of the body, localizing and using (2.6), we obtain

$$\dot{\epsilon} \;=\; -q_x + r + \sigma\dot{\varepsilon}\,. \tag{2.7}$$

Above, ϵ denotes the internal energy density, q the heat flux and r the radiative heating or the heat supply per unit volume.

Finally, we write the second law of thermodynamics or the Clausius-Duhem in-

equality, again in local form:

$$\dot{\eta} \geq \left(-\frac{q}{\theta}\right)_x + \frac{r}{\theta} \quad \Rightarrow \quad \theta\dot{\eta} \geq -q_x + \frac{q\theta_x}{\theta} + r. \tag{2.8}$$

Here, η is the entropy density and θ the (absolute) temperature.

Using (2.7) in the second law (2.8), we obtain

$$-\dot{\epsilon} + \theta\dot{\eta} + \sigma\dot{\varepsilon} - \frac{q\theta_x}{\theta} \geq 0\,. \tag{2.9}$$

It is now convenient to the introduce Helmholtz free energy density $W = \epsilon - \theta\eta$ and rewrite the second law in the following form

$$-\dot{W} - \eta\dot{\theta} + \sigma\dot{\varepsilon} - \frac{q\theta_x}{\theta} \geq 0\,. \tag{2.10}$$

2.1.3 Constitutive relations, driving forces and kinetic relations

We assume that the Helmholtz free energy density depends on the strain, the temperature and the internal variables.

$$W = W(\varepsilon, \lambda, \varepsilon_m, \varepsilon_p, \theta). \tag{2.11}$$

We make similar assumptions on the stress. Substituting these in the second law, (2.10), we obtain,

$$-\left(\frac{\partial W}{\partial \varepsilon} - \sigma\right)\dot{\varepsilon} - \frac{\partial W}{\partial \lambda}\dot{\lambda} - \frac{\partial W}{\partial \varepsilon_m}\dot{\varepsilon}_m - \frac{\partial W}{\partial \varepsilon_p}\dot{\varepsilon}_p - \left(\frac{\partial W}{\partial \theta} + \eta\right)\dot{\theta} - \frac{q\theta_x}{\theta} \;\geq\; 0. \tag{2.12}$$

Using arguments similar to those of Coleman and Noll (19), we conclude that

$$\sigma = \frac{\partial W}{\partial \varepsilon}, \quad \eta = -\frac{\partial W}{\partial \theta}. \tag{2.13}$$

We also assume Fourier's law of heat transfer:

$$q = -k\theta_x \tag{2.14}$$

where $k > 0$ is the conductivity.

We define the *driving forces* associated with the internal variables to be the quantities conjugate to their rates of change in (2.12):

$$d_\lambda := -\frac{\partial W}{\partial \lambda}, \quad d_{\varepsilon_m} := -\frac{\partial W}{\partial \varepsilon_m}, \quad d_{\varepsilon_p} := -\frac{\partial W}{\partial \varepsilon_p}. \tag{2.15}$$

Substituting these back into (2.12), and using (2.13) and (2.14), we conclude that the second law reduces to the requirement that

$$d_\lambda \dot{\lambda} + d_{\varepsilon_m}\dot{\varepsilon}_m + d_{\varepsilon_p}\dot{\varepsilon}_p \;\geq\; 0\,. \tag{2.16}$$

We have to prescribe the evolution of the internal variables to be consistent with this relation.

We assume that the evolution of the internal variables λ, ε_m depends on the driving forces through the following *kinetic relations*, and subject to the constraints (2.4):

$$\dot{\lambda} = K_\lambda(d_\lambda, \lambda, \varepsilon_m) \qquad \lambda \in [0,1], \tag{2.17}$$

$$\dot{\varepsilon}_m = K_{\varepsilon_m}(d_{\varepsilon_m}, \lambda, \varepsilon_m) \qquad \varepsilon_m \in [\varepsilon_m^c, \varepsilon_m^t]. \tag{2.18}$$

Finally we assume that the evolution of the internal variable ε_p is prescribed as in the rate-independent theory of plasticity. We postpone its discussion till the next section.

2.1.4 Specific constitutive assumptions

We specialize to the following constitutive relation for the Helmholtz energy,

$$W = \frac{E}{2}\left(\varepsilon - \varepsilon_p - \lambda\,\varepsilon_m\right)^2 + \lambda\,\omega(\theta) - c_p\,\theta \ln\left(\frac{\theta}{\theta_0}\right) \tag{2.19}$$

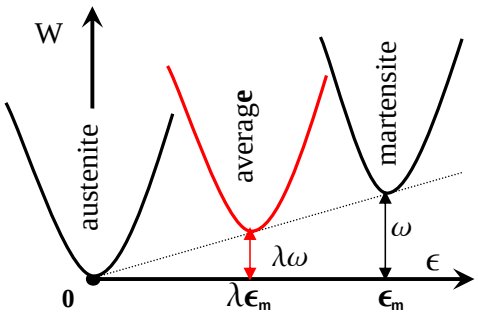

Figure 2.1: Schematic representation of the Helmholtz energy density.

where E is the elastic modulus (assumed to be equal in both the austenite and the martensite), ω is the difference in chemical energy between the austenite and the martensite, c_p is the heat capacity (assumed to be equal in both the austenite and the martensite), and ordinary thermal expansion is neglected. A schematic form of this relation at some temperature above austenite finish temperature, where austenite is the stable phase, is illustrated in Figure 2.1. We further assume that

$$\omega(\theta) = \frac{\mathcal{L}}{\theta_{cr}}(\theta - \theta_{cr}) \tag{2.20}$$

where $\mathcal{L}$ is the latent heat of transformation and θ_{cr} is the thermodynamic transformation temperature. Both parameters are evaluated through experimental measurements. Substituting (2.19) and (2.20) in (2.13), we obtain

$$\begin{aligned}
\sigma &= E(\varepsilon - \varepsilon_p - \lambda\,\varepsilon_m), && (2.21)\\
\eta &= \lambda\frac{\mathcal{L}}{\theta_{cr}} - c_p\left(1 + \ln\left(\frac{\theta}{\theta_0}\right)\right), && (2.22)\\
d_\lambda &= \sigma\varepsilon_m - \omega, && (2.23)\\
d_{\varepsilon_m} &= \lambda\sigma, && (2.24)\\
d_{\varepsilon_p} &= \sigma. && (2.25)
\end{aligned}$$

The kinetic relation describing the evolution of the martensite volume fraction λ

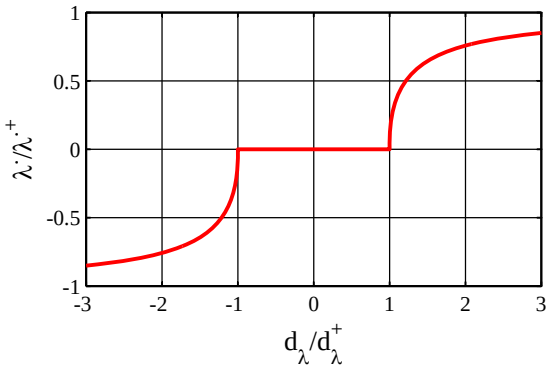

Figure 2.2: The kinetic relation between $\dot{\lambda}$ and the driving force d_λ

is taken to be the following:

$$\dot{\lambda} = \begin{cases} \dot{\lambda}^+ \left(1 + (d_\lambda - d_\lambda^+)^{-1}\right)^{-\frac{1}{p}} & d_\lambda > d_\lambda^+ \text{ and } \lambda < 1 \\ \dot{\lambda}^- \left(1 + (d_\lambda^- - d_\lambda)^{-1}\right)^{-\frac{1}{p}} & d_\lambda < d_\lambda^- \text{ and } \lambda > 0 \\ 0 & \text{otherwise} \end{cases} \tag{2.26}$$

where $\dot{\lambda}^\pm, d_\lambda^\pm, p$ are material parameters. This relation is shown in Figure 2.2. Note that the kinetic relation is characterized by a "stick-slip" character at small driving forces. The phase transformation requires a critical driving force before it can proceed, i.e., the rate of change of volume fraction is 0 for driving forces below a critical driving force. As one exceeds the critical driving force, note the curve is vertical meaning that the rate of phase transformation is indeterminate or equivalently the driving force is independent of rate of phase transformation. This is rate-independent behavior. The reason for this is a combination of metastability (6) and pinning by defects (1; 7; 10). However, at large driving forces, it becomes rate-dependent and in fact asymptotes to a limiting rate. The reason for this is that phase boundaries require an unboundedly increasing driving force for the propagation speeds to reach towards some sound speed (10; 38). Note that this kinetic relation is consistent with the experimental observations that say that for low driving forces, around $d_\lambda^\pm$, phase transformation is rate-independent (35) and at large driving forces, material shows rate dependency (33).

The evolution of the effective transformation strain ε_m describes the twinning, detwinning and other such processes that convert one martensitic variant to another. We assume a rather simple law for its evolution:

$$\dot{\varepsilon}_m = K_{\varepsilon_m}(d_{\varepsilon_m},\, \lambda,\, \varepsilon_m) = \frac{\alpha}{\lambda}\, d_{\varepsilon_m} = \begin{cases} \alpha\sigma & \varepsilon_m \in [\varepsilon_m^c,\, \varepsilon_m^t] \\ 0 & \text{otherwise} \end{cases} \tag{2.27}$$

where α is a material parameter and is chosen large enough to guarantee a very quick process, so that ε_m is essentially equal to ε_m^t and ε_m^c under tension and compression respectively.

Finally, we assume a rate-independent plasticity relation that neglects the Bauschinger effect:

$$\dot{\varepsilon}_p = K_{\varepsilon_p}(d_{\varepsilon_p},\, \sigma_y) = \frac{\dot{d_{\varepsilon_p}}}{H} = \begin{cases} \frac{\dot{\sigma}}{H} & \sigma \geq \sigma_y \text{ or } \sigma \leq -\sigma_y \\ 0 & \text{otherwise} \end{cases} \tag{2.28}$$

where H is the hardening parameter and σ_y is the plastic yield stress.

This completes the specification of the model.

2.1.5 Temperature evolution

The energy balance along with the constitutive relations describe the evolution of the temperature. However, this is rather complicated, and therefore it is useful to make some simplifying assumptions.

We begin by substituting for the internal energy in terms of the Helmholtz free energy and entropy in the energy balance (2.7) to rewrite it as

$$\dot{W} + \theta\dot{\eta} + \dot{\theta}\eta = -q_x + r + \sigma\dot{\varepsilon}. \tag{2.29}$$

Using the constitutive assumption (2.19) for W to expand $\dot{W}$, using the various definitions of driving force and simplifying, we obtain

$$\theta\dot{\eta} = -q_x + r + d_\lambda\dot{\lambda} + d_{\varepsilon_m}\dot{\varepsilon}_m + d_{\varepsilon_p}\dot{\varepsilon}_p. \tag{2.30}$$

Specializing now to the specific constitutive relation and in particular (2.22), we obtain,

$$c_p\dot{\theta} = \dot{\lambda}\theta\frac{\mathcal{L}}{\theta_{cr}} - q_x + r + d_\lambda\dot{\lambda} + d_{\varepsilon_m}\dot{\varepsilon}_m + d_{\varepsilon_p}\dot{\varepsilon}_p. \tag{2.31}$$

In the sequel, we shall be interested in processes where we can neglect heat transfer ($q = r = 0$). Further, it turns out that the latent heat of transformation is large compared to the energy dissipated during transformation, martensitic variant reorientation and plasticity during typical processes of interest. Therefore we assume

$$c_p\dot{\theta} \;=\; \theta\dot{\lambda}\frac{\mathcal{L}}{\theta_{cr}}. \tag{2.32}$$

Integrating this, we obtain a relation between temperature, volume fraction of martensite, latent heat and specific heat:

$$\theta(t) \;=\; \theta_0 \exp\left(\frac{(\lambda(t) - \lambda_0)\mathcal{L}}{c_p\theta_{cr}}\right). \tag{2.33}$$

2.2 Demonstration

In this section the model is demonstrated using both stress-controlled and Kolsky bar experiments. We demonstrate that our model is consistent with the observed asymmetric response of shape-memory alloys under tension and compression. It is able to capture the behavior under a wide range of temperatures spanning both the shape-memory effect and superelasticity, and a wide range of loading rates. The model is relatively easy to use, and this is demonstrated by designing the necessary pulse for a constant strain rate in a Kolsky bar experiment. Throughout this section, we calculate the response of a material point to a given load or deformation history.

2.2.1 Parameters

Consistent with typical experiments on NiTi (see for example (31)), we consider the following parameters:

$$\begin{aligned} M_s &= -51.55\,^oC \quad \text{and} \quad A_s = -6.36\,^oC \\ \mathcal{L} &= 79\ (\frac{\text{MJ}}{\text{m}^3}) \quad \text{and} \quad c_p = 5.4\ (\frac{\text{MJ}}{\text{m}^3\,^o\text{K}}) \\ \varepsilon_m^c &= -2.5\% \quad \text{and} \quad \varepsilon_m^t = 5\% \\ E &= 65\ (\text{GPa}) \quad \text{and} \quad \sigma_y = 1500\ (\text{MPa}) \end{aligned} \tag{2.34}$$

where M_s and A_s are the martensite start and austenite start temperatures, respectively*. Recalling (2.26) and (2.23), we obtain

$$d_\lambda^+ = -\omega(M_s), \quad d_\lambda^- = -\omega(A_s). \tag{2.35}$$

Assuming further that

$$d_\lambda^+ = -d_\lambda^-, \tag{2.36}$$

*M_s is the temperature at which the specimen completely in the austenite phase begins to transform to martensite during cooling and A_s is the temperature at which the specimen completely in the martensite phase begins to transform to austenite during heating.

we conclude that

$$d_\lambda^+ = -d_\lambda^- = \mathcal{L}\left(\frac{A_s - M_s}{A_s + M_s}\right), \quad \theta_{cr} = \frac{A_s + M_s}{2}. \tag{2.37}$$

Note that one has to be careful to specify the absolute temperature in Kelvin to use these formulas.

We also assume the following kinetic coefficients:

$$\dot{\lambda}^+ = -\dot{\lambda}^- = 1, \quad \alpha = 1, \quad p = 2 \quad \text{and} \quad H = \frac{E}{50}.$$

Note that $\dot{\lambda}^\pm$ control the evolution rate of the volume fraction of martensite, are kept fixed in the entire chapter and chosen so that $\dot{\lambda}\,\varepsilon_m$ is smaller than $\dot{\varepsilon}$.

Parameter α is chosen to guarantee the fast speed of the evolution of phase transformation strain ε_m both under tension and compression as described earlier. While larger α's do not change the results, smaller α's may lead to slow evolution of ε_m, which is not acceptable in this setting.

The power of the kinetic law p controls the shape of its function, for the given value of $p = 2$ its form is shown in Figure 2.2. For higher values the kinetic relation would get closer to a Heaviside function in the first and third quadrant.

2.2.2 Superelasticity

To demonstrate the capability of this model to reproduce the superelastic response of shape-memory alloys, we here compare our simulation results with those of pure tension experimental results of McNaney et al. (31) as shown in Figure 2.3. Ambient temperature is set to be equal to the room temperature $\theta = 22\,^oC$. Transformation temperatures are characterized by differential scanning calorimetry in the experiment and are equal to the ones mentioned earlier (2.34). It is good to note that austenite finish temperature A_f is equal to 18.13^oC, which ensures that the material is initially in the austenite phase, as we are above the austenite finish temperature.[†]

[†]All other parameters used are as described earlier in (2.34) except $\mathcal{L} = 8.8$ J/g and $E = 40$ GPa.

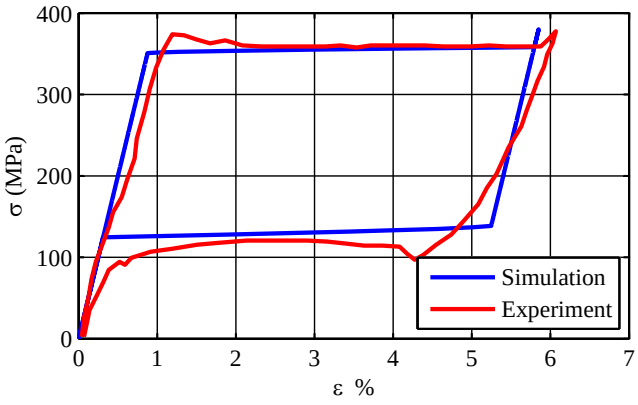

Figure 2.3: Comparison between the experiment (31) and the fit to the model.

This simulation is for a quasistatic case as strain rates are in the range of $10^{-5}s^{-1}$ to $10^{-4}s^{-1}$.

As illustrated in the figure the initial elastic response is followed by a stress plateau where forward phase transformation occurs. The specimen transforms completely to martensite at approximately 5.8% strain and upon further loading behaves elastically. Unloading of the specimen is initially elastic, followed by a lower plateau where the reverse phase transformation occurs. The material behaves elastically again when it is totally transformed back to austenite. It is clear that the model is able to reproduce the overall features of the experiment. However, we see some differences. First, notice that the unloading begins with a greater slope in our model compared to the experiment. This is because our model assigns the same elastic moduli for both the austenite and the martensite while the experimental values are different. This may be easily changed. Second, the experiment shows a slight overshoot in both loading and unloading, but the model does not. This is related to localization and is beyond the scope of this chapter.

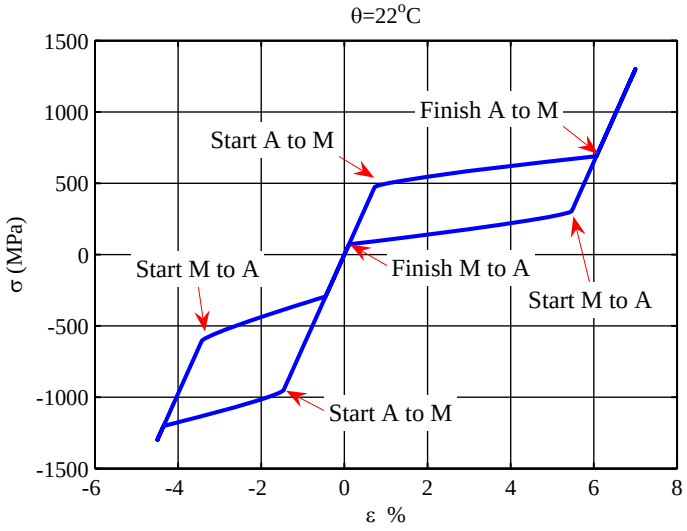

Figure 2.4: A typical stress-strain curve generated by the model.

2.2.3 Tension-compression asymmetry

In this section we evaluate the ability of the model to capture the tension-compression asymmetry. We consider an applied stress of the form

$$\sigma(t) = A \sin \omega t \tag{2.38}$$

with $A = 1300$ MPa and $\omega = 2\pi/T$ with T equal to 5×10^{-3} seconds unless otherwise mentioned. In particular, this value of loading is below the chosen yield strength, and thus plasticity is suppressed. We examine this aspect later in this chapter. We integrate (2.26), (2.27), (2.28), (2.33) as well as (2.21) simultaneously subject to the initial conditions

$$\varepsilon(0) = 0.0\%, \quad \varepsilon_p(0) = 0.0\%, \quad \varepsilon_m(0) = 0.0\%, \quad \lambda(0) = 0 \quad \text{and} \quad \theta(0) = 22\,^oC \tag{2.39}$$

to obtain the time-trajectory of ε, ε_m, ε_p, λ and θ.

The result is shown in Figure 2.4. As we start loading, the material deforms elastically till reaching the point at the top-left corner of the upper *flag*. At this point the austenite to martensite phase transformation starts and this results in a change

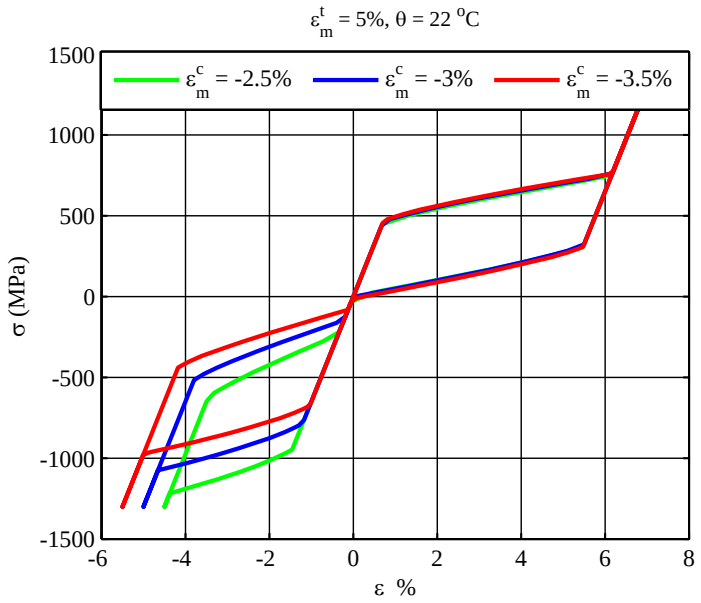

Figure 2.5: Effect of the relative values of the phase transformation strains in the asymmetric response

of slope. It continues till the material fully transforms to martensite and we reach the top-right corner of the upper flag. The material deforms elastically beyond that. As material is unloaded, it deforms back elastically till the driving force gets equal to d_λ^- at the bottom-right corner of the upper flag. The reverse phase transformation starts as we traverse the lower side of the upper flag. The reverse phase transformation continues till the material transforms back to austenite completely at the bottom-left corner of the upper flag. The material undergoes the same process under compression; however, the stress level required to nucleate the martensite phase from the parent austenite phase is higher in compression than in tension; the transformation strain measured in compression is smaller than that in tension; the hysteresis loop generated in compression is wider (along the stress axis) than the hysteresis loop generated in tension, consistent with the well-known asymmetry of shape-memory alloys.

Figure 2.5 schematically shows the effect of the relative values of the compressive ε_m^c and tensile ε_m^t phase transformation strains in the shape of the stress-strain response.

2.2.4 Ambient temperature and the shape-memory effect

Figures 2.6 through 2.10 show the effect of change of the ambient temperature in the stress-strain hysteresis. The initial temperature is taken to be the ambient temperature (instead of that in (2.39)), and subsequently allowed to evolve according to (2.33).

At the lowest ambient temperature, 200°K, shown in Figure 2.6, λ quickly increases to 1 as the austenite transforms to martensite and remains there independent of loading. So the stress-strain curve reflects the evolution of ε_m, or reorientation of martensitic variants. This changes as the ambient temperature increases through M_s and A_s till at 295°K, one is completely in the austenite at zero stress independent of the loading history. So this stress-strain curve reflects the stress-induced transformation. As the ambient temperature increases, stress required to induce the transformation increases (faster in compression than in tension since the transformation strains are different), till no transformation is observed at 425°K. All of this is consistent with observations and the well known Clausius − Clapeyron relation (35).

It is worth remarking that these plots show that this model captures both the shape-memory effect as well as the stress-induced transformation. The latter is observed at 295°K. To observe the former, suppose we cool the specimen with no stress. As remarked above, the material transforms to martensite as λ increases to 1 as we pass below M_s to say 200°K. However, the transformation strain ε_m remains at 0, and it follows from (2.21) that the strain ε remains at 0. Thus, transformation induced by cooling produces no strain, something called self-accommodation, and this is captured by the model. Now, deform the specimen. It is clear from stress-strain curve at 200°K, that unloading causes a residual strain or permanent deformation. Finally heat the specimen to above A_f to say 295°K. Note from stress-strain curve that the only strain consistent with zero stress is zero, and thus the specimen recovers its permanent deformation. This is the shape-memory effect.

To study the temperature dependence of the critical phase transformation stress we can also use the equation (2.23), which relates the thermodynamic driving force

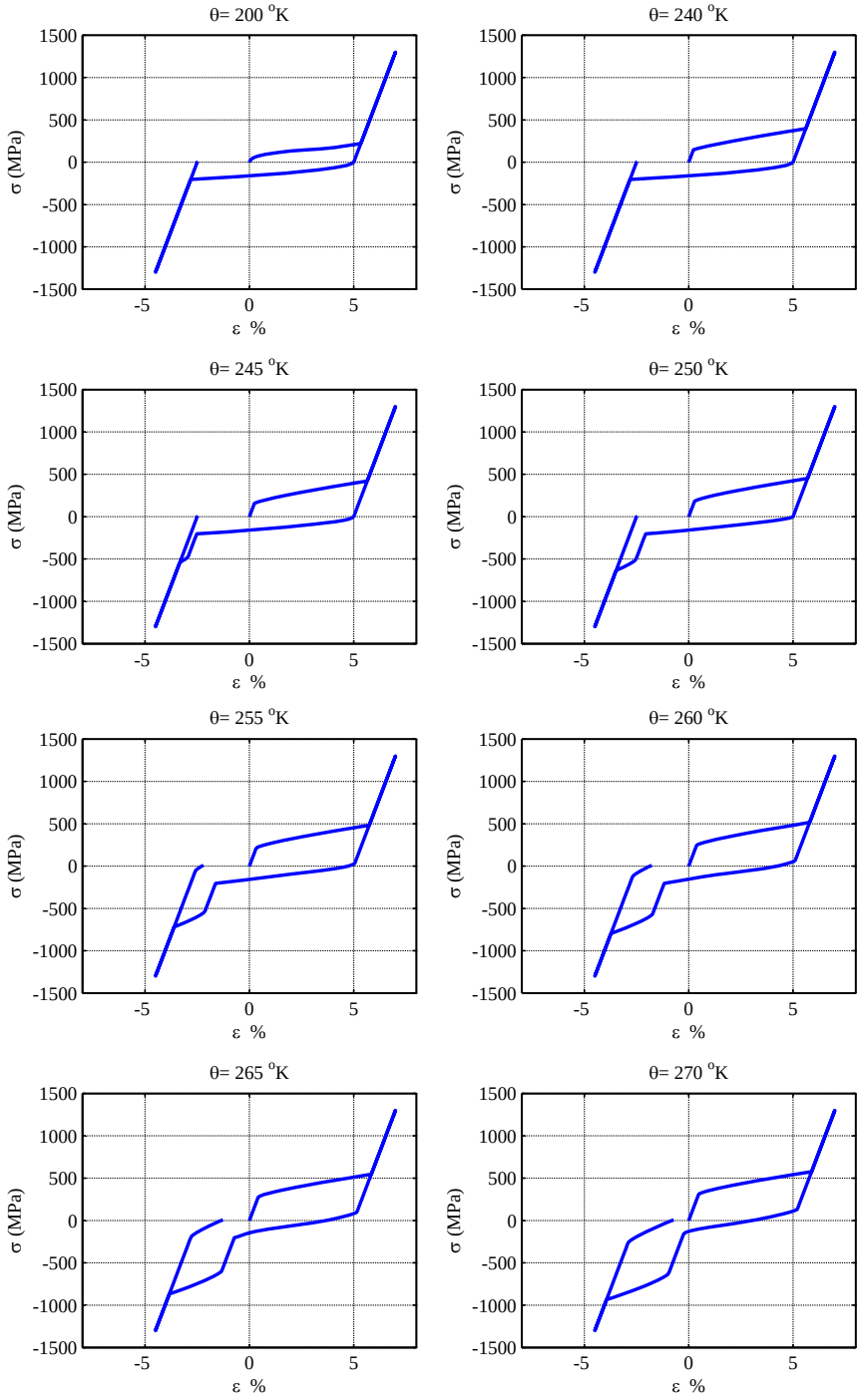

Figure 2.6: The stress-strain behavior at different ambient temperatures.

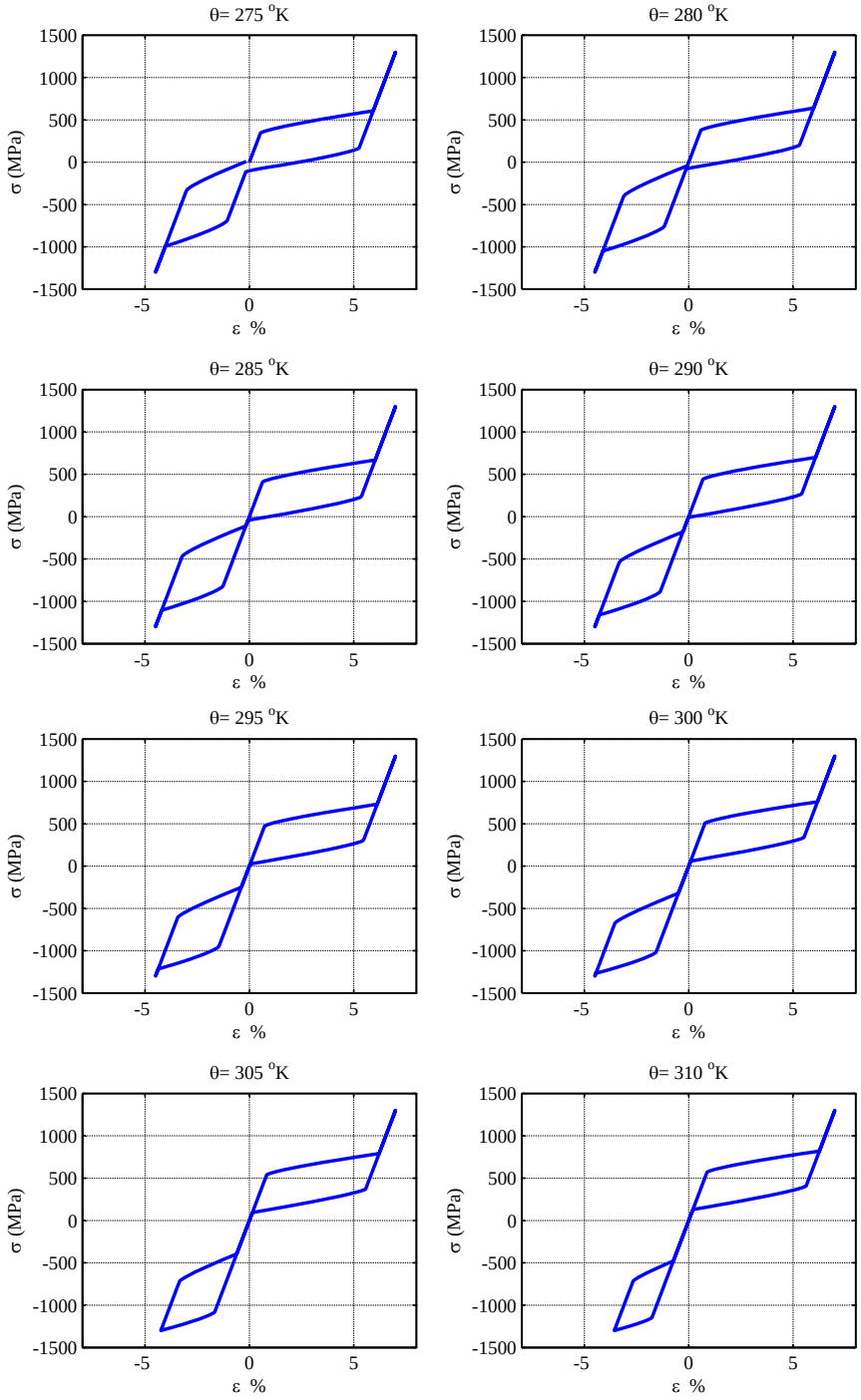

Figure 2.7: The stress-strain behavior at different ambient temperatures.

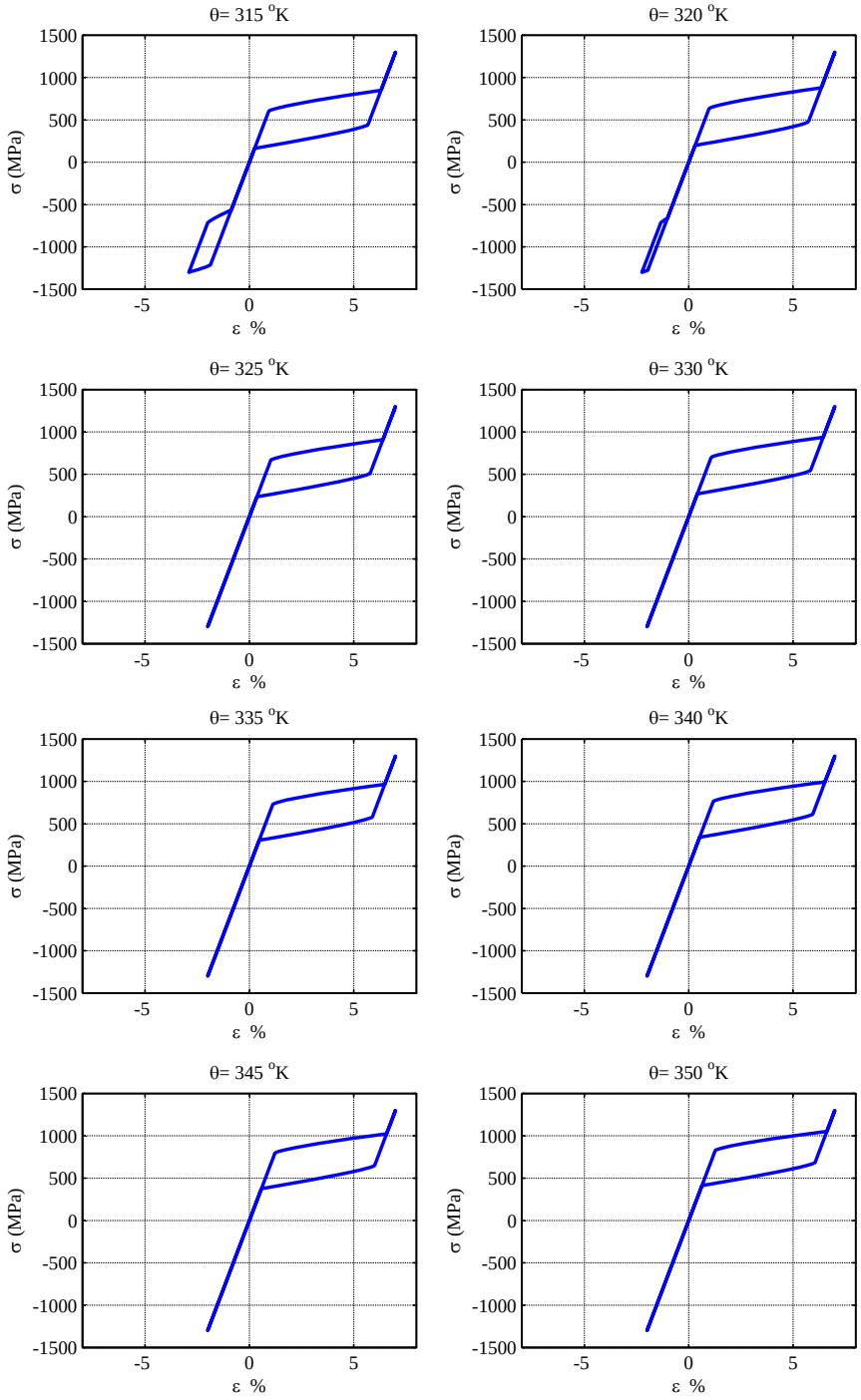

Figure 2.8: The stress-strain behavior at different ambient temperatures.

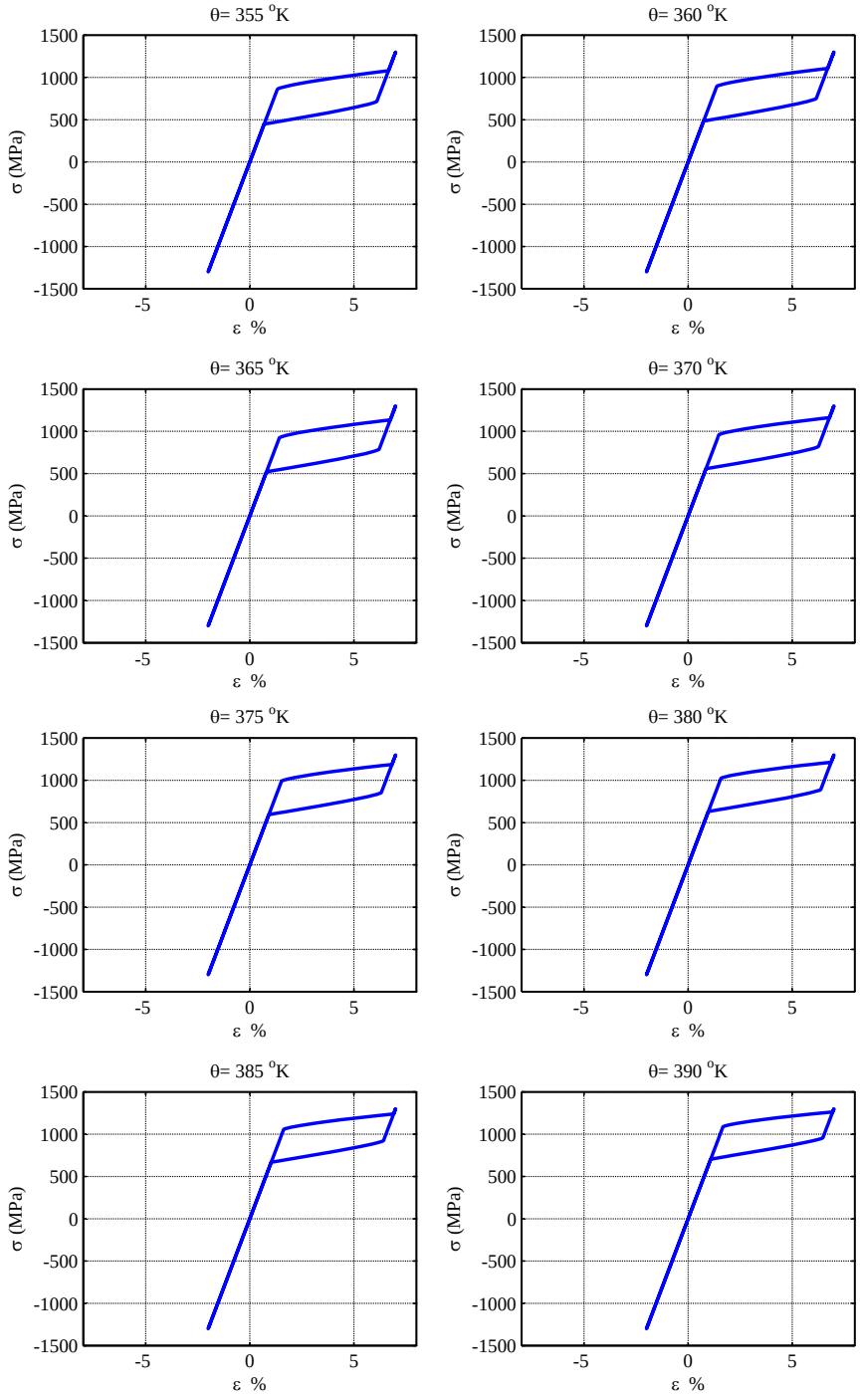

Figure 2.9: The stress-strain behavior at different ambient temperatures.

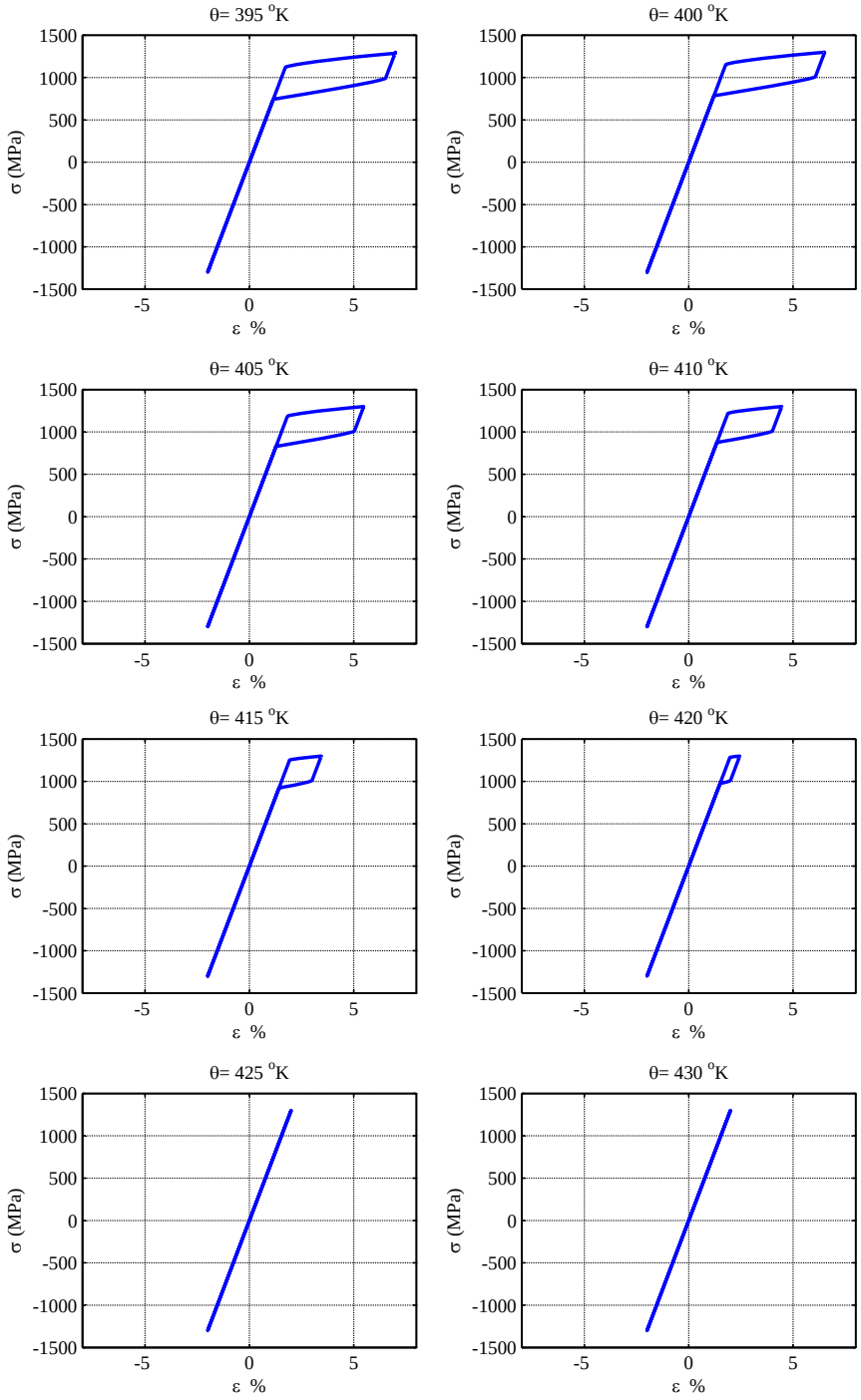

Figure 2.10: The stress-strain behavior at different ambient temperatures.

d_λ to the stress σ. In order to find the critical stress at which forward transformation from austenite to martensite starts one would write:

$$d_\lambda^+ = \sigma^{+^t}\varepsilon_m^t - \omega \quad \text{and} \quad d_\lambda^+ = \sigma^{+^c}\varepsilon_m^c - \omega \tag{2.40}$$

Solving for the critical stress:

$$\sigma^{+^t} = \frac{d_\lambda^+ + \omega}{\varepsilon_m^t} \quad \text{and} \quad \sigma^{+^c} = \frac{d_\lambda^+ + \omega}{\varepsilon_m^c}. \tag{2.41}$$

from (2.20) and (2.37) we have

$$\omega(\theta) = \frac{\mathcal{L}}{\theta_{cr}}(\theta - \theta_{cr}), \quad d_\lambda^+ = \mathcal{L}\left(\frac{A_s - M_s}{A_s + M_s}\right) \quad \text{and} \quad \theta_{cr} = \frac{A_s + M_s}{2}.$$

It follows that,

$$d_\lambda^+ + \omega(\theta) = \frac{\mathcal{L}}{\theta_{cr}}\left(\frac{A_s - M_s}{2} + \theta - \frac{A_s + M_s}{2}\right) = \frac{\mathcal{L}}{\theta_{cr}}(\theta - M_s) \tag{2.42}$$

which would be an equivalent for (2.41):

$$\sigma^{+^t} = \frac{\mathcal{L}}{\theta_{cr}\,\varepsilon_m^t}(\theta - M_s) \quad \text{and} \quad \sigma^{+^c} = \frac{\mathcal{L}}{\theta_{cr}\,\varepsilon_m^c}(\theta - M_s). \tag{2.43}$$

The above relation could also be easily derived from the Clausius − Clapeyron relation.

2.2.5 Effect of loading rate on the deformation behavior

Figure 2.11 shows the results of both the tensile and compressive half-cycles of loading at different loading rates. Each curve was generated by starting with the initial conditions (2.39), and carrying through the calculation for a tensile or compressive half-cycle of loading. As stress rate increases, the transformation begins at the same level of stress, but the stress increases relatively faster than the strain can evolve, giving rise to an apparent hardening and increase in the size of the hysteresis loop.

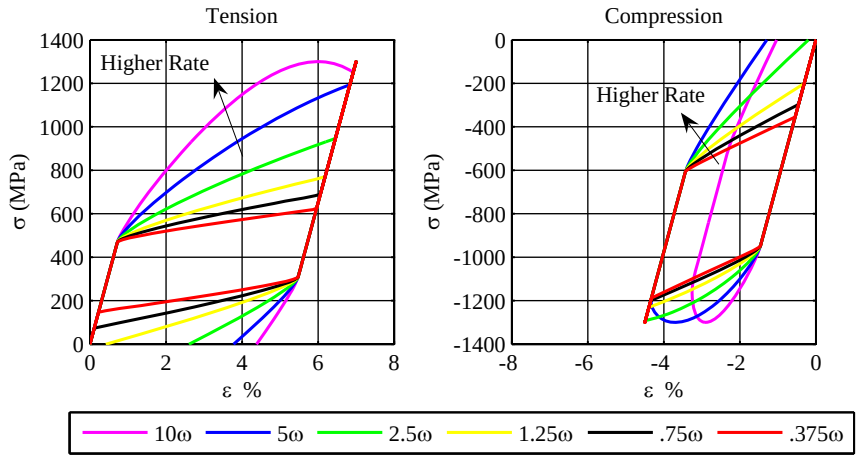

Figure 2.11: Tensile and compressive half-cycles at different loading rates, $\omega \mapsto 0.375\omega$, 0.75ω, 1.25ω, 2.5ω, 5ω, 10ω.

This hardening is a result of both the particular kinetic relation (specifically the rate dependence at high rates) and also an increase of temperature of the material. We shall examine the two effects separately below. At higher rates we also notice two other aspects. First, there is an apparent residual strain on full unloading. The reason is that the stress unloads too fast to allow for the completion of the reverse transformation. This is a consequence of the rate-dependence of the chosen kinetic relation at high rates. Second, at the highest rate (10ω), the material appears to soften as the loading proceeds. The reason is that the loading rate is so high that the transformation is not complete as the load increases to its peak and thus the transformation continues even as the load begins to decrease. All of these are consistent with observations in the literature (33).

Figure 2.12 shows the results of a full tension-compression cycle starting with tension.

Adiabatic heating affects the stress-strain response of the of shape-memory alloys. In order to properly interpret the effect of loading rate here we examine the relative role of the two factors that lead to the apparent hardening at high rates. Figure 2.13 shows the stress-strain response of the rate-independent (left) and rate-dependent (center) kinetic relations. The kinetic relations are shown on the right. The rate-

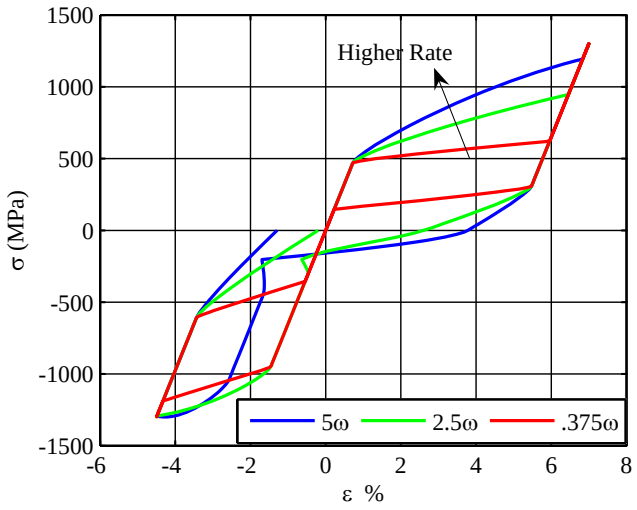

Figure 2.12: Complete tension-compression cycles at different loading rates, $\omega \mapsto 0.375\omega$, 2.5ω, 5ω.

dependent kinetic relation is the one stated earlier in (2.26). The rate-independent kinetic relation may be described as follows

$$|d_\lambda| \leq d_\lambda^+, \quad \dot{\lambda} = 0 \text{ if } |d_\lambda| < d_\lambda^+ \ , \tag{2.44}$$

and is shown as a dashed line on the right of Figure 2.13.

Let us begin with the rate-independent response shown on the left. If the loading is quasistatic and in fact slow enough to dissipate the latent heat so that the response is isothermal, one obtains the stress-strain response marked "Isothermal." As the loading rate increases, there is less time to dissipate the latent heat, and the temperature rises as the transformation progresses. Consequently the stress required to sustain the transformation increases with increasing volume fraction causing an apparent hardening. We eventually reach the response marked "Adiabatic." Further increase in loading rate does not change the response.

We can estimate the amount of hardening for this rate-independent situation. By combining the definition of driving force (2.23) with the constitutive assumption

(2.20) for ω, we obtain

$$d_\lambda \;=\; \sigma\varepsilon_m - \frac{\mathcal{L}}{\theta_{cr}}\left(\theta - \theta_{cr}\right) \;. \tag{2.45}$$

For rate-independent kinetics, (2.44), the driving force $d_\lambda = d_\lambda^+$ for transformation to proceed. Thus, the stress required for the transformation to proceed is given by

$$\sigma = \frac{d_\lambda^+}{\varepsilon_m} + \frac{\mathcal{L}}{\varepsilon_m \theta_{cr}}\left(\theta - \theta_{cr}\right) \;. \tag{2.46}$$

At the start of the transformation and for isothermal conditions, $\theta = \theta_0$. However, under adiabatic conditions, the temperature rises with transformation according to (2.33), so that final temperature at the completion of transformation is given by

$$\theta_f = \theta_0 \exp\left(\frac{\mathcal{L}}{c_p \theta_{cr}}\right) \;. \tag{2.47}$$

Thus the difference in stress between the start and finish of transformation during rate-independent adiabatic conditions[‡] is given by

$$\Delta\sigma \;=\; \frac{\theta_0\,\mathcal{L}}{\varepsilon_m\,\theta_{cr}}\left(\exp\left(\frac{\mathcal{L}}{c_p\theta_{cr}}\right) - 1\right) \;. \tag{2.48}$$

We now turn to the rate-dependent kinetic relation (2.26). The response is shown in the center of Figure 2.13. Under quasistatic, isothermal loading the response is identical to the rate-independent case and thus not shown. Since this kinetic relation is rate-independent for small rates, we first see a transition from isothermal to adiabatic, as before. Note that the response marked $.375\omega$ for the rate-dependent case is identical to the adiabatic response of the rate-independent case. On increasing the rate even further, we access the regime at which the kinetic relation becomes rate-dependent and thus observe further hardening.

In conclusion, both the transition from isothermal to adiabatic conditions as well as inherent rate dependence can give rise to hardening of the response with increasing

[‡]This is also equal to the difference in stress at the finish between adiabatic and isothermal conditions.

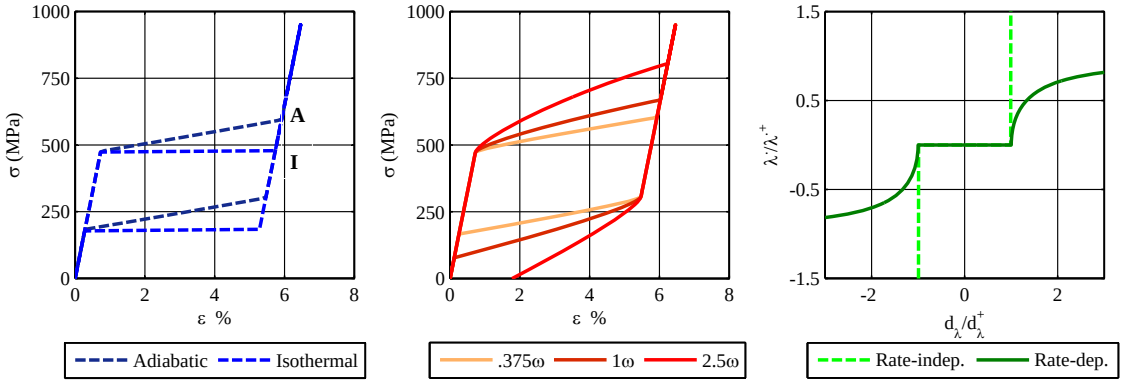

Figure 2.13: Comparison of the stress-strain relations for rate-independent (left) and rate-dependent (center) transformation kinetics. The two kinetic relations are shown on the right.

rate. However the former is limited to an increase of stress as described in (2.48). Any further hardening is necessarily a manifestation of inherent rate dependence of the transformation.

Figures 2.14 and 2.15 demonstrate how the power of the kinetic relation affects the stress-strain response for an isothermal as well as an adiabatic thermal condition.

2.2.6 Effect of plastic yield strength

The results discussed so far do not consider any plasticity since the yield strength was chosen to be higher than the maximum applied load. We now change that by taking the amplitude of loading to 800MPa and then taking a range of yield strengths from 350 MPa to 850 MPa. The results are shown in Figure 2.16. There is no plasticity as before when the yield strength is above stress amplitude ($\sigma_y = 850$ MPa). One begins to observe plasticity as the yield strength decreases. At $\sigma_y = 750, 650$ MPa, note that the yielding does not begin till the transformation is complete. The unloading is similar as before, though offset by the residual plastic strain and this remains as a permanent strain even after full unloading. At $\sigma_y = 550$ MPa, the transformation begins at 500 MPa, the plasticity begins at 550 MPa (indicated by an arrow) even before the transformation is complete, and proceeds even after the transformation is complete (again indicated by an arrow. At $\sigma_y = 350$ MPa, the yield begins at 350

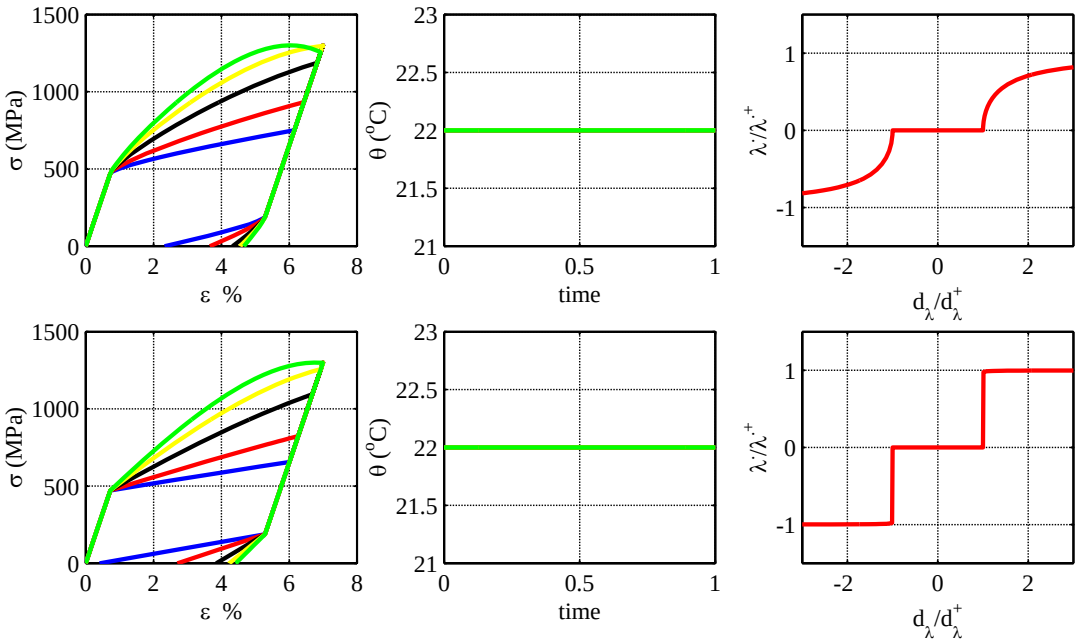

Figure 2.14: The effect of the power of the kinetic relation on the stress-strain response at loading rates: $\omega \mapsto 1.25\omega, 2.5\omega, 5\omega, 7.5\omega, 10\omega$ for an isothermal condition.

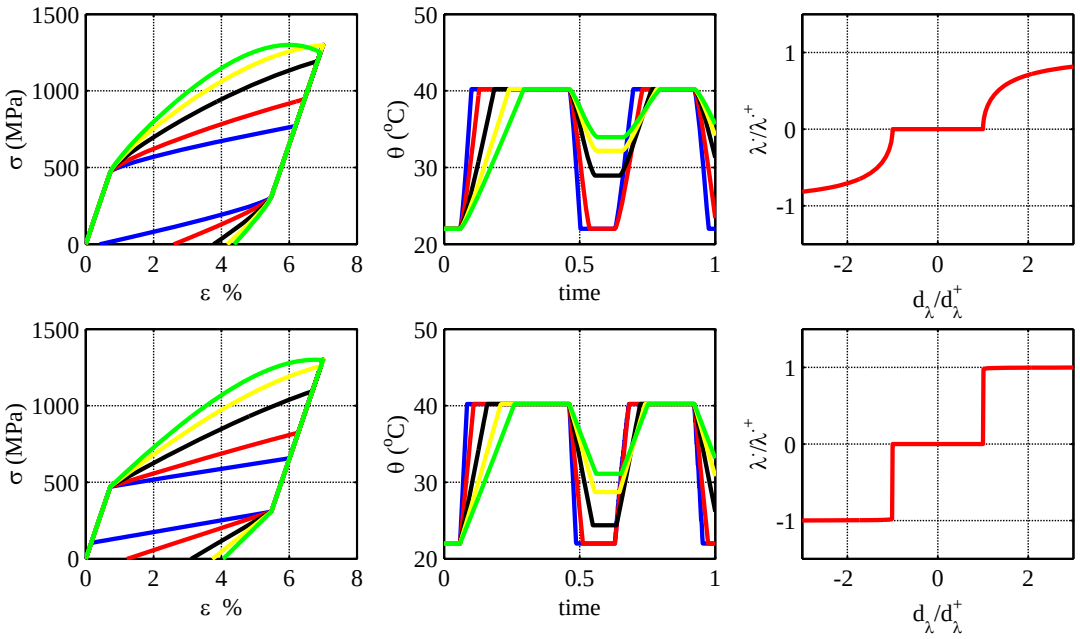

Figure 2.15: The effect of the power of the kinetic relation on the stress-strain response at loading rates: $\omega \mapsto 1.25\omega, 2.5\omega, 5\omega, 7.5\omega, 10\omega$ for an adiabatic condition.

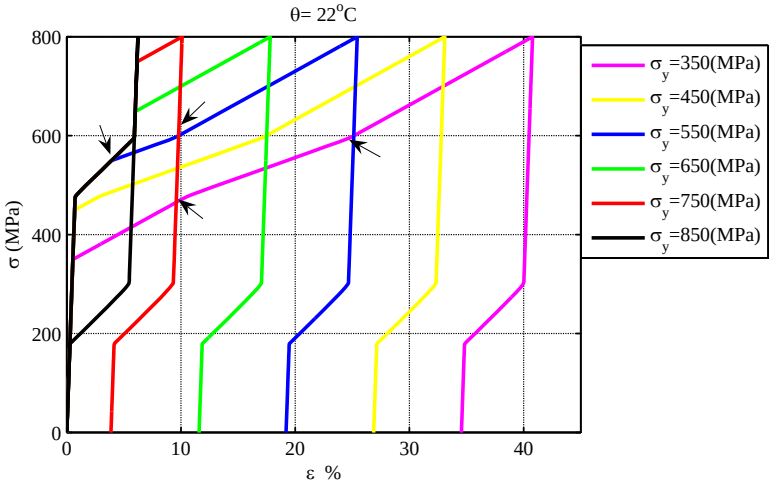

Figure 2.16: The stress-strain relations at different yield strength.

MPa, and continues as the transformation begins at 500 MPa (indicated by an arrow) and is complete (again indicated by an arrow). The unloading is as before.

2.2.7 Internal loops

Inspired by some experiments, we discuss internal loops of the stress-strain hysteresis for a simple triangular applied stress function. In Figure 2.17 the applied stress function σ is shown at the top left corner, the strain ε evolution at top right, the evolution of the martensitic volume fraction λ at the bottom left, and the stress-strain curves in the bottom right. The stress-strain curves consist of two parallel, linearly elastic branches and two almost horizontal lines where forward and reverse phase transformation happens. In particular, for the cases in which loading is interrupted before material is fully transformed to martensite, material starts unloading along a path parallel to the elastic loading-unloading branches and then starts the reverse phase transformation and goes back to the initial austenite phase at an almost constant stress level. This is consistent with the observations and arguments of Abeyaratne, Chu and James (1) but not with those of Huo and Müller (21).

We also note that some of the curves appear to show a softening. This is a consequence of the triangular applied load. The ramp-down begins before the trans-

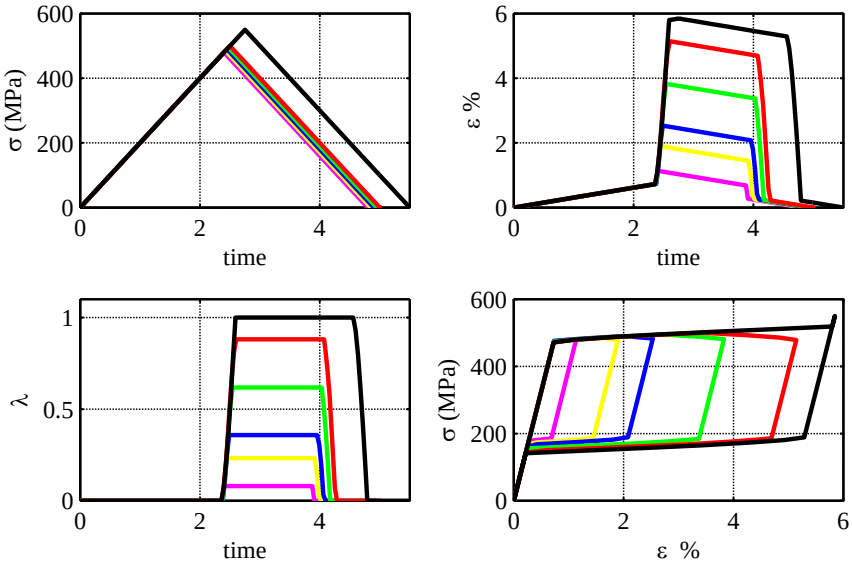

Figure 2.17: The internal hysteresis loops.

formation is complete: so during the initial ramp-down, the load is decreasing but still high enough for the transformation to continue giving rise to an apparent softening.

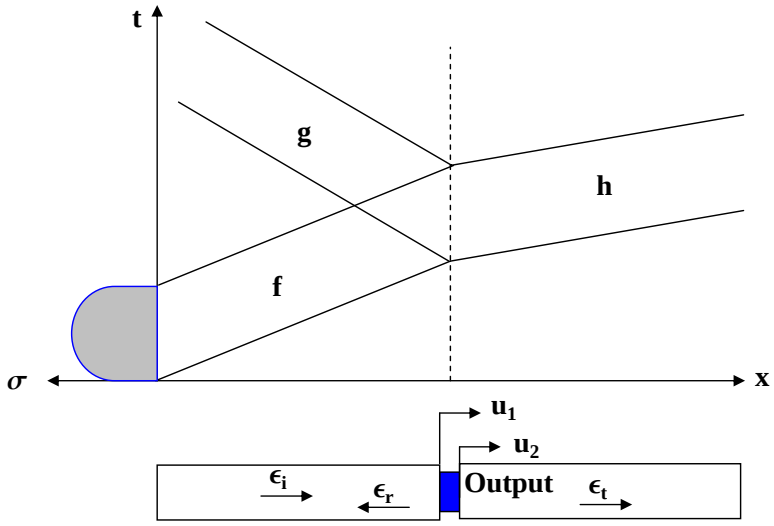

Figure 2.18: Kolsky bar and time-space diagram.

2.3 Kolsky bar

The previous section demonstrated the model under stress-control. However, this is difficult to attain experimentally. In materials like shape-memory alloys that involve the evolution of internal variables, the stress-strain curve varies with the methodology of the experiment. A particularly popular means of measuring material properties at high deformation rates is the Kolsky or split-Hopkinson bar. So we consider this in this section. It also serves the emphasize how sensitively the stress-strain curve can depend on the experimental methodology.

2.3.1 Kolsky bar

In the Kolsky or split-Hopkinson bar experiment shown in Figure 2.18, a thin specimen is placed between an incident bar (left) and output bar (right), both made of a linear elastic material and designed to have very little dispersion. A compression stress wave of known amplitude, duration and shape is generated in an incident bar through a striker bar (not shown). As this wave reaches the specimen, a portion is reflected while another portion is transmitted into the output bar. The length of the specimen is very small compared to the ratio of the wave speed to the duration of the

pulse so that one may assume that the specimen is in equilibrium at any given time.

Since the input bar is linear elastic, the displacement in the bar is of the form

$$u_L(x,t) = f(x-ct) + g(x+ct) \tag{2.49}$$

so that the strain, the stress and the particle velocity are given by

$$\begin{aligned}
\varepsilon_L(x,t) &= (u_L)_{,x}(x,t) = f'(x-ct) + g'(x+ct) && (2.50)\\
\sigma_L(x,t) &= E_b\,(f'(x-ct) + g'(x+ct)) && (2.51)\\
v_L(x,t) &= (u_L)_{,t}(x,t) = c(-f'(x-ct) + g'(x+ct)) && (2.52)
\end{aligned}$$

that includes both the incident and reflected waves. Above, the prime ($'$) denotes differential with respect to its native variable. Similarly, the output bar is linear elastic and

$$\begin{aligned}
u_R(x,t)_{left} &= h(x-ct) && (2.53)\\
\varepsilon_R(x,t) &= h'(x-ct) && (2.54)\\
\sigma_R(x,t) &= E_b\,h'(x-ct) && (2.55)\\
v_R(x,t) &= -c\,h'(x-ct) && (2.56)
\end{aligned}$$

since there is only a transmitted wave. Assuming the equilibrium of the specimen, the stress in the specimen is uniform and one has continuity of forces so that

$$\sigma(t)A_s = \sigma_L(0,t)A_b = \sigma_R(0,t)A_b, \tag{2.57}$$

where A_s and A_b are the cross-sectional areas of specimen and the input/output bars, respectively. Further, the overall strain in the specimen is given as

$$\varepsilon = \frac{u_R(0,t) - u_L(0,t)}{l_s} \tag{2.58}$$

where l_s is the length of the specimen. It follows that

$$\sigma(t) = \frac{E_b\,A_b}{A_s}(f'(-ct)+g'(+ct)) = \frac{E_b\,A_b}{A_s}h'(-ct), \tag{2.59}$$

$$\dot{\varepsilon}(t) = \frac{c(-h'(-ct)+f'(-ct)-g'(ct))}{l_s}. \tag{2.60}$$

In a typical Kolsky bar experiment, f is applied, g and h are measured, and (2.59), (2.60) are used to obtain the stress and strain rate.

To further simplify these equations we start with the second relation in (2.59) and rewrite it as follows:

$$f'(-ct)+g'(+ct) = h'(-ct) \quad \Rightarrow \quad g'(+ct) = h'(-ct)-f'(-ct). \tag{2.61}$$

This would simplify (2.59) and (2.60) to:

$$\sigma(t) = \frac{E_b\,A_b}{A_s}h'(-ct), \tag{2.62}$$

$$\dot{\varepsilon}(t) = \frac{2\,c\,(-h'(-ct)+f'(-ct))}{l_s}. \tag{2.63}$$

Our purpose here is to see how a material described by our model would behave when subjected to a Kolsky bar experiment. So we apply a given input pulse $f(t)$, integrate equations (2.62) and (2.63) and apply (2.21), (2.26), (2.27), (2.28) and (2.33) to obtain h, σ, ε, ε_m, ε_p, λ and θ. Reflected wave profile g can also be derived by applying (2.61). The initial conditions are the same as before. We choose the same parameters as described in the previous section. Further,

$$\begin{aligned} \text{Diameter}_{\text{specimen}} &= 1.5 \text{ cm} \quad \text{and} \quad \text{Diameter}_{\text{kolsky bars}} = 2 \text{ cm} \\ E_{\text{specimen}} &= 65 \text{ GPa} \quad \text{and} \quad E_{\text{kolsky bars}} = 200 \text{ GPa} \\ \text{Length}_{\text{specimen}} &= 0.5 \text{ cm} \quad \text{and} \quad \text{Wave Speed}_{\text{specimen}} = 3500 \text{ m/s}\ . \end{aligned} \tag{2.64}$$

The yield strength is chosen high enough so that plasticity plays no role. We assume that the incident wave f' is a square pulse with amplitude 1.5×10^{-3}, duration

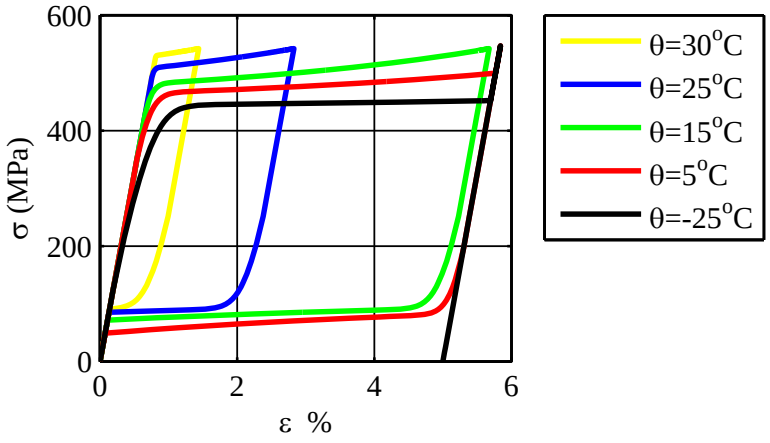

Figure 2.19: The effect of ambient temperature on stress-strain response.

50×10^{-4} sec and rise time 50×10^{-6} sec unless otherwise stated.

2.3.2 Ambient temperature

Figure 2.19 shows the result for different ambient (initial) temperatures. The critical stress at which phase transformation starts, rises as temperature increases. Therefore at the highest temperature displayed, 30°C, the transformation begins very late, just before the unloading. Therefore the material does not have enough time to transform fully, and consequently the amount of strain is small. It fully transforms back on unloading. As the ambient temperature drops, the transformation begins earlier and thus proceeds further, and the amount of strain increases. It continues to transform back fully except at the lowest displayed temperature of -25°C.

Notice that the shapes of the stress-strain curves are less boxy than those obtained with the given stress history in the previous section. This is our first indication that the stress-strain curve can depend on experimental methodology.

2.3.3 Pulse amplitude, size and shape

Figure 2.20 shows the effect of changing the pulse amplitude, while Figure 2.21 shows the effect of changing pulse duration. As expected, the transformation is incomplete with smaller or shorter pulses. Figure 2.22 shows the stress-strain curve for various

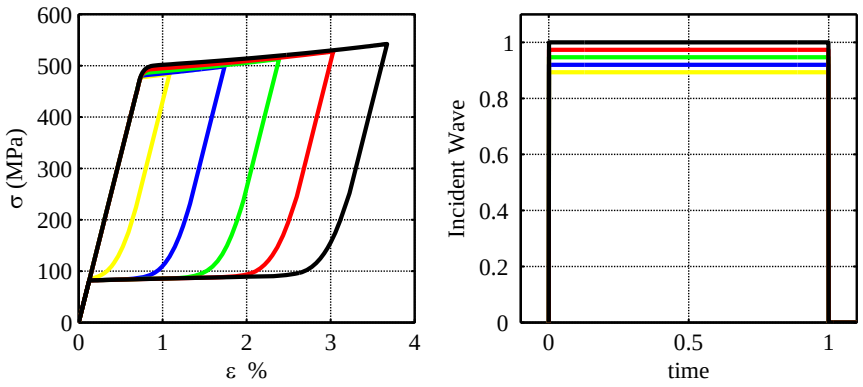

Figure 2.20: Pulse amplitude's effect in stress-strain hysteresis. The amplitude and pulse duration are normalized with those described in (2.64).

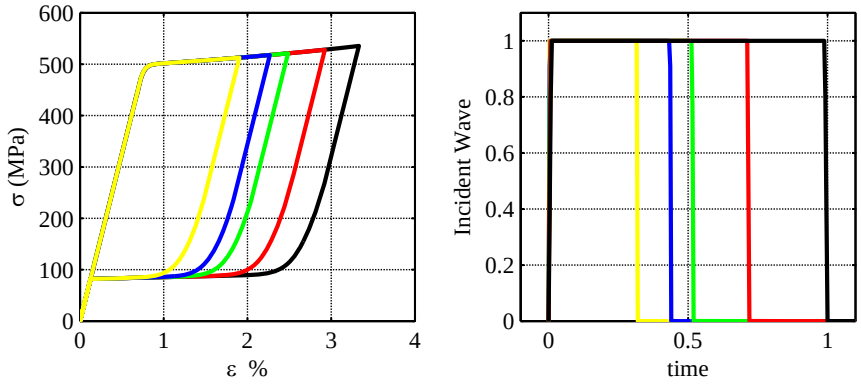

Figure 2.21: Pulse duration's effect in stress-strain hysteresis. The amplitude and pulse duration are normalized with those described in (2.64).

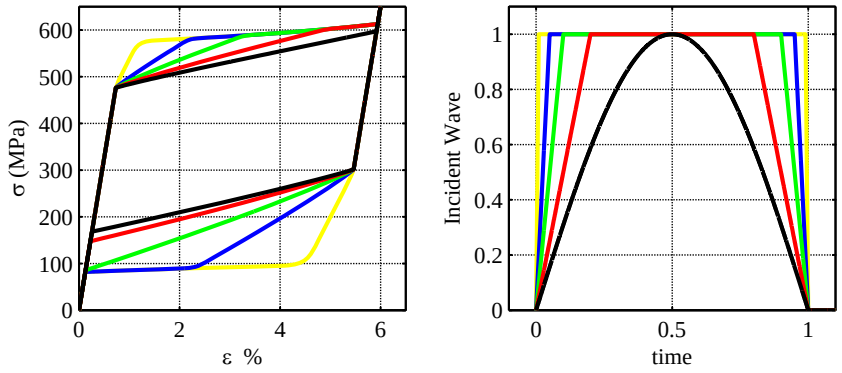

Figure 2.22: The effect of the pulse shape in stress-strain hysteresis. The amplitude and pulse duration are normalized with those described in (2.64).

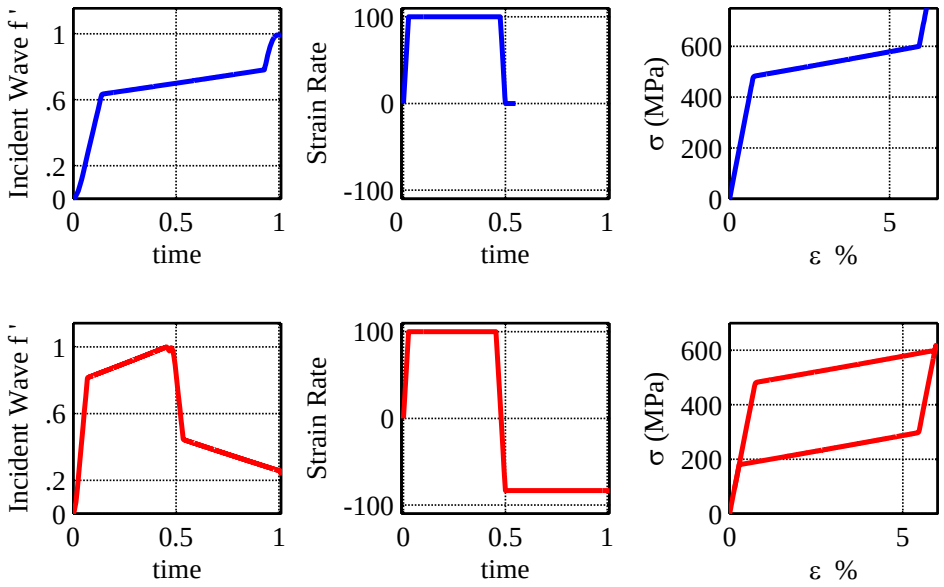

Figure 2.23: Design of the strain rate in the specimen.

pulse shapes. The shape of the stress-strain curve can vary widely with the input pulse.

This points to the importance of designing an appropriate pulse shape in experiments. The strain rate of the shape-memory alloy sample varies significantly as its microstructure changes and obtaining a constant strain rate during the austenite to martensite phase transformation in experiments is an issue of concern (33). We address this by using the model to design a pulse that yields a desired strain rate history. We set our given strain rate $\dot{\varepsilon}(t)$ and integrate equations (2.62) and (2.63) to solve for the incident f and transmitted h waves. The reflected wave g can also be derived by using (2.61) when f and h are quantified. We will apply (2.21), (2.26), (2.27), (2.28) and (2.33) to obtain σ, ε_m, ε_p, λ and θ. The initial conditions are the same as before. The results are shown in Figure 2.23 for two desired strain rates. The first is a constant strain rate to investigate the loading. Note that the pulse can not have constant amplitude but has to increase gradually in amplitude. The second is a jump test to study both the loading and the unloading. Note that the wave profile on the left is normalized and we are in fact plotting the slope f', which is unitless rather than the incident wave profile f.

Chapter 3

Three-Dimensional Constitutive Model for Shape-Memory Alloys

3.1 Constitutive Model

In this chapter, we develop and discuss a three-dimensional constitutive model within a continuum thermodynamic framework for polycrystalline shape-memory alloys. Micromechanics origins of the model, the concepts emerged from those analysis and their relation to macroscopic properties in both single and polycrystals are presented.

3.1.1 Kinematics

Similar to the previous chapter, we use two kinematic or field or internal variables to represent the consequence of microstructure in an RVE: the *volume fraction of martensite*, $\lambda(x,t)$, and the *effective transformation strain of the martensite*, $\varepsilon_m(x,t)$.

$\lambda(x,t)$ remains a scalar and is constrained to take values between 0 and 1. However $\varepsilon_m(x,t)$ is now a symmetric second-order tensor. It is constrained to lie inside a set P, the set of all possible effective transformation strains. We postpone a detailed discussion of this set till section 3.1.4, but note for now that it is a convex set in the space of symmetric trace-free second-order matrices. Thus,

$$\lambda \in [0,1] \quad \text{and} \quad \varepsilon_m \in P. \tag{3.1}$$

It is worth noting that the effective transformation strain of the RVE is $\lambda\varepsilon_m$ since λ is the volume fraction of martensite, ε_m is the effective transformation strain of the martensite and the transformation strain of the austenite is zero by choice of reference configuration.

Finally, we introduce the plastic strain tensor ε_p as an additional field variable. Putting everything together, we say that the total strain can be divided into three parts, elastic, transformation and plastic:

$$\varepsilon(x,t) = \frac{1}{2}(\nabla u + \nabla u^T) = \varepsilon_e(x,t) + \lambda(x,t)\varepsilon_m(x,t) + \varepsilon_p(x,t). \tag{3.2}$$

3.1.2 Balance laws

We assume that the usual balance laws hold. In local form, the balance of linear momentum and energy may be stated as

$$\rho u_{tt} = \text{div} \tag{3.3}$$

$$\sigma\dot{\epsilon} = -\nabla q + r + \sigma : \dot{\varepsilon}\,. \tag{3.4}$$

where ρ is the (referential) mass per unit length, σ is the (Piola-Kirchhoff) stress, ϵ is the internal energy density, q the heat flux and r the radiative heating.

(3.5)

We also use the local form of the second law of thermodynamics,

$$-\dot{W} - \eta\dot{\theta} + \sigma : \dot{\varepsilon} - \frac{q\nabla\theta}{\theta} \geq 0\,, \tag{3.6}$$

where $W = \epsilon - \theta\eta$ is the Helmholtz free energy density, η the entropy density and θ the (absolute) temperature.

3.1.3 Constitutive relations, driving forces and kinetic relations

We assume that the Helmholtz free energy density depends on the strain, the temperature and the internal variables:

$$W = W(\varepsilon, \lambda, \varepsilon_m, \varepsilon_p, \theta). \tag{3.7}$$

Specifically, we assume,

$$W = \frac{1}{2}\left(\varepsilon - \varepsilon_p - \lambda\,\varepsilon_m\right) C \left(\varepsilon - \varepsilon_p - \lambda\,\varepsilon_m\right) + \lambda\,\omega(\theta) - c_p\,\theta \ln\left(\frac{\theta}{\theta_0}\right) \tag{3.8}$$

where C is a fourth-order tensor denoting the elastic modulus (assumed to be equal in both the austenite and the martensite), ω is the difference in chemical energy between the austenite and the martensite, c_p is the heat capacity (assumed to be equal in both the austenite and the martensite), and ordinary thermal expansion is neglected. This relation is illustrated in Figure 2.1. We further assume that

$$\omega(\theta) = \frac{\mathcal{L}}{\theta_{cr}}(\theta - \theta_{cr}) \tag{3.9}$$

where $\mathcal{L}$ is the latent heat of transformation and θ_{cr} is the thermodynamic transformation temperature. Arguing as in chapter 2, we obtain

$$\begin{aligned}
\sigma &= C(\varepsilon - \varepsilon_p - \lambda\,\varepsilon_m), && (3.10)\\
\eta &= \lambda\frac{\mathcal{L}}{\theta_{cr}} - c_p\left(1 + \ln\left(\frac{\theta}{\theta_0}\right)\right), && (3.11)\\
d_\lambda &= \sigma : \varepsilon_m - \omega, && (3.12)\\
d_{\varepsilon_m} &= \lambda\sigma, && (3.13)\\
d_{\varepsilon_p} &= \sigma. && (3.14)
\end{aligned}$$

where d_λ, d_{ε_m} and d_{ε_p} denote the driving forces associated with the rates of change of their conjugate internal variables, λ, ε_m and ε_p respectively.

The kinetic relation describing the evolution of the martensite volume fraction λ is taken to be the following:

$$\dot{\lambda} = \begin{cases} \dot{\lambda}^+ \left(1 + \left(d_\lambda - d_\lambda^+\right)^{-1}\right)^{-\frac{1}{p}} & d_\lambda > d_\lambda^+ \text{ and } \lambda < 1 \\ \dot{\lambda}^- \left(1 + \left(d_\lambda^- - d_\lambda\right)^{-1}\right)^{-\frac{1}{p}} & d_\lambda < d_\lambda^- \text{ and } \lambda > 0 \\ 0 & \text{otherwise.} \end{cases} \tag{3.15}$$

where $\dot{\lambda}^\pm, d_\lambda^\pm, p$ are material parameters. This relation is shown in Figure 2.2 and its nature is discussed in section 2.1.4.

We assume the following plasticity relation:

$$\dot{\varepsilon}_p = K_{\varepsilon_p}\left(d_{\varepsilon_p}, \text{ yield surface}\right) = \frac{\dot{d_{\varepsilon_p}}}{H} = \begin{cases} \frac{\dot{\sigma}}{H} & \sigma \in \text{yield surface} \\ 0 & \text{otherwise.} \end{cases} \tag{3.16}$$

where H is the hardening parameter.

The evolution of the effective transformation strain ε_m describes the twinning, detwinning and other such processes that convert one martensitic variant to another. We assume a rather simple law for its evolution:

$$\dot{\varepsilon}_m = K_{\varepsilon_m}\left(d_{\varepsilon_m}, \lambda, \varepsilon_m\right) = \begin{cases} \frac{\alpha}{\lambda}\, d_{\varepsilon_m} & \varepsilon_m \in \breve{\mathrm{P}} \\ \frac{\alpha}{\lambda}\left(d_{\varepsilon_m}\right)_{\partial P} & \varepsilon_m \in \partial P \\ 0 & \text{otherwise} \end{cases} \tag{3.17}$$

where $\breve{\mathrm{P}}$ denotes the interior of P, ∂P the boundary of P and $A_{\partial P}$ the projection of A to the tangent space of P. There are subtleties associated with this statement which we presently discuss.

3.1.4 Set of effective transformation strains

In general the transformation strain ε_m is a symmetric tensor and thus has six independent components. It may appear therefore that we need a six-dimensional transformation strain space to represent the set of effective transformation strains.

Self-accommodation, however, dictates that the transformation strain ε_m tensor is trace-free (8). It follows then that the set P lives on a subspace five-dimensional space of trace-free symmetric matrices. Therefore viewed as a six-dimensional object, $\breve{\mathrm{P}}$, the interior of P, is empty.

Further the tangent space is always contained in the five-dimensional subspace of trace-free symmetric tensors or deviatoric tensors. Therefore, it is convenient to restrict ourselves to the five-dimensional space of deviatoric tensors and rewrite (3.17) as

$$\dot{\varepsilon}_m = K_{\varepsilon_m}(d_{\varepsilon_m},\, \lambda,\, \varepsilon_m) = \begin{cases} \frac{\alpha}{\lambda}\,\hat{d}_{\varepsilon_m} & \varepsilon_m \in \breve{\mathrm{P}} \\ \frac{\alpha}{\lambda}\,(\hat{d}_{\varepsilon_m})_{\partial P} & \varepsilon_m \in \partial P \\ 0 & \text{otherwise} \end{cases} \tag{3.18}$$

where $\breve{\mathrm{P}}$ and ∂P are interpreted as the relative interior and relative boundary to this subspace, and $\hat{A}$ is the deviatoric part of the tensor A.

To elaborate on this point, suppose we define P through the following relation

$$P = \{\varepsilon_m | tr(\varepsilon_m) = 0,\, g(\varepsilon_m) \leq 0\} \tag{3.19}$$

for a suitable $g : \mathbb{R}^{3\times 3}_{\text{dev}} \to \mathbb{R}$. Then,

$$\dot{\varepsilon}_m = \begin{cases} \frac{\alpha}{\lambda}\hat{d}_{\varepsilon_m} & g(\varepsilon_m) < 0 \\ \frac{\alpha}{\lambda}(\hat{d}_{\varepsilon_m} - \hat{d}_{\varepsilon_m} : \frac{\partial g}{\partial \varepsilon_m} \frac{\frac{\partial g}{\partial \varepsilon_m}}{|\frac{\partial g}{\partial \varepsilon_m}|^2}) & g(\varepsilon_m) = 0 \\ 0 & \text{otherwise.} \end{cases} \tag{3.20}$$

Recalling that $d_{\varepsilon_m} = \lambda\,\sigma$ from (3.13),

$$\dot{\varepsilon}_m = \begin{cases} \alpha\hat{\sigma} & g(\varepsilon_m) < 0 \\ \alpha(\hat{\sigma} - \hat{\sigma} : \frac{\partial g}{\partial \varepsilon_m} \frac{\frac{\partial g}{\partial \varepsilon_m}}{|\frac{\partial g}{\partial \varepsilon_m}|^2}) & g(\varepsilon_m) = 0 \\ 0 & \text{otherwise.} \end{cases} \tag{3.21}$$

We now discuss, three specific constitutive relations for P.

3.1.4.1 Isotropic and symmetric transformation

Isotropy states that

$$g(\varepsilon_m) = g(\, R^T \, \varepsilon_m \, R \,). \tag{3.22}$$

for all rotations R. This implies that we can define the transformation strain function, $g(\varepsilon_m)$ by three principal values of the transformation strain, or its three invariants $I_1(\varepsilon_m)$, $I_2(\varepsilon_m)$ and $I_3(\varepsilon_m)$ where,

$$\begin{aligned} I_1(\varepsilon_m) &= tr(\varepsilon_m), & (3.23)\\ I_2(\varepsilon_m) &= \frac{1}{2}\,[tr(\varepsilon_m)^2 - \, tr({\varepsilon_m}^2)], & (3.24)\\ I_3(\varepsilon_m) &= det(\varepsilon_m). & (3.25) \end{aligned}$$

As mentioned earlier, self-accommodation asks the transformation strain ε_m to be trace-free, which forces $I_1(\varepsilon_m)$ to vanish, which simplifies $I_2(\varepsilon_m)$ as follows:

$$I_2(\varepsilon_m) \;=\; -\frac{1}{2}\, tr({\varepsilon_m}^2). \tag{3.26}$$

For an isotropic alloy with tension-compression symmetry the following would be a reasonable choice for the set of effective transformation strains:

$$P = \{\varepsilon_m | tr(\varepsilon_m) = 0,\; g(\varepsilon_m) = I_2(\varepsilon_m) - \, b \leqslant 0\}. \tag{3.27}$$

Equations (3.17) and (3.27) give the growth rule for the transformation strain as

$$\dot{\varepsilon}_m = \begin{cases} \alpha\hat{\sigma} & |\varepsilon_m| < \sqrt{2\,b} \\ \alpha(\hat{\sigma} - \, \varepsilon_m \, \frac{\varepsilon_m : \hat{\sigma}}{|\varepsilon_m|^2}) & |\varepsilon_m| = \sqrt{2\,b} \\ 0 & \text{otherwise.} \end{cases} \tag{3.28}$$

3.1.4.2 Isotropic and asymmetric transformation

Obviously $I_2(\varepsilon_m)$ does not change sign as transformation strain changes sign and a set of effective transformation strains solely based on $I_2(\varepsilon_m)$ would not allow tension-compression asymmetry to appear. This is why in general one would prefer using a $g(\varepsilon_m)$ function, where

$$g(\varepsilon_m) = g(I_2(\varepsilon_m),\, I_3(\varepsilon_m)). \tag{3.29}$$

This changes the set of recoverable strains to

$$P = \{\varepsilon_m | tr(\varepsilon_m) = 0,\, g(\varepsilon_m) = (-I_2(\varepsilon_m))^{\frac{3}{2}} - a\, I_3(\varepsilon_m) - \, b \leqslant 0\}. \tag{3.30}$$

Equations (3.17) and (3.30) give the growth rule for the transformation strain as

$$\dot{\varepsilon}_m = \begin{cases} \alpha\hat{\sigma} & g(\varepsilon_m) < 0 \\ \alpha(\hat{\sigma} - \, (\frac{3\,|\varepsilon_m|}{\sqrt{8}}\,\varepsilon_m - \, a\,\mathrm{cof}(\varepsilon_m)^T)\,\frac{(\frac{3\,|\varepsilon_m|}{\sqrt{8}}\,\varepsilon_m - a\,\mathrm{cof}(\varepsilon_m)^T):\hat{\sigma}}{|(\frac{3\,|\varepsilon_m|}{\sqrt{8}}\,\varepsilon_m - a\,\mathrm{cof}(\varepsilon_m)^T)|^2}) & g(\varepsilon_m) = 0 \\ 0 & \text{otherwise.} \end{cases} \tag{3.31}$$

3.1.4.3 Anisotropic and asymmetric transformation

In some circumstances such as for alloys that have been reduced in thickness by cold rolling in one direction, the introduction of a degree of anisotropy in the theory is necessary. In the isotropic case when $g(\varepsilon_m) = g(R^T\,\varepsilon_m\,R)\ \forall R$ we get $g(\varepsilon_m) = g(I_1(\varepsilon_m),\, I_2(\varepsilon_m),\, I_3(\varepsilon_m))$, which along with the self-accommodation of transformation strain tensor ε_m simplifies $g(\varepsilon_m)$ to the form (3.29). For the anisotropic case when $g(\varepsilon_m) = g(R^T\,\varepsilon_m\,R)\ \forall R\,\hat{e} = \hat{e}$ we have

$$g(\varepsilon_m) = g(I_2(\varepsilon_m),\, I_3(\varepsilon_m),\, \hat{e}\cdot\varepsilon_m\,\hat{e},\, \hat{e}\cdot{\varepsilon_m}^2\,\hat{e}). \tag{3.32}$$

Here we propose to work with the following form:

$$g(\varepsilon_m) = (-I_2(\varepsilon_m))^{\frac{3}{2}} - a\, I_3(\varepsilon_m) - \ b - \ c\,(\hat{e}\cdot\varepsilon_m\,\hat{e})^3. \tag{3.33}$$

This changes the set of recoverable strains to

$$P = \{\varepsilon_m | tr(\varepsilon_m) = 0,\ g(\varepsilon_m) = (-I_2(\varepsilon_m))^{\frac{3}{2}} - a\, I_3(\varepsilon_m) - \ b - \ c\,(\hat{e}\cdot\varepsilon_m\,\hat{e})^3\}. \tag{3.34}$$

This changes the growth rule for the transformation strain (3.31) to

$$\dot{\varepsilon}_m = \begin{cases} \frac{\alpha}{\lambda}\,\hat{d}_{\varepsilon_m} & g(\varepsilon_m) < 0 \\ \frac{\alpha}{\lambda}\,(\hat{d}_{\varepsilon_m} \ - \ \frac{\hat{d}_{\varepsilon_m} : \frac{\partial g}{\partial \varepsilon_m}}{|\frac{\partial g}{\partial \varepsilon_m}|^2}) & g(\varepsilon_m) = 0 \\ 0 & \text{otherwise,} \end{cases} \tag{3.35}$$

where

$$\frac{\partial g}{\partial \varepsilon_m} = \frac{3\,|\varepsilon_m|}{\sqrt{8}}\,\varepsilon_m - \ a\,\mathrm{cof}(\varepsilon_m)^T - \ 3\,c\,(\hat{e}\cdot\hat{e})\,(\hat{e}\cdot\varepsilon_m\,\hat{e})^2. \tag{3.36}$$

The interesting interplay of parameters a, b and c and their impact on the shape of the set of recoverable transformation strains be reviewed later in this chapter. Having defined the set of recoverable strains and evolution of the transformation strain, we describe how to find the critical stress where phase transformation is triggered.

3.1.5 Temperature evolution

The energy balance, along with the constitutive relations describe the evolution of the temperature. Specializing to the specific constitutive relation and in particular (3.11), we obtain

$$c_p\dot{\theta} = \dot{\lambda}\theta\frac{\mathcal{L}}{\theta_{cr}} - \nabla q + r + d_\lambda\dot{\lambda} + d_{\varepsilon_m} : \dot{\varepsilon}_m + d_{\varepsilon_p} : \dot{\varepsilon}_p. \tag{3.37}$$

3.1.5.1 Adiabatic conditions

For processes where heat transfer is negligible we have ($q = r = 0$). Further, it turns out that the latent heat of transformation is large compared to the energy dissipated during transformation, martensitic variant reorientation and plasticity during typical processes of interest. Therefore we assume

$$c_p\dot{\theta} \;=\; \theta\dot{\lambda}\frac{\mathcal{L}}{\theta_{cr}} \tag{3.38}$$

Integrating this, we obtain a relation between temperature, volume fraction of martensite, latent heat and specific heat:

$$\theta(t) \;=\; \theta_0 \exp\left(\frac{(\lambda(t)-\lambda_0)\mathcal{L}}{c_p\theta_{cr}}\right). \tag{3.39}$$

3.1.5.2 Non-adiabatic conditions

Under non-adiabatic thermal conditions radiative heating r is no longer equal to zero and in (3.37) we replace it with

$$r = -\frac{4h}{d_s}\,(\theta-\theta^*). \tag{3.40}$$

where h is the convection heat transfer coefficient and for the air it is normally 10 to 100 $\frac{\mathrm{J}}{\mathrm{m^2\,K\,s}}$. Parameter d_s is the diameter of the specimen for a cylinder sample and θ^* is the ambient temperature. This changes (3.38) to

$$c_p\dot{\theta} \;=\; \theta\dot{\lambda}\frac{\mathcal{L}}{\theta_{cr}} + r \Rightarrow c_p\dot{\theta} \;=\; \theta\dot{\lambda}\frac{\mathcal{L}}{\theta_{cr}} - \frac{4h}{d_s}\,(\theta-\theta^*). \tag{3.41}$$

Integrating this, we obtain a relation between temperature, volume fraction of martensite, latent heat, specific heat and convection heat transfer coefficient:

$$\theta(t) \;=\; \exp^{\int_0^t (\frac{\mathcal{L}}{c_p\,\theta_{cr}}\,\dot{\lambda}(\tau) - \frac{4h}{c_p\,d_s})d\tau}\left(\theta_0 \;-\; \int_0^t \frac{4h}{c_p\,d_s}\,\exp^{-\int_0^\tau (\frac{\mathcal{L}}{c_p\,\theta_{cr}}\,\dot{\lambda}(\tau^*) - \frac{4h}{c_p\,d_s})d\tau^*}\,d\tau\right) \tag{3.42}$$

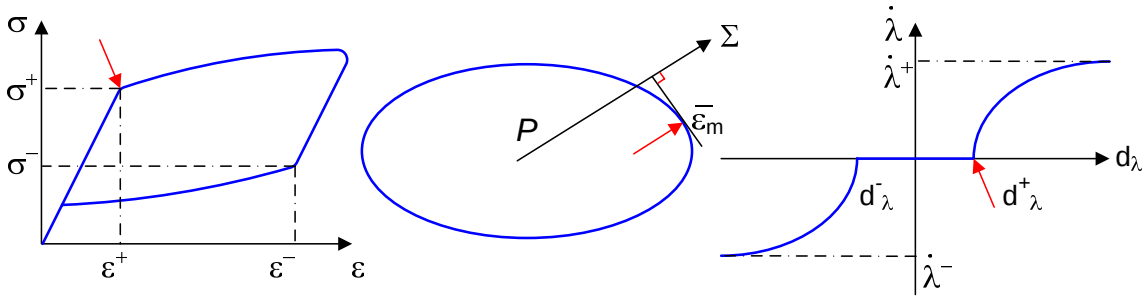

Figure 3.1: Initiation of the forward martensitic phase transformation.

3.1.6 Critical phase transformation stress

Consider a specimen of shape memory material in the austenite state ($\lambda = 0$) and above M_s subjected to some proportional loading

$$\sigma = s\,\Sigma. \tag{3.43}$$

for $s > 0$ and monotone increasing. Since we have chosen α to be so large that ε_m evolves much faster than stress, ε_m reaches the boundary ∂P of the set of recoverable phase transformation strains quickly and then evolves along it till the normal to ∂P becomes parallel to Σ. This value $\overline{\varepsilon_m}$, does not evolve any further for constant normalized Σ stress direction tensor and solves the following problem:

$$\max_{\varepsilon_m \in P} (\sigma : \varepsilon_m) \;=\; s \max_{\varepsilon_m \in P} (\Sigma : \varepsilon_m). \tag{3.44}$$

The driving force for transformation is then given by (3.12)

$$d_\lambda = \sigma : \overline{\varepsilon_m} - \omega = s \max_{\varepsilon_m \in P} (\Sigma : \varepsilon_m) - \omega. \tag{3.45}$$

Transformation begins when $d = d_\lambda^+$. Then it follows that the initial stress for transformation is given by

$$s_c = (d_\lambda^+ + \omega) / \max_{\varepsilon_m \in P} (\Sigma : \varepsilon_m). \tag{3.46}$$

This defines the radial extent of the transformation yield surface in stress space and along the given stress direction Σ. Figure 3.1 shows how this point is related to corresponding points on the stress-strain hysteresis and the kinetic law.

3.2 Demonstration of the isotropic model

In this section we confine our simulations with the assumption of isotropy, suitable for polycrystalline shape-memory alloys where the degree of anisotropy developed during the phase transformation process is negligible. We demonstrate how to derive the transformation surface in this model, conduct a parameter study and present a series of proportional and non-proportional loading simulations. We then demonstrate the effects of temperature by studying the adiabatic and non-adiabatic thermal conditions.

3.2.1 Parameters

Consistent with typical experiments on NiTi (see for example (31)), we consider the following parameters:

$$\begin{aligned} M_s &= -51.55\,^oC \quad \text{and} \quad A_s = -6.36\,^oC \\ \mathcal{L} &= 79\ (\frac{\text{MJ}}{\text{m}^3}) \quad \text{and} \quad c_p = 5.4\ (\frac{\text{MJ}}{\text{m}^3\,^o\text{K}}) \\ E &= 65\ (\text{GPa}) \quad \text{and} \quad \sigma_y = 1500\ (\text{MPa}) \end{aligned} \tag{3.47}$$

where M_s and A_s are the martensite start and austenite start temperatures, respectively. Recalling (3.15) and (3.12), we obtain

$$d_\lambda^+ = -\omega(M_s), \quad d_\lambda^- = -\omega(A_s). \tag{3.48}$$

3.2.2 Set of effective transformation strains

For an isotropic polycrystal of a shape-memory alloy, the set of effective transformation strains is defined by two parameters a and b. In Figures 3.2 and 3.3 the effect of changes of these two parameters on the shape and size of the phase transformation locus. As illustrated in these figures parameter b is responsible for the size of the transformation locus and parameter a controls the shape of the set.

This suggests that in order to understand fully the size and shape of the transfor-

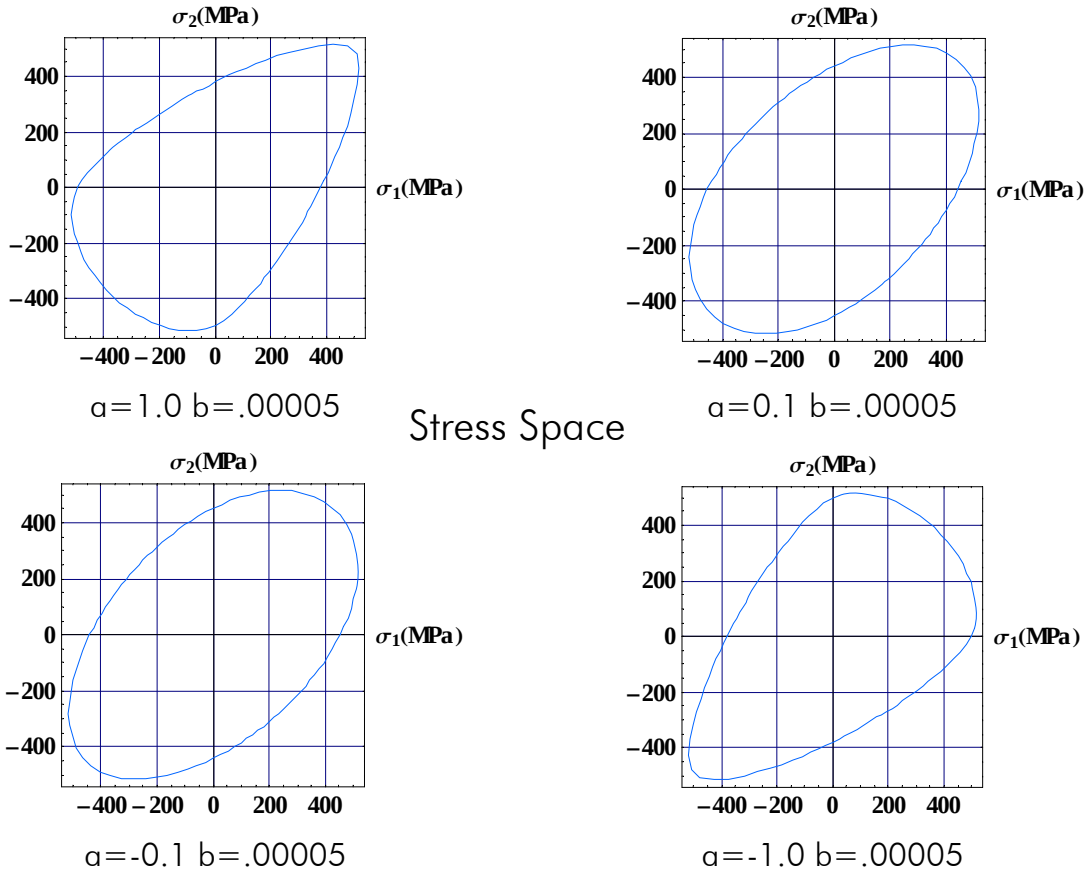

Figure 3.2: Parameter study on the effect of parameter a on the shape of the phase transformation surface.

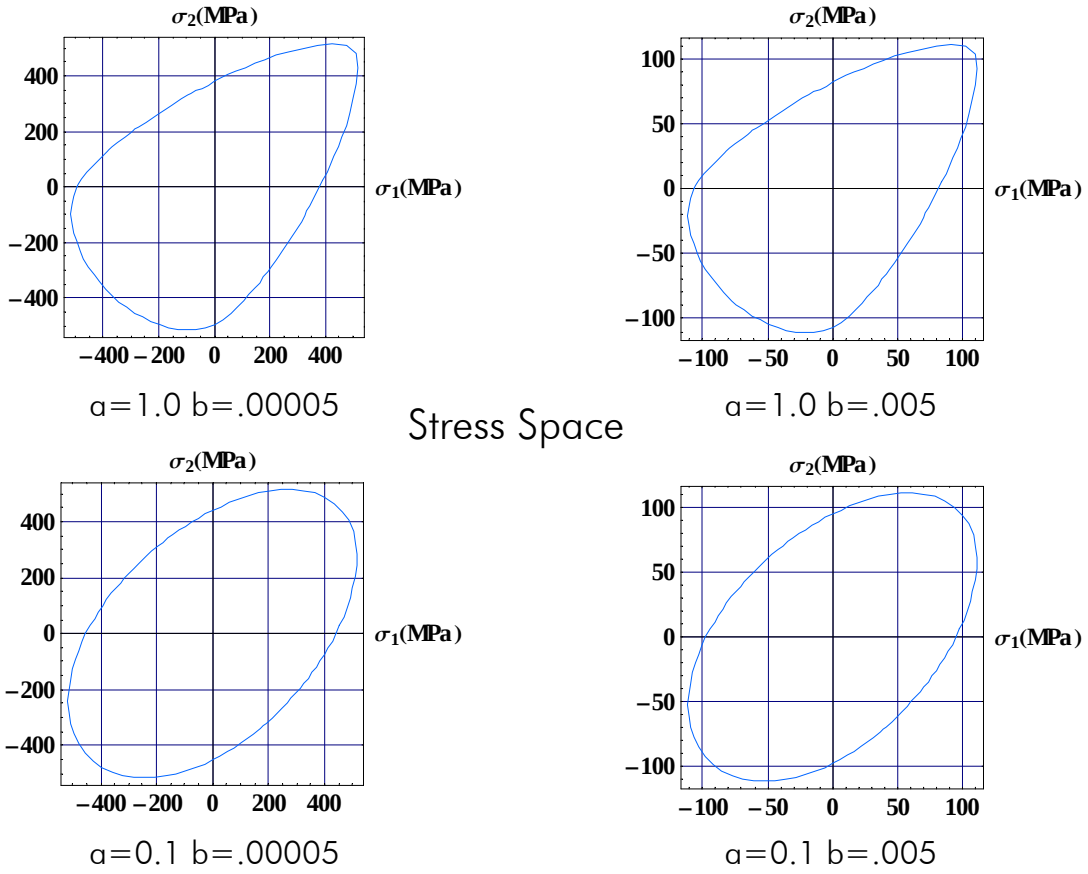

Figure 3.3: Parameter study on the effect of parameters a and b on the shape and size of the phase transformation surface.

mation surface we only need to evaluate parameters a and b and this only needs two data points at the onset of the transformation yield.

In the presence of such information, as described in section 3.1.6 we solve for two different stress directions say, $\sum_1$ and $\sum_2$, in order to find P, the set of effective transformation strains in the transformation strain ε_m space.

For a Ti - 49.75 Ni (at.%) with an austenite-twinned martensite interface we pick the critical stress values in $< 1\,0\,0 >$ and $< 1\,\bar{1}\,0 >$ directions and derive the set of effective transformation strains.

$$\begin{aligned}
\text{Direction} < 1\,0\,0 >: \quad (\sigma_1,\, \sigma_2) &= (380,\quad 0)(\text{MPa}) \quad \Rightarrow \quad s_{c1} = 380\ (\text{MPa}),\\
\text{Direction} < 1\,\bar{1}\,0 >: \quad (\sigma_1,\, \sigma_2) &= (0, -240)(\text{MPa}) \quad \Rightarrow \quad s_{c2} = 339\ (\text{MPa}).
\end{aligned}$$

Given the above two data points and $\varepsilon_m^t = 5\%$ we find unknown parameters a and b in the following steps:

1. Find a relation $b = F_1(a)$ between parameters a and b given

$$\max_{\varepsilon_m \in P} (\Sigma_1 : \varepsilon_m) \;=\; \varepsilon_m^t.$$

2. Use (3.46) to write

$$(d_\lambda^+ + \omega) \;=\; s_{c1} \max_{\varepsilon_m \in P} (\Sigma_1 : \varepsilon_m) \;=\; s_{c1}\, \varepsilon_m^t.$$

3. Find a relation $b = F_2(a)$ between parameters a and b given

$$\max_{\varepsilon_m \in P} (\Sigma_2 : \varepsilon_m) \;=\; \frac{(d_\lambda^+ + \omega)}{s_{c2}} \;=\; \varepsilon_m^t \frac{s_{c1}}{s_{c2}}.$$

4. Given $b = F_1(a)$ and $b = F_2(a)$ solve for a and b.

Using the above procedure the transformation surface in the transformation strain space is derived as shown in Figure 3.4. In this figure, values of parameters a and b are 1.035 and 0.000049, respectively. In this figure there is a stress direction vector

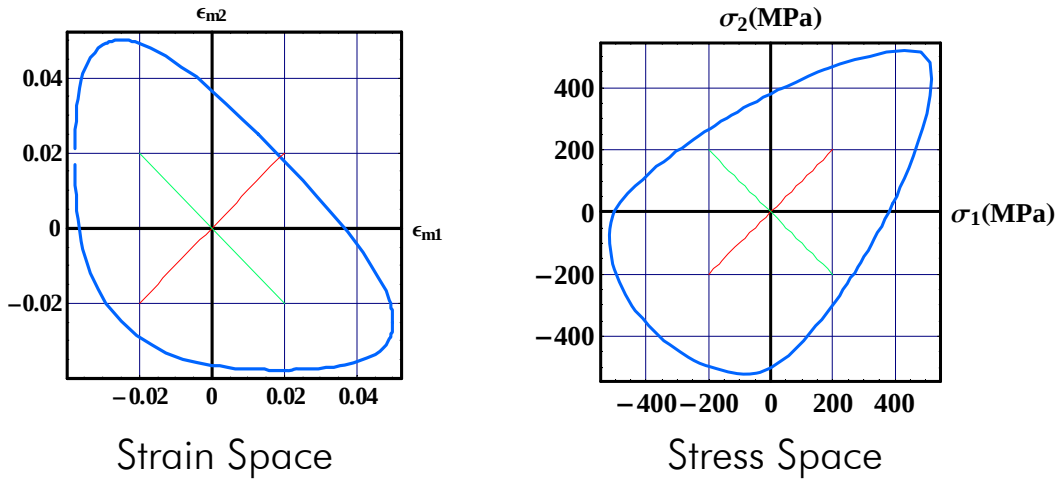

Figure 3.4: Phase transformation surfaces of Ni-Ti in stress and strain space.

Σ for every point on the transformation locus. The value of $(d_\lambda^+ + \omega)$ is also known from the above. Now using (3.46) the phase transformation surface in the principal stress space is derived as in Figure 3.4. This figure is consistent with the experimental phase transformation yield points obtained for proportional biaxial loadings in tension(compression)-torsion or bicompression (25),(37). By temperature variations, the phase transformation yield locus in the stress space would naturally change size. This is introduced by the temperature dependence of ω, according to (3.9). As temperature grows, the difference in stress-free chemical energy of the austenite and the martensite grows and this would lead to higher critical phase transformation stress values and a larger stress phase transformation yield locus accordingly. In this model it is assumed that the phase transformation yield locus in the ϵ_m space does not change by temperature and thus parameters a and b remain constant.

3.2.3 Proportional loading

For the same material parameters as listed earlier and for the phase transformation yield locus that we just derived, here we simulate a few different proportional loading experiments. Figure 3.5 shows results of our simulations of the uniaxial tension-compression tests for different initial temperatures θ. In these plots evolution of the

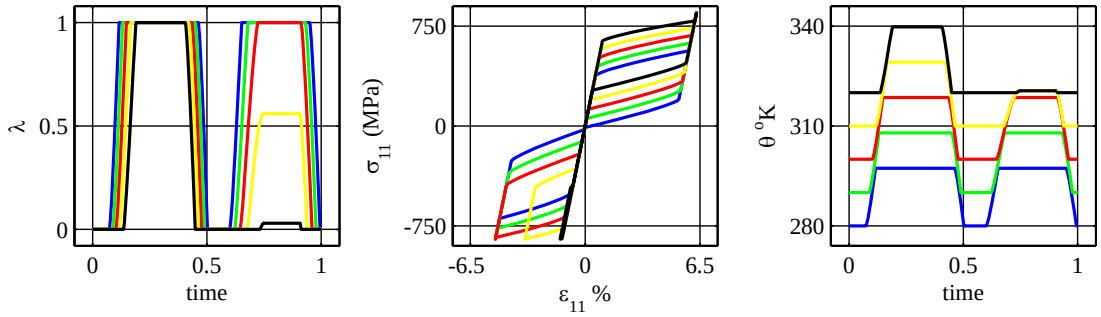

Figure 3.5: Uniaxial tension-compression stress-strain curves under proportional loading.

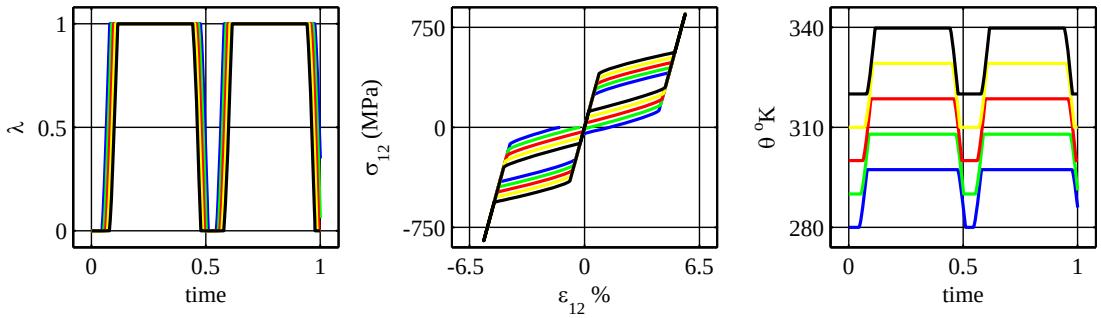

Figure 3.6: Pure shear stress-strain curves under proportional loading.

volume fraction of martensite and the temperature changes in the sample are also demonstrated. It should be noted that in these plots λ and θ have been tracked for a *full* tension-compression test. Rate of loading and unloading under tension and compression being kept fixed implies that to study the growth of martensite under tension, one should follow λ plots from time $t = 0.0$ to $t = 0.5$ and to study the growth of martensite under compression, one should follow λ plots from time $t = 0.5$ to $t = 1.0$. The same is valid about the temperature evolution under tension and compression. Figure 3.6 shows the stress-strain response, growth of volume fraction of martensite and temperature as a function of time for pure shear tests for different initial temperatures θ.

Figure 3.7 shows results of application of the current model for a set of biaxial tension-compression tests. In these simulations the initial temperature θ is assumed to be equal to 280°K and adiabatic condition is considered, the biaxial stress tensor

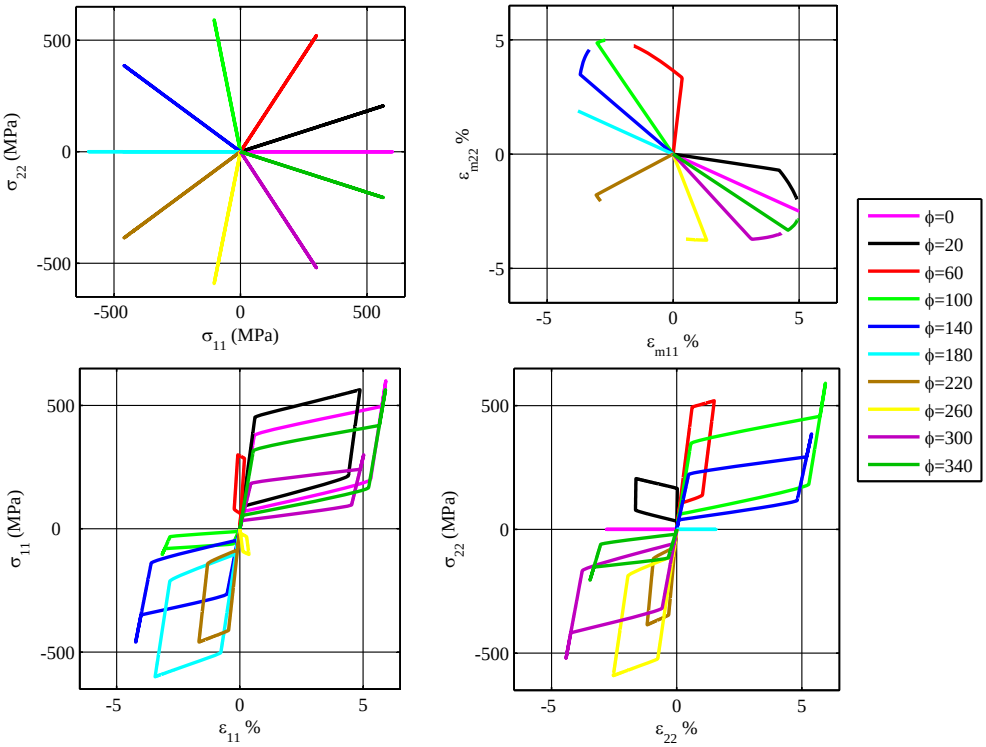

Figure 3.7: Biaxial proportional tension-compression loading of Ni-Ti.

is assumed to be as follows:

$$\sigma = \sigma_{max}(t) \begin{pmatrix} \cos\phi & 0 & 0 \\ 0 & \sin\phi & 0 \\ 0 & 0 & 0 \end{pmatrix}. \tag{3.49}$$

3.2.4 Non-adiabatic conditions

To illustrate the stress-strain behavior under non-adiabatic thermal conditions we assume the following relation for the radiative heating r:

$$r = -\frac{4h}{d_s}(\theta - \theta^*).$$

where h is the convection heat transfer coefficient and for the air it is normally 10 to 100 $\frac{\mathrm{J}}{\mathrm{m^2\,K\,s}}$. Parameter d_s is the diameter of the specimen for a cylinder sample and

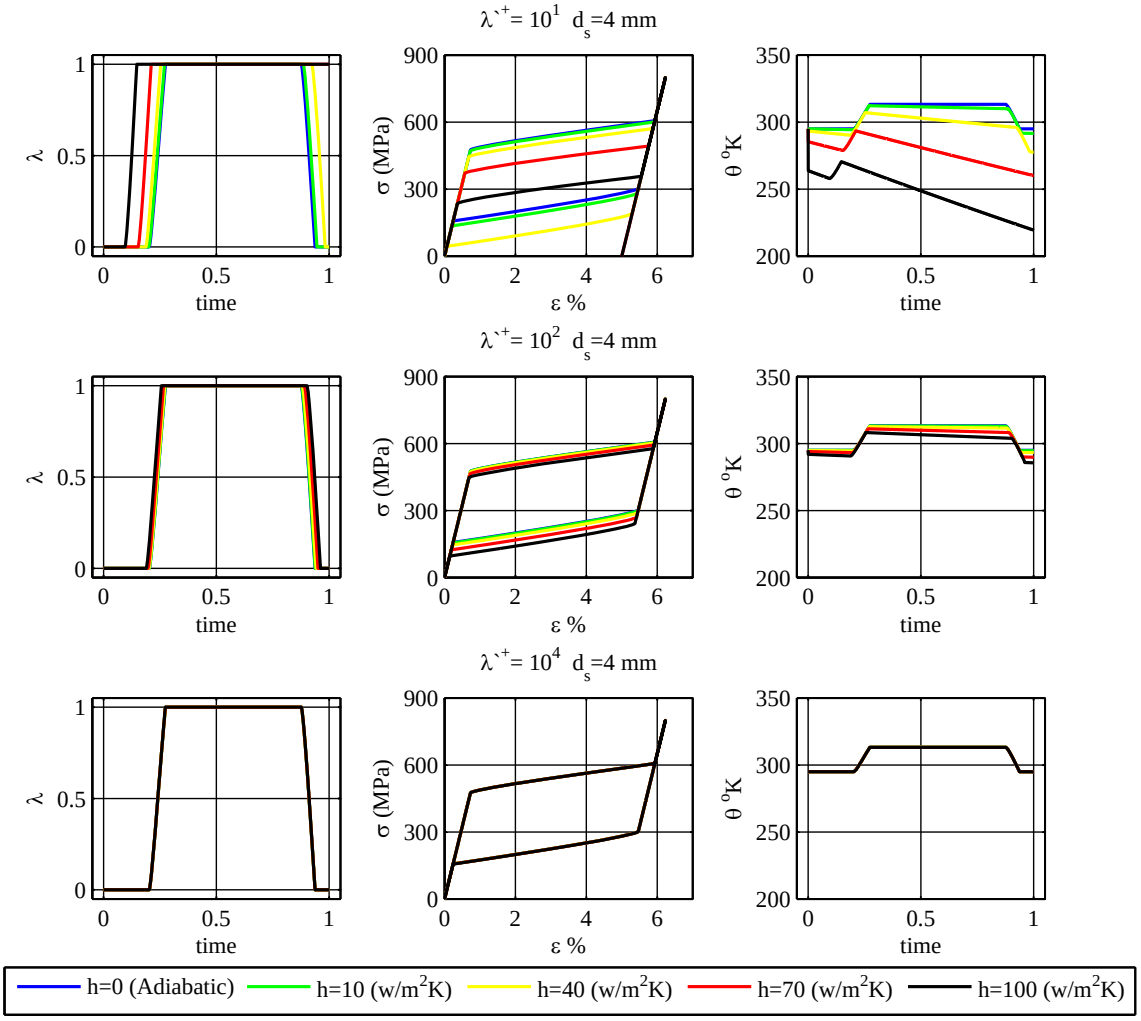

Figure 3.8: Non-adiabatic conditions.

θ^* is the ambient temperature.

This changes (3.38) to

$$c_p\dot{\theta} \;=\; \theta\dot{\lambda}\frac{\mathcal{L}}{\theta_{cr}} + r \Rightarrow c_p\dot{\theta} \;=\; \theta\dot{\lambda}\frac{\mathcal{L}}{\theta_{cr}} - \frac{4h}{d_s}\left(\theta - \theta^*\right).$$

Integrating the above, we obtain a relation between temperature, volume fraction of martensite, latent heat, specific heat and convection heat transfer coefficient.

$$\theta(t) \;=\; \exp^{\int_0^t (\frac{\mathcal{L}}{c_p\,\theta_{cr}}\,\dot{\lambda}(\tau) - \frac{4h}{c_p\,d_s})d\tau}\left(\theta_0 \;-\; \int_0^t \frac{4h}{c_p\,d_s}\,\exp^{-\int_0^\tau (\frac{\mathcal{L}}{c_p\,\theta_{cr}}\,\dot{\lambda}(\tau^*) - \frac{4h}{c_p\,d_s})d\tau^*}\,d\tau\right).$$

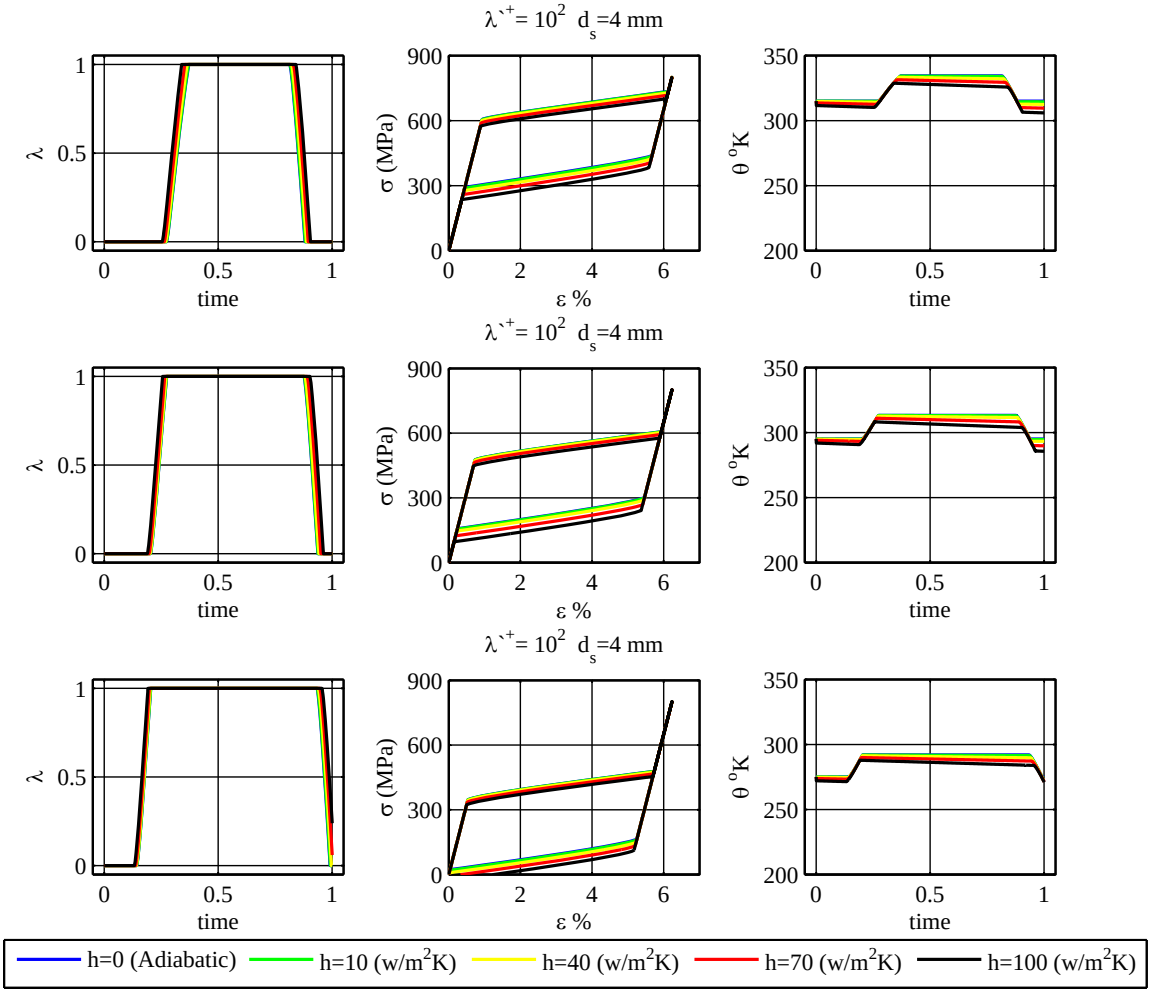

Figure 3.9: Non-adiabatic conditions.

Figure 3.8 shows the stress-strain hysteresis for a cylindrical NiTi specimen of diameter $d_s = 4$ mm and at ambient room temperature. In this figure the effect of changes in the value of the convection heat transfer coefficient on the stress-strain response of the material is demonstrated. The temperature profile as well as the profile of the volume fraction of martensite are also demonstrated in this figure. As illustrated in the figure the phase transformation and the heat convection are two competing processes and for higher rates of phase transformation processes, the heat convection effect is decreased. This is predictable from 3.42 as for larger $\dot{\lambda}^+$'s the term $\frac{4h}{c_p\, d_s}$ would be negligible compared to $\frac{\mathcal{L}}{c_p\, \theta_{cr}}\, \dot{\lambda}$.

In Figure 3.9 we study the effect of the ambient temperature on the heat convection. We pick a given maximum rate for the kinetic relation equal to $\dot{\lambda}^+ = 10^2 s^{-1}$ and in each row start the simulations with a given ambient temperature $\theta^* = 275^o$K, $\theta^* = 295^o$K and $\theta^* = 315^o$K, respectively.

3.2.5 Nonproportional loading

In this section, numerical simulation of nonproportional loading of a NiTi SMA is presented. The simplified model proposed above is used to simulate the mechanical behavior of the specimen. Transformation temperatures, latent heat and other material parameters are chosen as listed previously; thermal condition is assumed to be adiabatic however.

Figure 3.10 shows stress-controlled simulations of a tension-torsion test. This is a stress-controlled test and the corresponding strain path is measured. On the path demonstrated by blue lines, tension is applied first. After reaching a tensile stress of 800 (MPa) tensile loading is halted and torsion starts. For a fixed tensile stress, torsion continues to grow till we reach the same level stress for torsion as that of tension. Then torsion is unloaded till zero torsion stress is achieved. At this time tensile force is also decreased for a final stress-free state. The same pattern is repeated for a torsion first, tension next loading case. This figure shows detailed information regarding the growth of λ, stress and strain. For a strain-controlled test a similar simulation can be conducted.

Figures 3.11, 3.12 and 3.13 show stress-controlled tension-torsion simulations of the same NiTi sample on six additional stress paths. In these plots one could follow the evolution of the internal variables λ and ε_m as well as the corresponding stress and strain paths. It should be noted that the ε_{m11}-ε_{m12} plot in Figures 3.13 is a cross-section of the phase transformation surface in the ε_{m11}-ε_{m12} plane.

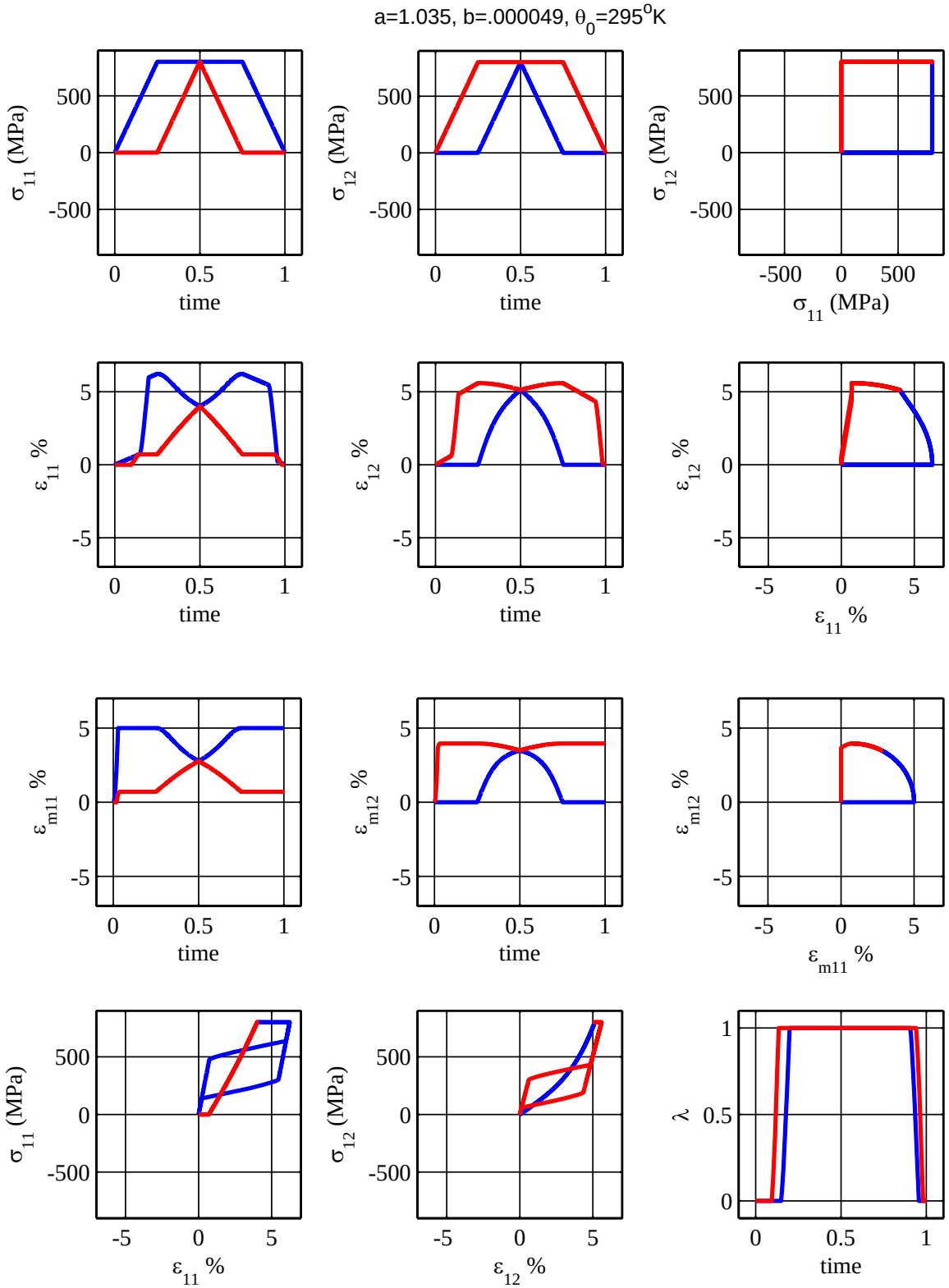

Figure 3.10: Nonproportional stress-controlled test.

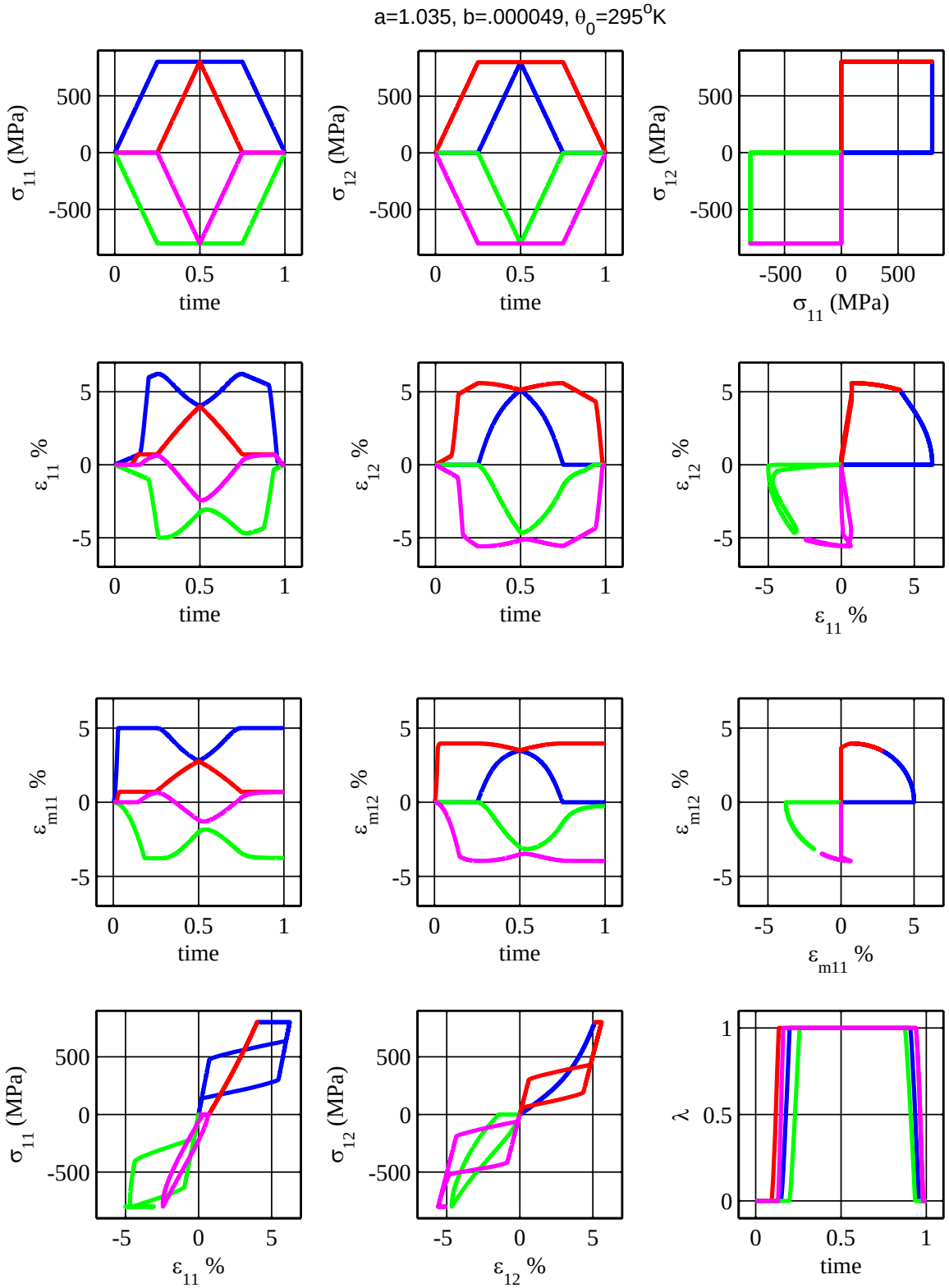

Figure 3.11: Nonproportional stress-controlled test.

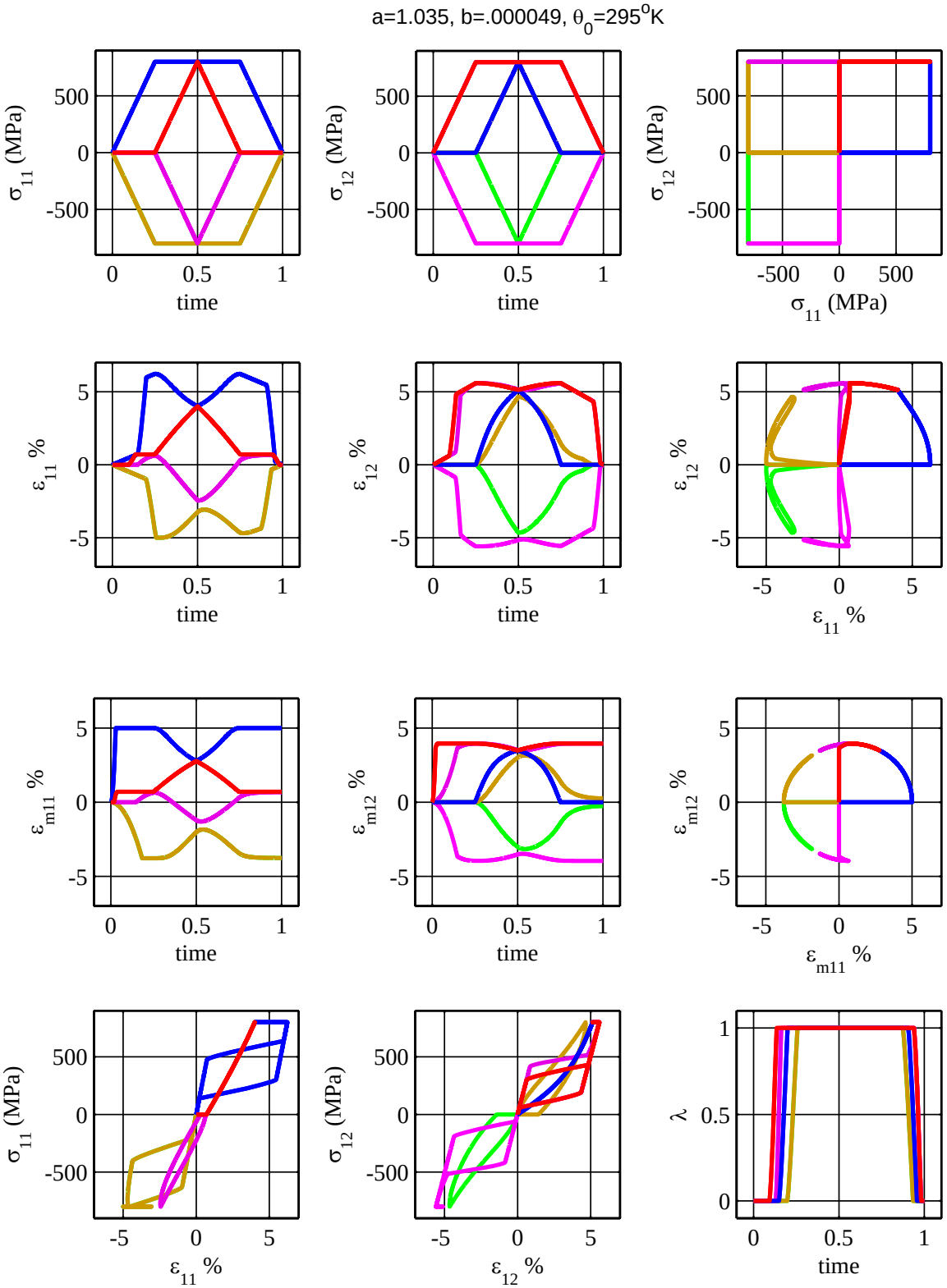

Figure 3.12: Nonproportional stress-controlled test.

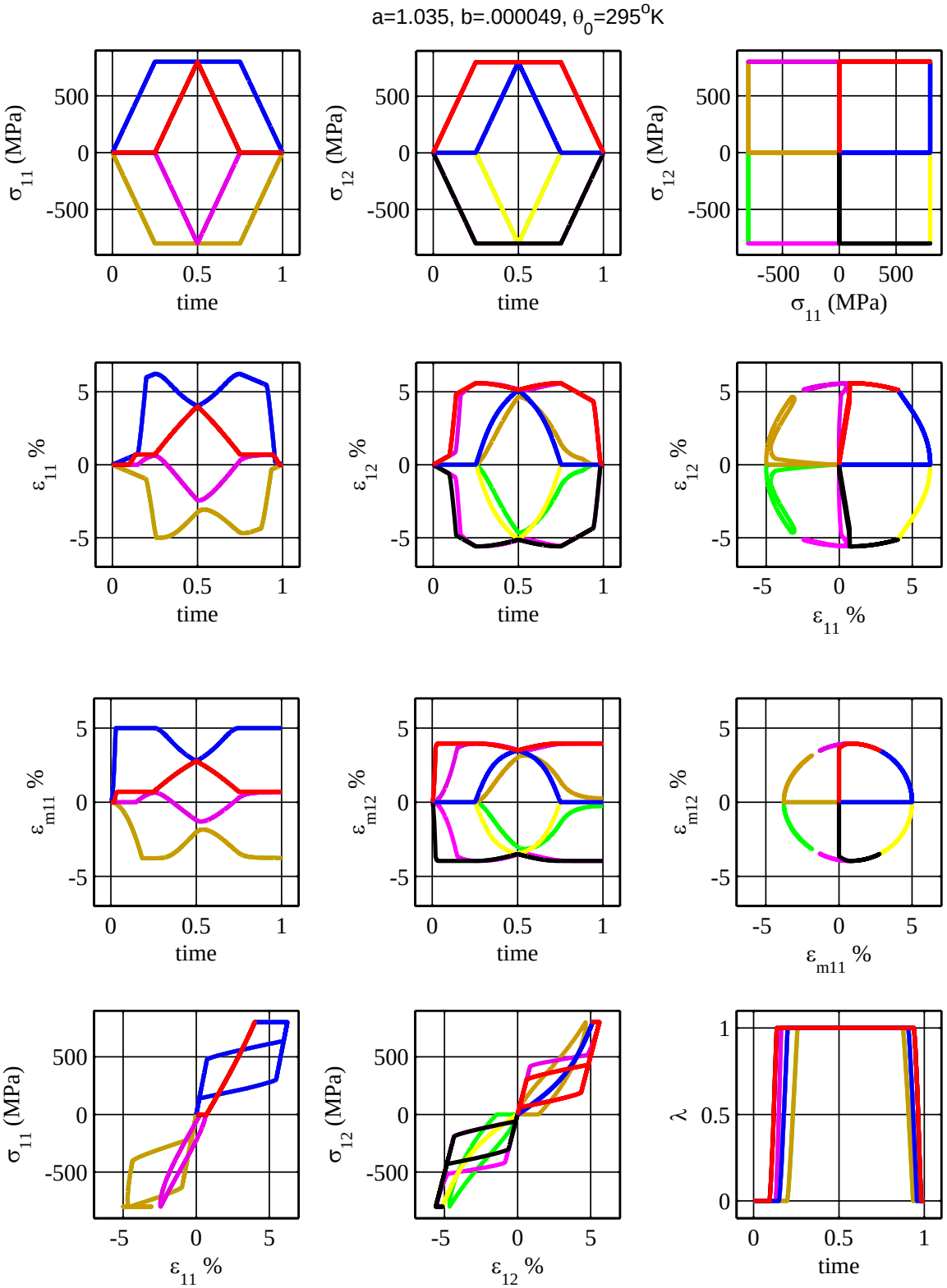

Figure 3.13: Nonproportional stress-controlled test.

3.3 Demonstration of the anisotropic model

To address micromechanical features such as texture, we need to understand the microstructure of the material and its relation to macroscopic properties in both single and polycrystals. In some circumstances such as for alloys that have been reduced in thickness by cold rolling in one direction, the introduction of a degree of anisotropy to the theory is necessary. In fact there is much experimental evidence on the effect of texture on properties of shape-memory alloys that, not considering the anisotropy in a thermomechanical constitutive model, would definitely limit its applications. In this section we demonstrate applicability of this model in modelling the anisotropy in shape-memory alloys. After parameterizing the phase transformation surface for an anisotropic alloy and further stress-controlled and strain-controlled simulations for a given SMA, we review Shu and Bhattacharya's (47) earlier work to model the effect of texture as a crucial factor in determining the shape-memory effect in polycrystals. We then show that our model is able to predict the qualitative behavior of a polycrystal alloy and its dependence on texture.

3.3.1 Parameters

Consistent with the assumptions of the previous section we choose to work with typical material parameter values of NiTi and consider the following parameters:

$$\begin{aligned} M_s &= -51.55\,^oC \quad \text{and} \quad A_s = -6.36\,^oC \\ \mathcal{L} &= 79\ (\frac{\text{MJ}}{\text{m}^3}) \quad \text{and} \quad c_p = 5.4\ (\frac{\text{MJ}}{\text{m}^3\,^o\text{K}}) \\ E &= 65\ (\text{GPa}) \quad \text{and} \quad \sigma_y = 1500\ (\text{MPa}) \end{aligned} \tag{3.50}$$

3.3.2 Set of effective transformation strains

As proposed earlier in (3.34) the set of recoverable strains for an anisotropic shape-memory alloy has three different parameters: a, b and c. In this section we intend to parameterize the phase transformation surface. It is good to note that parameter b

is a size parameter, i.e., it does not change the shape of the surface and that is why in the forthcoming sections we would fix b's value to that of the isotropic case, i.e., 0.000049 and only the interplay of changing parameters a and c is demonstrated.

3.3.3 Parameter study

Phase transformation strain tensor being trace-free has five independent components and this would complicate a parameter study of the phase transformation surface if not simplified further. Here at the first step we consider two different special cases, one without any shear strain and one with shear. We study the effect of parameters a and c and keep parameter b fixed. For now we will also fix vector e to $< 1\,0\,0 >$.

First we study the no-shear case, where phase transformation strain tensor is assumed to be

$$\epsilon_m = \begin{pmatrix} \epsilon_{m11} & 0 & 0 \\ 0 & \epsilon_{m22} & 0 \\ 0 & 0 & -\epsilon_{m11} - \epsilon_{m22} \end{pmatrix}. \tag{3.51}$$

Figure 3.14 shows the phase transformation surface in ϵ_{m11} versus ϵ_{m22} surface. For three different values of a, parameter c is perturbed and the transformation locus is plotted. Perturbing a while c is fixed results in Figure 3.15.

To consider cases where shear component is non-trivial, we also consider a phase transformation strain tensor in the following form:

$$\epsilon_m = \begin{pmatrix} \epsilon_{m11} & \epsilon_{m12} & 0 \\ \epsilon_{m12} & 0 & 0 \\ 0 & 0 & -\epsilon_{m11} \end{pmatrix}. \tag{3.52}$$

Figure 3.16 shows the phase transformation surface in ϵ_{m11} versus ϵ_{m12} surface. Here again for three different values of a, parameter c is perturbed and the transformation locus is plotted. Perturbing a while c is fixed results in Figure 3.17. In all these plots, the curves with a zero parameter c demonstrate the projection of the phase transfor-

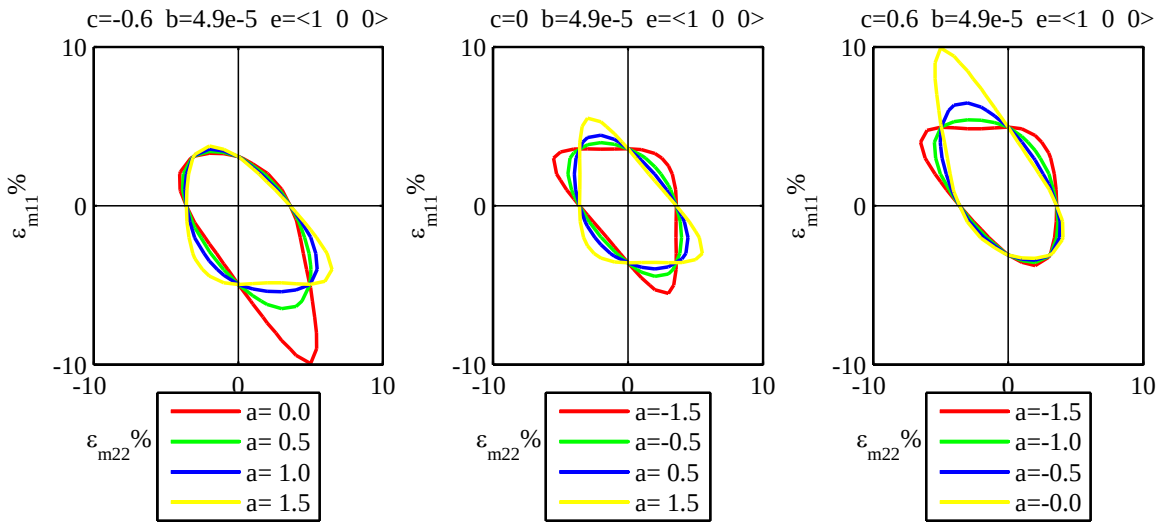

Figure 3.14: The effect of parameter c on the shape of the transformation surface.

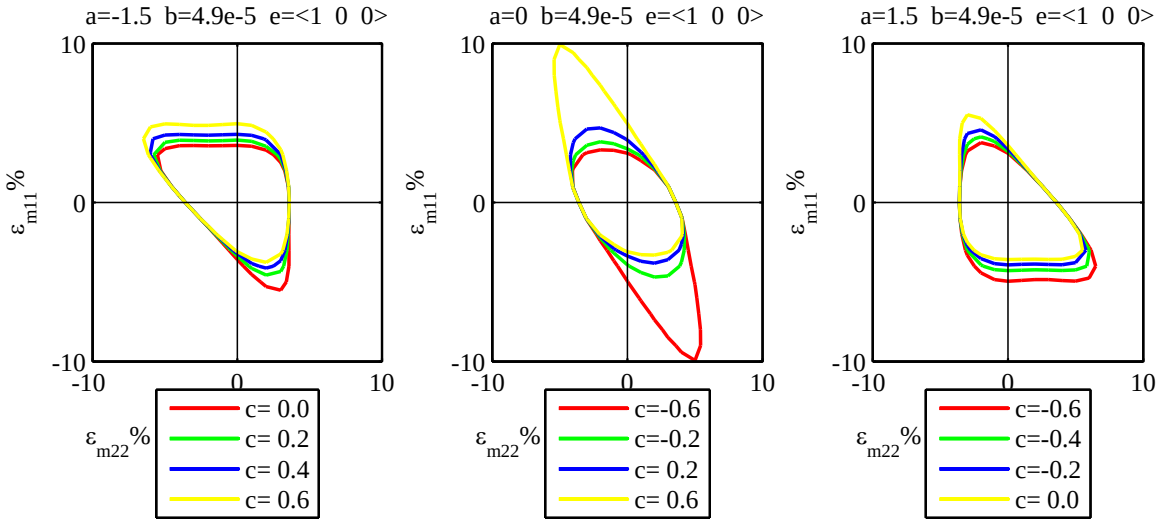

Figure 3.15: The effect of parameter a on the shape of the transformation surface.

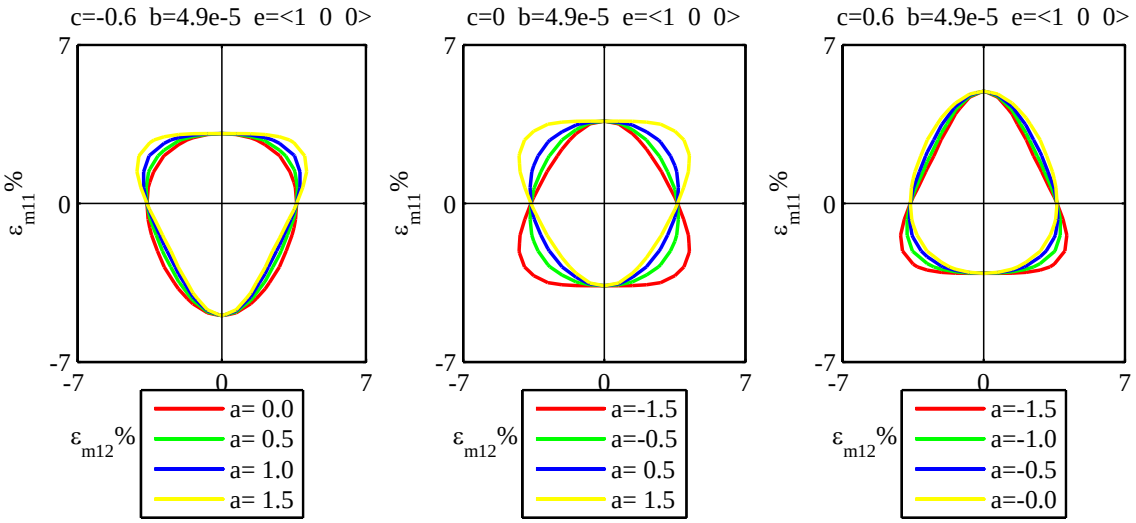

Figure 3.16: The effect of parameter c on the shape of the transformation surface.

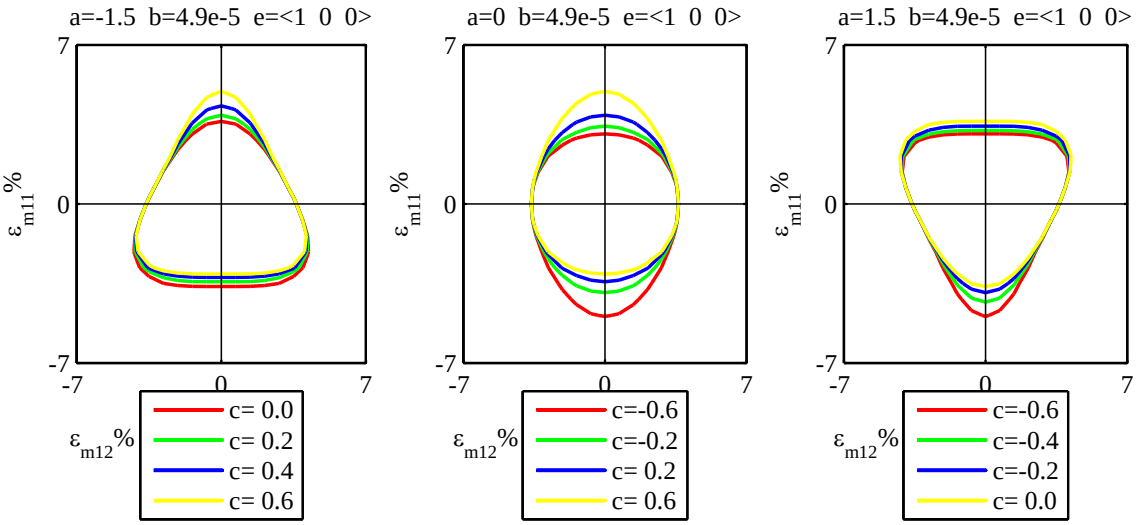

Figure 3.17: The effect of parameter a on the shape of the transformation surface.

mation yield surface for an *isotropic* NiTi ploycrystalline. These plots correctly show that the phase transformation surface is symmetric around the $\varepsilon_{m12} = 0\%$ line in the ε_{m11}-ε_{m12} strain plane.

The analytical model of Shu and Bhattacharya (1998) (47) suggests that for their combined tension $\pm$ torsion calculations of NiTi, the recoverable twist decreases with increasing imposed recoverable extension in random texture and $< 110 >$ texture while $< 100 >$ texture shows the opposite behavior. To simulate their model qualitatively, we choose the following two sets as values of the phase transformation surface parameters:

- Profile I : $a = 1.5$, $b = 0.000049$ and $c = -0.6$
- Profile II: $a = -1.5$, $b = 0.000049$ and $c = 0.6$

3.3.4 Stress-controlled tests

In the following simulations we closely study the evolution of the internal variables as well as stress-strain response of a ploycrystalline NiTi material. We continue to work with the preceding section's profile I and profile II. Fixing vector e to $< 1\,0\,0 >$ and using the same material parameters as listed in earlier sections, the evolution of internal variables λ and ϵ_m as well as the stress-strain behavior is derived as in Figure 3.18. Loading is tension/compression followed by torsion and the loading pattern is shown in the bottom right of Figure 3.18. The initial temperature is assumed to be $\theta_0 = 295^o$K, which is higher than the austenite finish temperature A_f of NiTi, thus the material undergoes superelastic deformation under tension plus torsion loads.

In this simulation σ_{11} and σ_{12} are the only non-trivial components of the stress tensor. Figure 3.18 in fact combines results of four different simulations together. These simulations are differentiated from each other by the sign of axial and shear stress. In all of them we start by stress loading the material axially up to a maximum load. Then shear stress starts increasing from zero while axial stress is kept constant, shear stress is then released at constant axial stress and finally material is unloaded

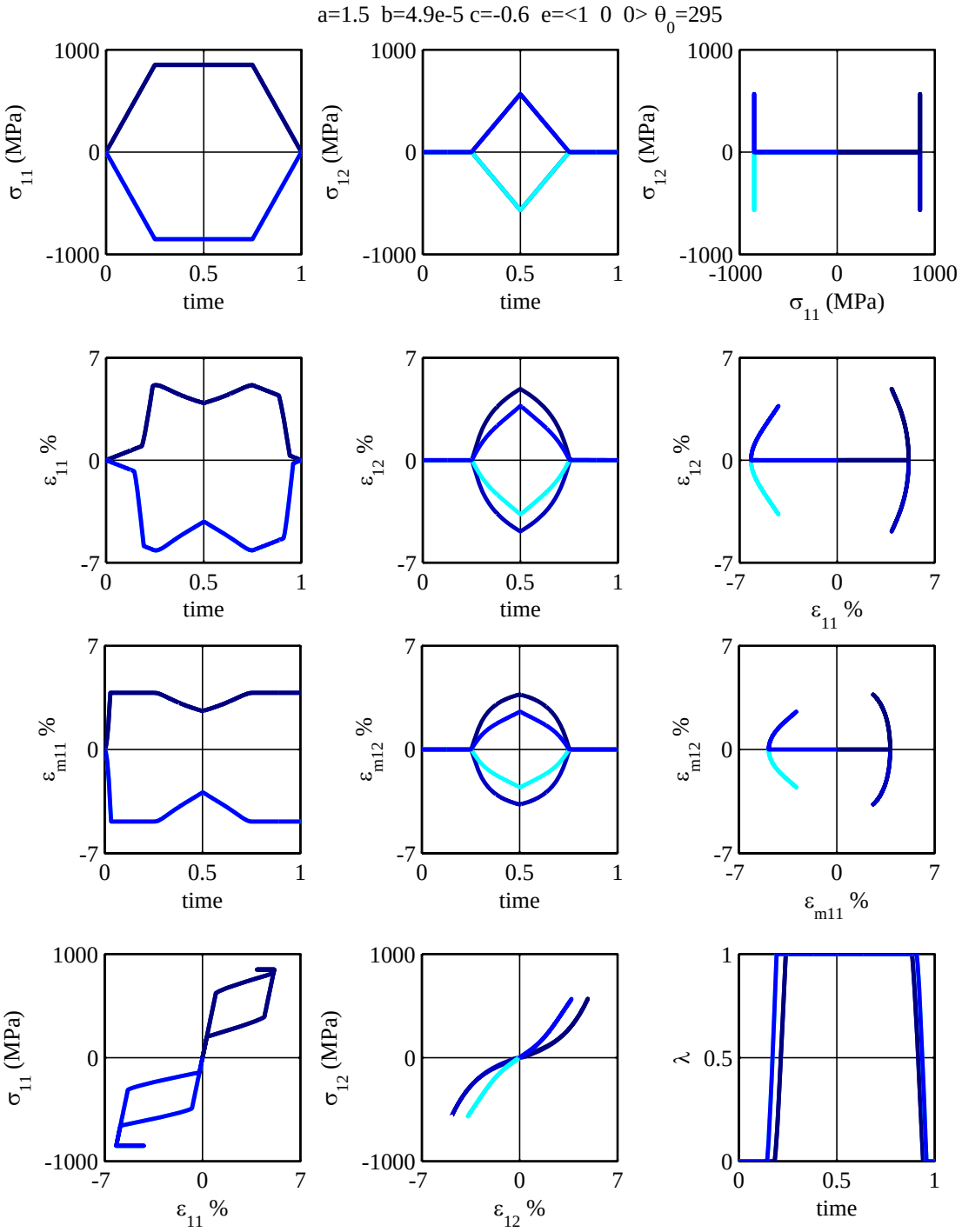

Figure 3.18: Stress-controlled behavior of an anisotropic NiTi polycrystalline: profile I.

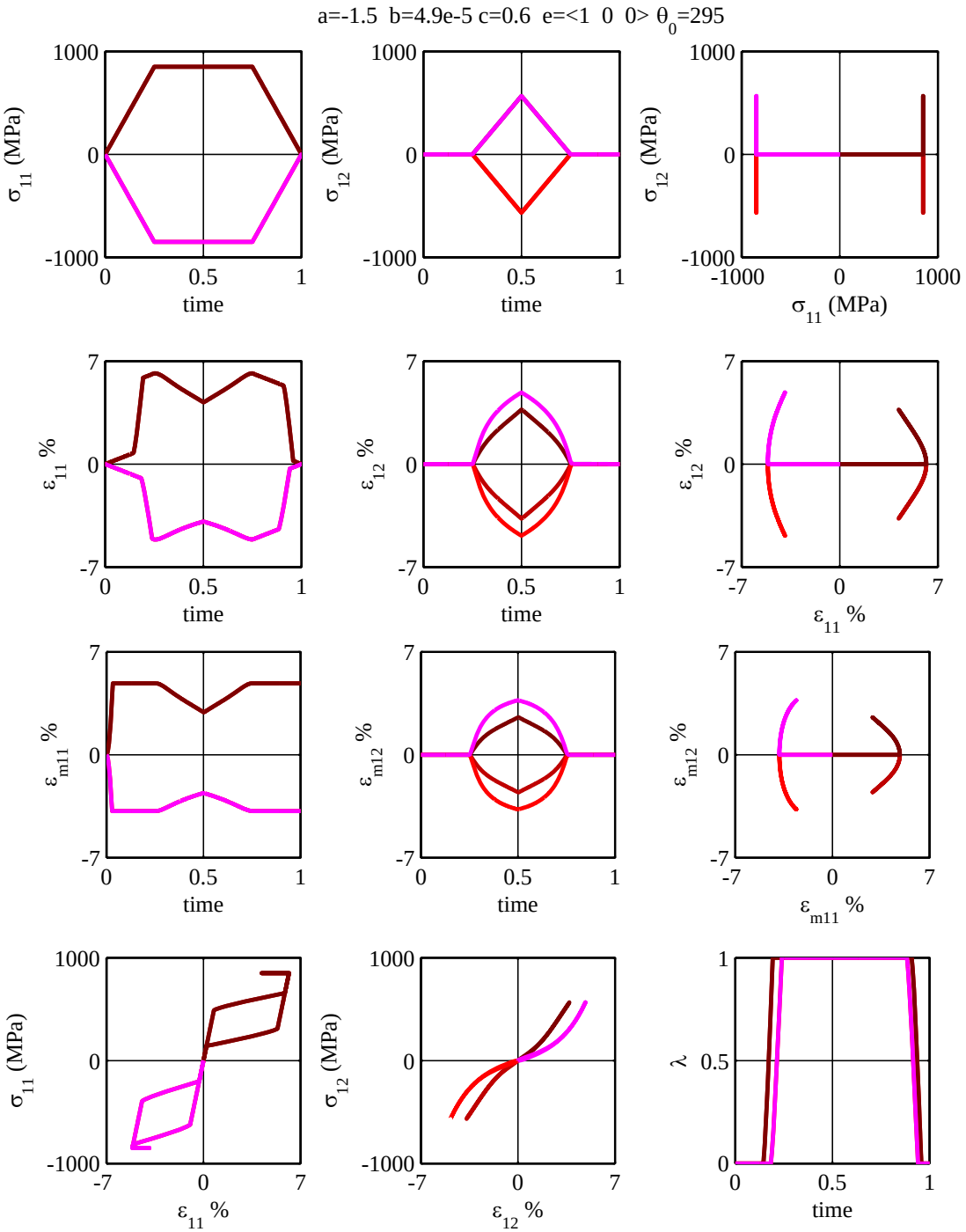

Figure 3.19: Stress-controlled behavior of an anisotropic NiTi polycrystalline: profile II.

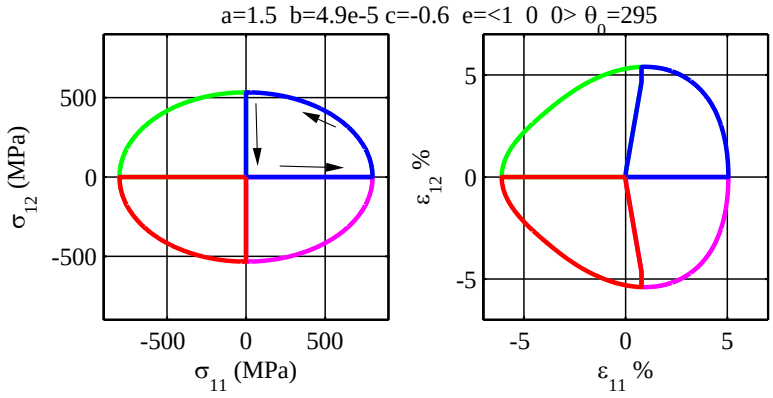

Figure 3.20: Stress-controlled tension-torsion simulation and the corresponding strain path of an anisotropic NiTi polycrystalline: profile I - Path 1.

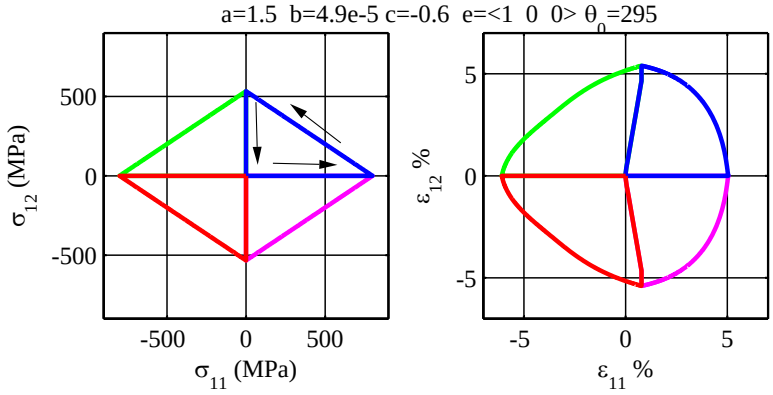

Figure 3.21: Stress-controlled tension-torsion simulation and the corresponding strain path of an anisotropic NiTi polycrystalline: profile I - Path 2.

axially to zero stress. The first two boxes on top left of this figure show this stress pattern; the next two boxes at the top are the axial and shear strain paths. Evolution of volume fraction of martensite and transformation strain is also shown in the middle. Figure 3.19 shows the same results derived for profile II.

Inspired by Sittner et al. (48) here we demonstrate six different types of tension-torsion stress-controlled simulations for an anisotropic NiTi polycrystal. We use profile I's transformation surface parameters. We use stress as the control parameter and the corresponding strain path is measured. Figures 3.20 through 3.26 show these results.

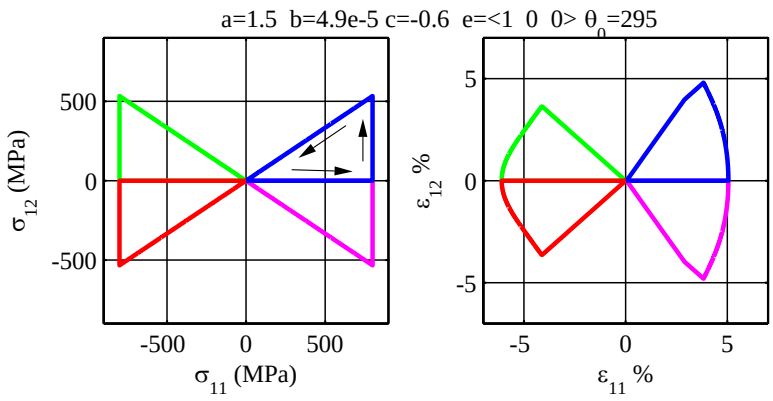

Figure 3.22: Stress-controlled tension-torsion simulation and the corresponding strain path of an anisotropic NiTi polycrystalline: profile I - Path 3.

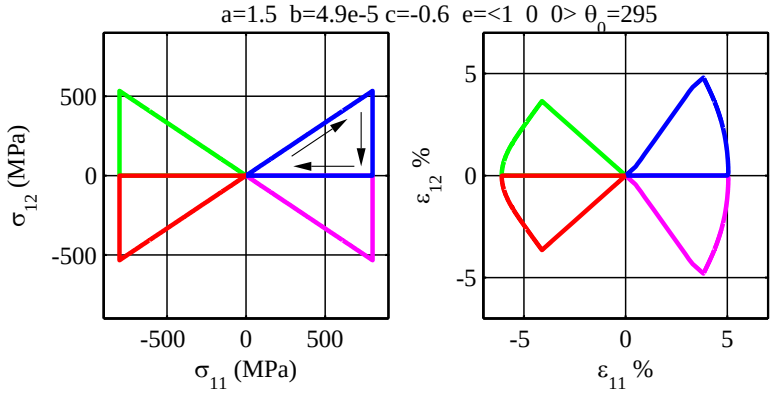

Figure 3.23: Stress-controlled tension-torsion simulation and the corresponding strain path of an anisotropic NiTi polycrystalline: profile I - Path 4.

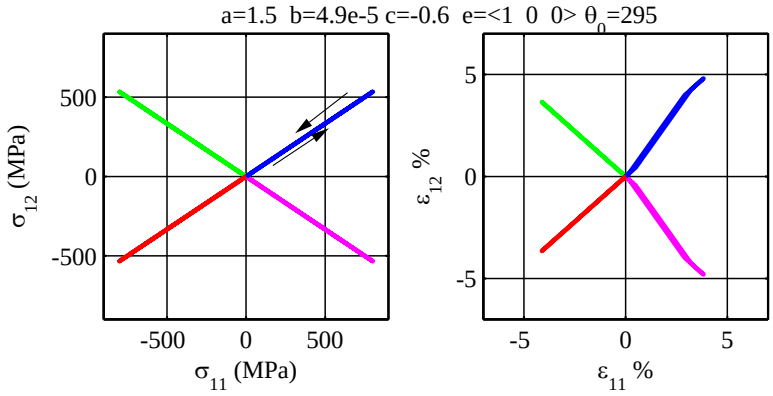

Figure 3.24: Stress-controlled tension-torsion simulation and the corresponding strain path of an anisotropic NiTi polycrystalline: profile I - Path 5.

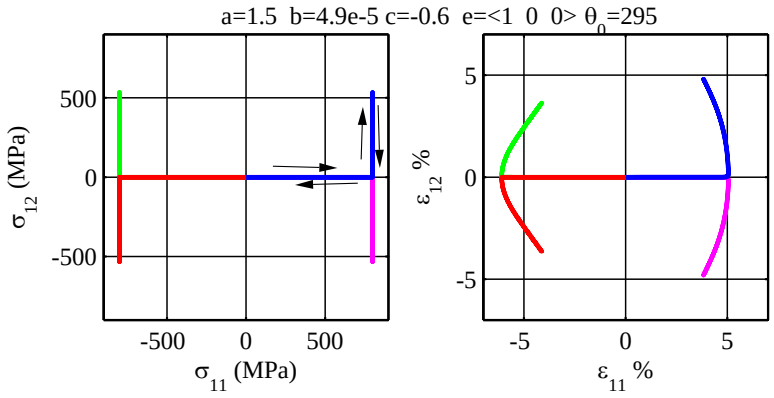

Figure 3.25: Stress-controlled tension-torsion simulation and the corresponding strain path of an anisotropic NiTi polycrystalline: profile I - Path 6.

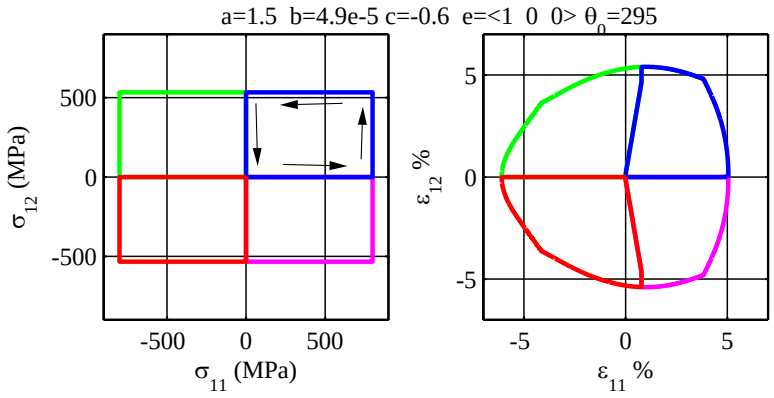

Figure 3.26: Stress-controlled tension-torsion simulation and the corresponding strain path of an anisotropic NiTi polycrystalline: profile I - Path 7.

3.3.5 Strain-controlled tests

In this section we present simulation results of a strain-controlled experiment. Material parameters are unchanged and Figure 3.27 and Figure 3.28 show these simulations for profile I and profile II, respectively.

In these simulations ϵ_{11} and ϵ_{12} are prescribed, ϵ_{22} is set to zero and other components of the strain tensor are derived by assuming the following form for the stress tensor:

$$\sigma = \begin{pmatrix} \sigma_1 & \tau & 0 \\ \tau & \sigma_2 & 0 \\ 0 & 0 & 0 \end{pmatrix}. \tag{3.53}$$

Here values of σ_1, σ_2 and τ are derived for each iteration based on the current values of ϵ_{11} and ϵ_{12}. Like the two preceding figures, these figures combine results of four simulations, where material is strain-loaded axially and then a shear strain is forced on the sample in the same fashion as that of the stress-controlled simulations of the previous section.

3.3.6 Effect of texture

In this section the effect of texture on a polycrystal of shape-memory alloy is demonstrated. Consider a thin sheet of the alloy under uniaxial tensile stress. We intend to rotate vector e in the plane and record the change in the recoverable strain as depicted in Figure 3.29.

Inoue et al. (23) have investigated planar anisotropy of shape-memory strain in polycrystalline NiTi alloy sheets and for a number of different textures have measured the recoverable tensile strain. Figure 3.30 shows how our model is capable of reproducing experimental observations of PL-CR sheets as reported in (23). The measured data are shown with a red line; the green line is simulation results for an isotropic material that does not show a texture effect as expected. The simulation results for anisotropic PL-CR sample sheets are shown with blue lines. One can use these re-

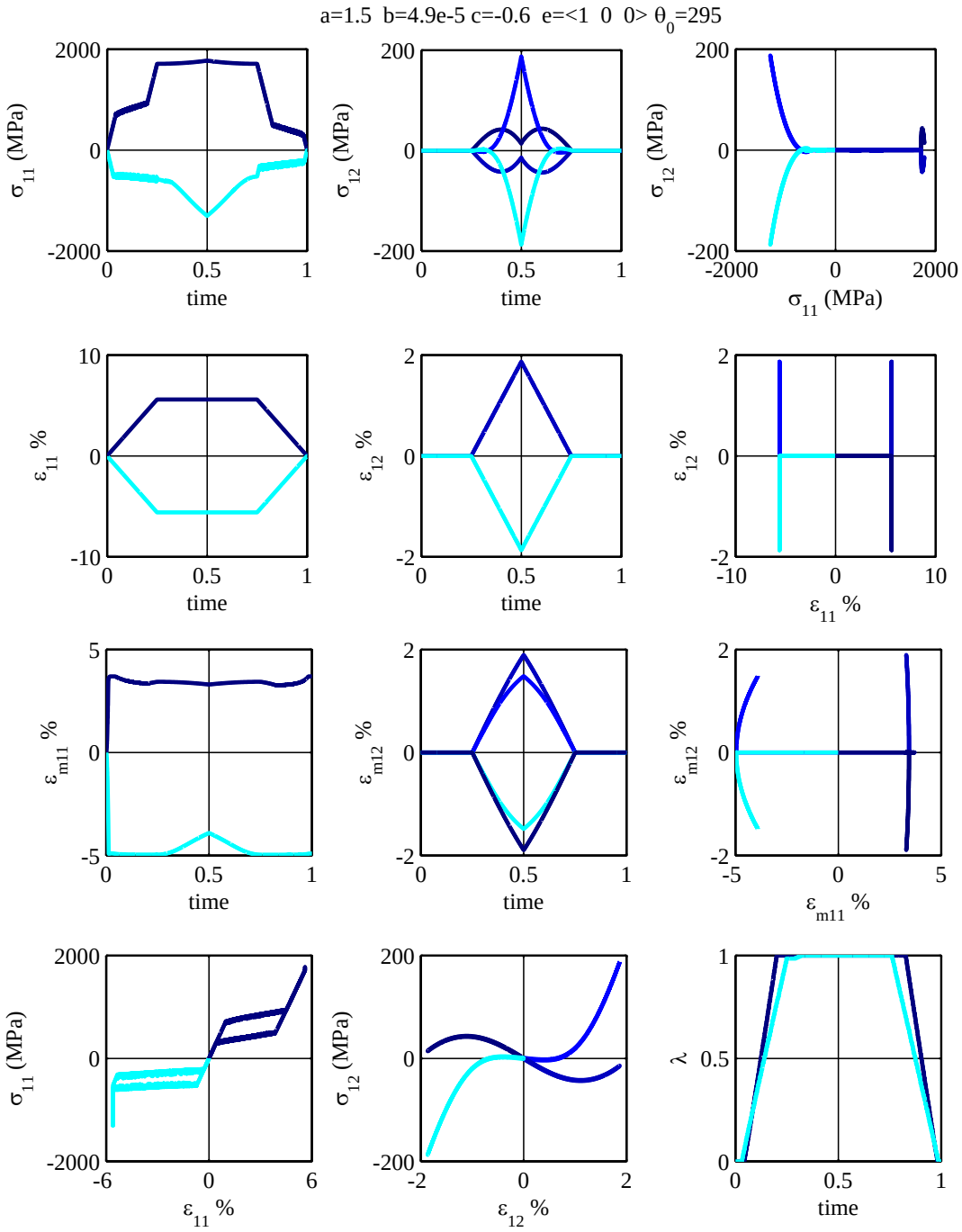

Figure 3.27: Strain-controlled behavior of an anisotropic NiTi polycrystalline: profile I.

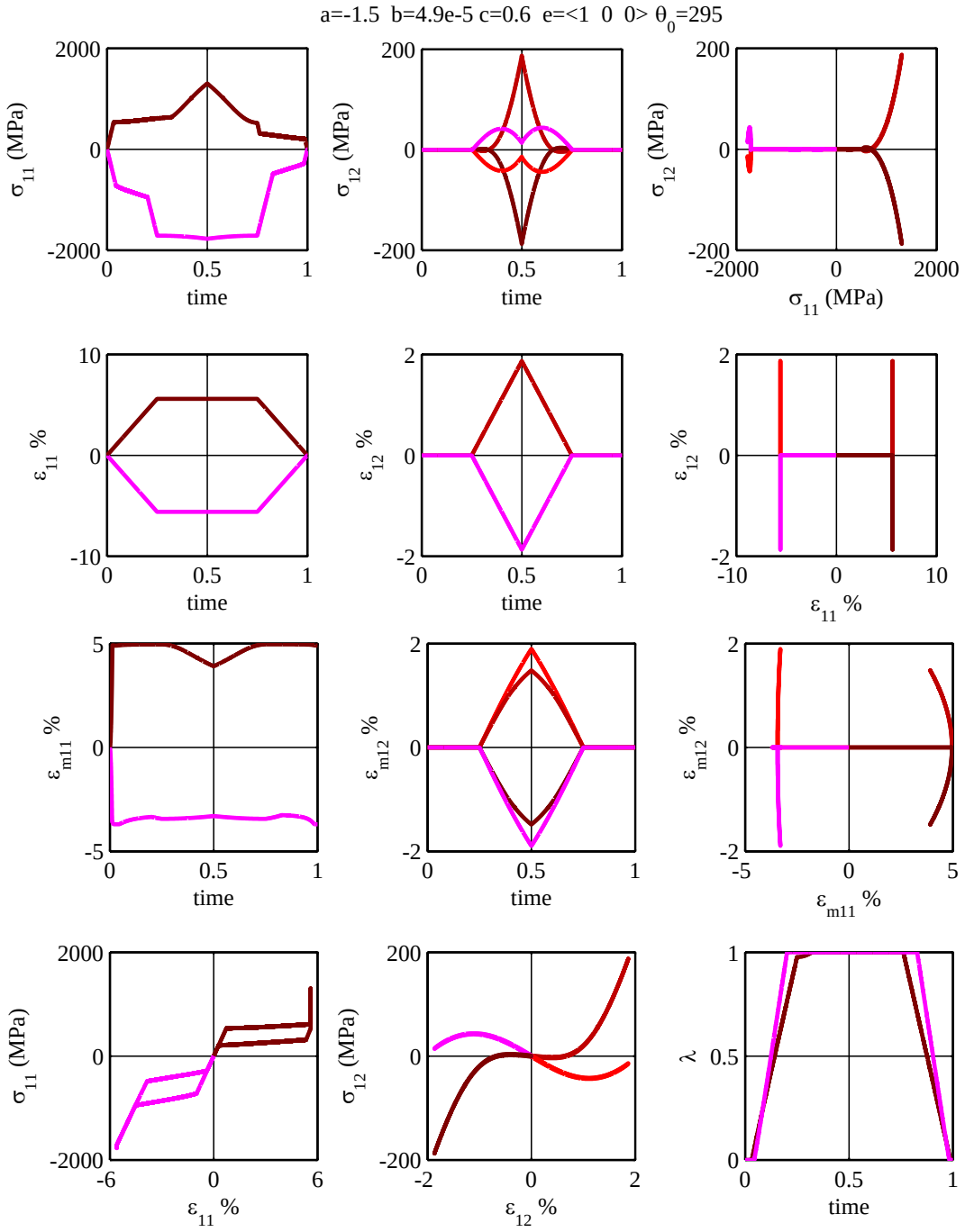

Figure 3.28: Strain-controlled behavior of an anisotropic NiTi polycrystalline: profile II.

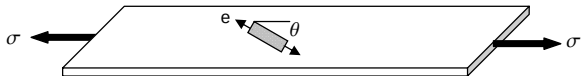

Figure 3.29: Rolled sheet under tensile stress

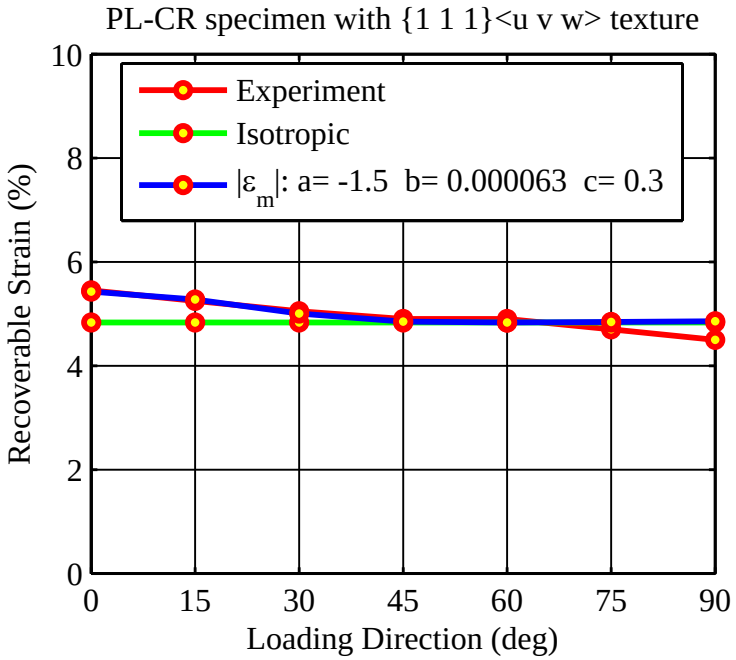

Figure 3.30: Analytical model v.s. experiment, PL-CR ($\{1\,1\,1\}< u\,v\,w >$ texture).

sults to parameterize the phase transformation yield surface and then to study the stress-strain response of the material for different textures.

Figure 3.31 demonstrate results of the stress-controlled simulations of polycrystalline NiTi samples with isotropic, $< 1\,1\,0 >$ and $< 1\,0\,0 >$ fiber textures, respectively. In all these simulations material parameters are equivalent to the ones listed in 3.3.1 and ambient temperature is equal to $\theta_0 = 295^o$K. These figures show the recoverable torsion vs. the recoverable extension in TiNi polycrystals with random texture as well as the two aforementioned textures. These results are qualitatively comparable to predictions of Shu and Bhattacharya (47).

Notice that in Figure 3.31 the recoverable twist decreases with increasing recoverable extension in $< 1\,1\,0 >$ fiber texture while $< 1\,0\,0 >$ texture does not follow the same path, for this texture twist initially increases by increasing extension and after it *saturates* it starts decreasing as extension grows.

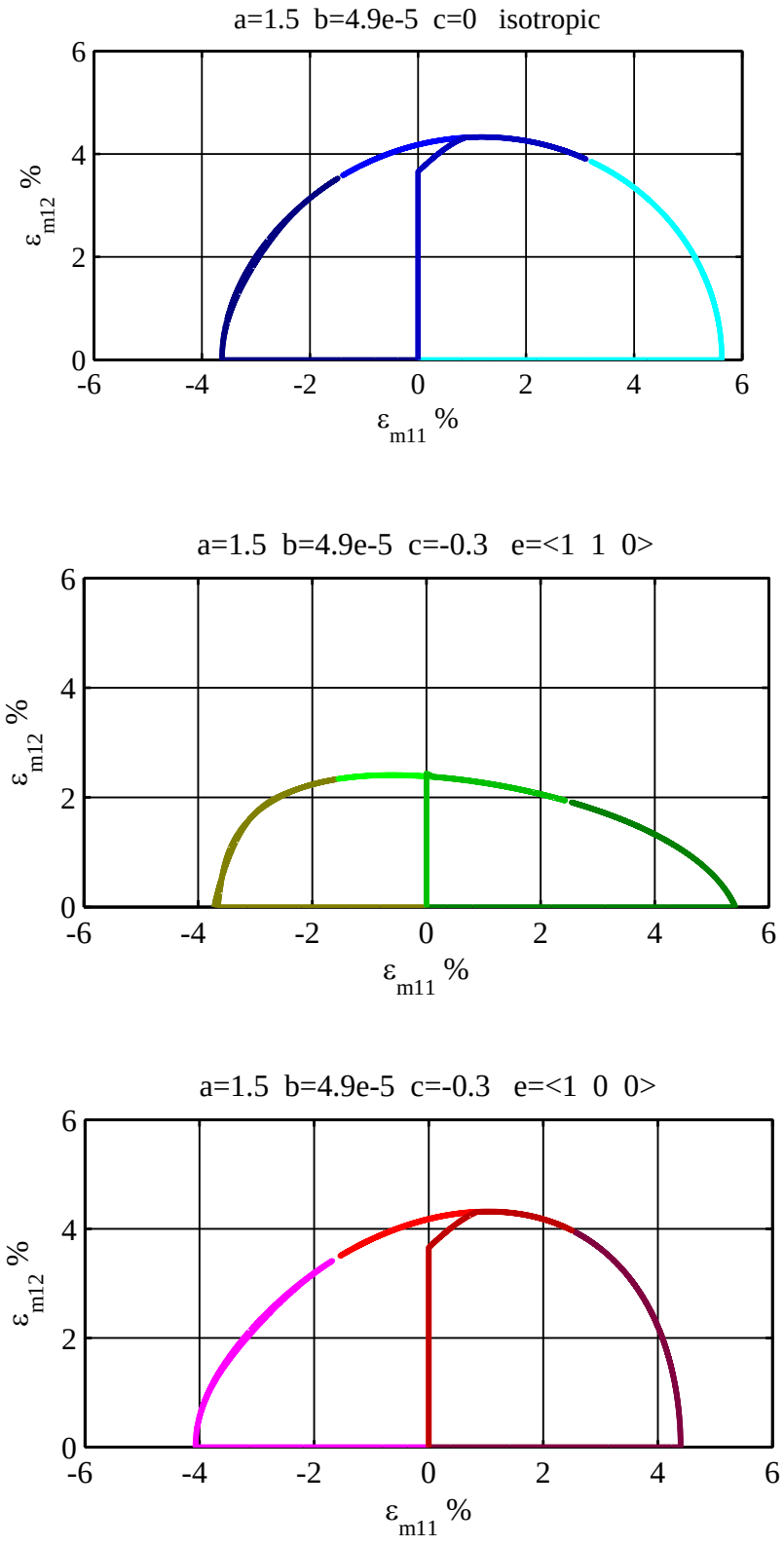

Figure 3.31: The recoverable torsion vs. the recoverable extension in NiTi polycrystals with isotropic fiber textures.

Chapter 4

Phase Transformation in Iron

4.1 Introduction

In this chapter we extend the constitutive framework, presented in chapter 2, to study the martensitic phase transformation and thermomechanical behavior of pure iron. For this material compared to SMAs, the transformation strains are larger, the stresses are larger and the plasticity is more involved. There is extensive literature on the experimental study of rate sensitivity of iron and its deformation mechanisms. Here we base our analysis on recent experimental observations of Rittel et al. (41) (also see (54)) on characterization of the shear dominant, large strain mechanical response of pure iron over strain rates ranging from $\dot{\varepsilon} = 10^{-4}(1/s)$ to $\dot{\varepsilon} = 10^{4}(1/s)$. Under high strain rates iron undergoes a reversible phase transformation from a bcc crystallographic structure α to an hcp crystallographic structure ε. We use the kinetic relation as proposed in the two previous chapters to describe the evolution of the microstructure. We also assume that the overall material response can be described by the Johnson-Cook constitutive relation, which is a widely used phenomenological model.

4.2 Model

We follow the model presented in chapter 2 with some modifications of the plasticity. The stress-strain relation is given by (2.21). The evolution of the transformation

strain is given by (2.27), while the evolution of λ is given by (2.26). We replace (2.28) for plasticity with the Johnson-Cook model described in detail in section 4.2.1. The energy equation (2.31) will be also modified slightly as described in section 4.2.2.

4.2.1 Johnson-Cook

At high strain rates material experiences thermal softening that would compete with the strain rate hardening effect. Thermal softening is caused by the temperature rise of the specimen, which happens as a result of the substantial amount of heat generated in the process. In order to assess the contribution of thermal softening we assume that the overall material response is described by the Johnson-Cook constitutive relation that describes the response of a number of metals fairly well:

$$\sigma \;=\; (\sigma_0 + B\,{\varepsilon_p}^n)\left(1 \;+\; C\ln\left(\frac{\dot{\varepsilon}_p}{\dot{\varepsilon}_0}\right)\right)\left(\frac{1 \;-\; D\exp(\theta_*)^m}{1 \;-\; D}\right), \tag{4.1}$$

where

$$\theta_* \;=\; \left(\frac{\theta \;-\; \theta_r}{\theta_r \;-\; \theta_m}\right). \tag{4.2}$$

Here σ_0, B, n, C, D and m are six model parameters and one needs to fit them to experiments. In particular here we use experimental results of Rittel et al. (41) to evaluate these model parameters. Further, θ_r is the reference temperature at which σ_0 is measured, θ_m is the melting temperature of the material and $\dot{\varepsilon_0}$ is a reference strain rate at which yield occurs at σ_0.

The Johnson-Cook constitutive relation has three distinct terms, covering the strain hardening, strain rate dependence and temperature softening of the material, respectively. In order to capture the nonlinear response of the material under both quasistatic and dynamic loading conditions the Johnson-Cook model needs to be modified. Experimental observations show that the flow stress of iron shows a different strain rate dependence under quasistatic and dynamic loading conditions. A schematic representation of these observations is shown in Figure 4.1.

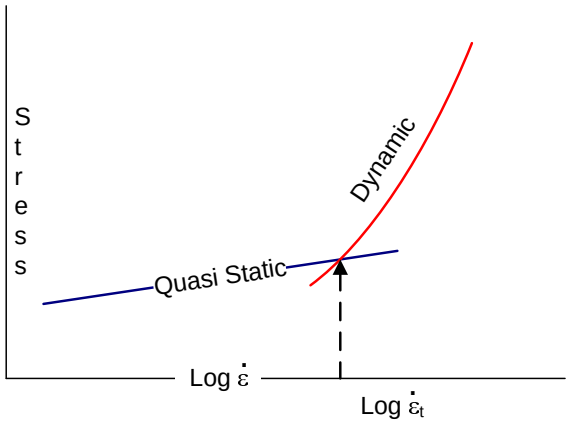

Figure 4.1: Strain rate dependence of the flow stress.

As illustrated in this figure by following the commonly used techniques in the literature, the flow stress can be described through applying two distinctive relations for static and dynamic tests:

$$\sigma = (\sigma_0 + B\,{\varepsilon_p}^n)\left(1 + C_1 \ln\left(\frac{\dot{\varepsilon}_p}{\dot{\varepsilon}_{0_1}}\right)\right)\left(\frac{1 - D\exp(\theta_*)^m}{1 - D}\right) \quad \text{for quasistatic case}$$

$$\sigma = (\sigma_0 + B\,{\varepsilon_p}^n)\left(1 + C_2 \ln\left(\frac{\dot{\varepsilon}_p}{\dot{\varepsilon}_{0_2}}\right)\right)\left(\frac{1 - D\exp(\theta_*)^m}{1 - D}\right) \quad \text{for dynamic case}$$

where parameters C_1, C_2, $\dot{\varepsilon_{0_1}}$ and $\dot{\varepsilon_{0_2}}$ remain to be evaluated through experiments. In order to make the transition between the quasistatic and the dynamic conditions smooth, we use a continuous function as follows:

$$S(\dot{\varepsilon}_p, s_1, s_2, \dot{\varepsilon}_t) = s_1 + \frac{s_2 - s_1}{2}\left(1 + \tanh\left(s \ln\frac{\dot{\varepsilon}_p}{\dot{\varepsilon}_t}\right)\right). \tag{4.3}$$

Function S is close to a Heaviside function with a smooth and continuous variation around the transition strain rate $\dot{\varepsilon}_t$. S is equal to s_1 when $\dot{\varepsilon} < \dot{\varepsilon}_t$ and equal to s_2 when $\dot{\varepsilon} > \dot{\varepsilon}_t$. Scaling factor s controls the size of the transition interval and $s = 4/\ln(1 + .01\,\delta)$ provides 99.9% of the transition from one region to the other to happen within $\pm\,\delta\%$ vicinity of the transition strain rate $\dot{\varepsilon}_t$.

We use function S to smoothen the transition between C_1 and C_2 as well as $\dot{\varepsilon}_{0_1}$

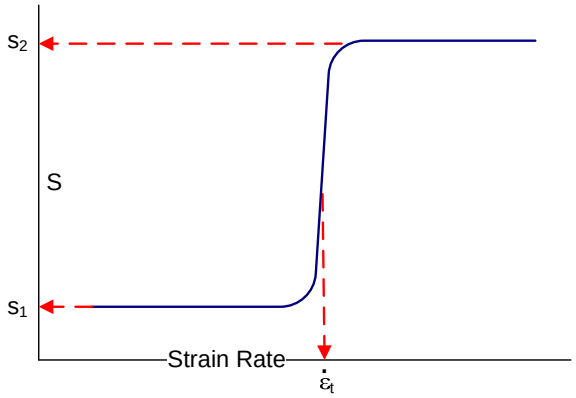

Figure 4.2: Schematic representation of the S function.

and $\dot{\varepsilon}_{0_2}$ as follows:

$$C = S(\dot{\varepsilon}_p, C_1, C_2, \dot{\varepsilon}_t) = C_1 + \frac{C_2 - C_1}{2}\left(1 + \tanh\left(s \ln \frac{\dot{\varepsilon}_p}{\dot{\varepsilon}_t}\right)\right) \tag{4.4}$$

$$\dot{\varepsilon}_0 = S(\dot{\varepsilon}_p, \dot{\varepsilon}_{0_1}, \dot{\varepsilon}_{0_2}, \dot{\varepsilon}_t) = \dot{\varepsilon}_{0_1} + \frac{\dot{\varepsilon}_{0_2} - \dot{\varepsilon}_{0_1}}{2}\left(1 + \tanh\left(s \ln \frac{\dot{\varepsilon}_p}{\dot{\varepsilon}_t}\right)\right) \tag{4.5}$$

These modifications would enable the Johnson-Cook model to capture the different strain rate hardening trends of the material under low and high strain rates properly.

4.2.2 Temperature evolution

In deriving the energy balance in chapter 2 we assumed that the entire plastic work is converted to heat. Experimental observations show that this is not true and Rosakis et al. (42) have studied this in detail. Adapting their derivation, we modify (2.31) to be

$$c_p\dot{\theta} = \dot{\lambda}\theta\frac{\mathcal{L}}{\theta_{cr}} - q_x + r + d_\lambda\dot{\lambda} + d_{\varepsilon_m}\dot{\varepsilon}_m + \beta d_{\varepsilon_p}\dot{\varepsilon}_p, \tag{4.6}$$

where β is the fraction of the plastic work converted into heating.

Assuming adiabatic condition ($q = r = 0$) and neglecting the dissipation associ-

ated with $\dot{\lambda}$ and $\dot{\varepsilon}_m$ and recalling that $d_{\varepsilon_p} = \sigma$, we obtain

$$c_p\dot{\theta} = \theta\dot{\lambda}\frac{\mathcal{L}}{\theta_{cr}} + \beta\sigma\,\dot{\varepsilon}_p. \tag{4.7}$$

Integrating this, we obtain a relation between temperature, volume fraction of martensite, latent heat, specific heat and the plastic work:

$$\theta(t) = \exp\left(\frac{(\lambda-\lambda_0)\,\mathcal{L}}{c_p\,\theta_{cr}}\right)\left(\theta_0 + \int_0^t \exp\left(-\frac{(\lambda-\lambda_0)\,\mathcal{L})}{c_p\,\theta_{cr}}\right)\frac{\beta\sigma\dot{\varepsilon}_p}{c_p}\,d\tau\right). \tag{4.8}$$

It should be noted that it is common to assume the fraction β of the plastic work converted into heating to be a constant typically chosen between 0.8 and 1. This was first observed through quasistatic experiments of Taylor et al. (52), (20) who studied the remaining latent heat in a metal after cold working. More recently fully dynamic experiments suggest that β depends strongly on both strain and strain rate for various engineering materials. Here as we study the coupled thermomechanic response of pure iron under a wide interval of strain rates we choose β as a function of strain and strain rate both. We use experimental observations of Rittel et al. to choose the form of this function.

4.2.3 Further approximation

Since we are interested in large strains, the plastic strain ε_p and transformation strain ε_m are significantly larger than the elastic strain ε_e. Therefore we ignore it in the sequel and the σ stress as a constraint stress and drop the stress-strain relation (2.21). We also assume that ε_m evolves very fast to its limit and remains there. Therefore we treat it as a constant and drop (2.27). In summary we solve (4.1), (4.8) and (2.26).

4.3 Demonstration

In this section the model is demonstrated using strain-controlled experiments. We demonstrate that our model is consistent with the observed stress-strain response of pure iron for a wide range of strain rates. It is able to capture both the thermal softening effects as well as the rate hardening. We first fit the Johnson-Cook model to the experimental data and then, when the model is fully parameterized, we compare our simulation results with experimental observations. Throughout this section, the material parameters as well as the model parameters are kept constant.

4.3.1 Parameters

Consistent with typical experiments on pure iron (see for example (18)), we consider the following parameter values:

$$\begin{aligned} \text{Atomic mass} \;&=\; 55.85 \times 10^{-3}\ \text{(kg/mol)} \qquad \text{and} \qquad \text{Density} \;=\; 7870\ \text{(kg/m3)} \\ \Delta S(\alpha \leftrightarrow \varepsilon) \;&=\; -\,2.54\ \text{(J/K/mol)} \qquad \text{and} \qquad \Delta H(\alpha \leftrightarrow \varepsilon) \;=\; 8.144 \times 10^{4}\ \text{(J/mol)} \\ E \;&=\; 190\ \text{(GPa)} \qquad \text{and} \qquad c_p \;=\; 3.5\ (\frac{\text{MJ}}{\text{m}^3\,{}^o\text{K}}) \end{aligned}$$

In all the simulations ambient temperature is assumed to be equal to 295^oK. We further assume that ε_m is equal to zero for the α phase and equal to 5% for the ε phase. Latent heat $\mathcal{L}$ of the phase transformation can be calculated from the above table of parameters. Critical temperature θ_{cr} is assumed to be equal to 800^oK. We also assume the following kinetic coefficients:

$$\dot{\lambda}^{+} = -\dot{\lambda}^{-} = 1, \quad p \;=\; 2\,.$$

Note that $\dot{\lambda}^{\pm}$ control the evolution rate of the volume fraction of martensite, are kept fixed in the entire chapter and chosen so that $\dot{\lambda}\,\varepsilon_m$ is smaller than $\dot{\varepsilon}_p$. The power of the kinetic law p controls the shape of its function as earlier described in preceding chapters.

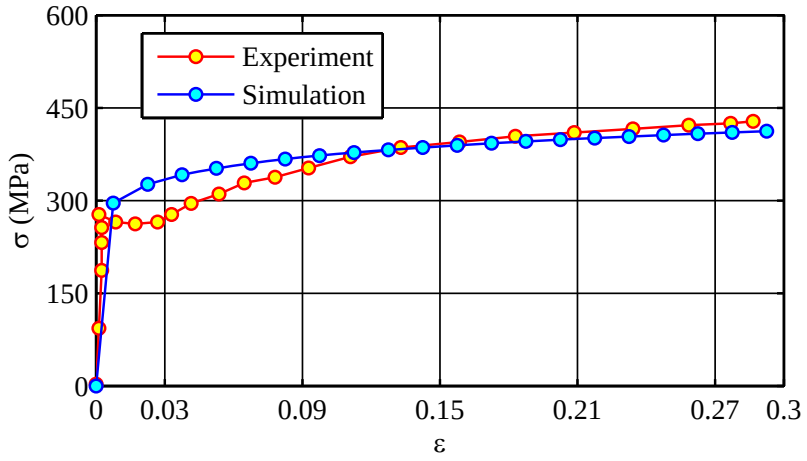

Figure 4.3: Quasistatic stress-strain response of pure iron.

4.3.2 Fitting the model to the experiment

The Johnson-Cook model has seven parameters in the form presented in (4.1). Three of these parameters (σ_0, B and n) belong to the first multiplying component and are determined by a fit to a quasistatic test. For such a test contributions of the strain rate hardening and thermal softening in the second and third multiplying components of the stress are negligible and these terms are essentially equal to 1. To determine σ_0, B and n we use experimental results of Rittel et al. for a quasistatic experiment on pure iron. Figure 4.3 shows results of such simulation along with the experimental results. Through the above simulation, values of the three parameters σ_0, B and n are determined:

$$\sigma_0 \;=\; 32.6 \text{ (MPa)} \qquad B \;=\; 430 \text{ (MPa)} \qquad n \;=\; 0.1$$

Here σ_0 is the yield stress, B is the pre-exponential factor, and n is the work-hardening coefficient.

To include effects of the strain rate hardening we should determine factors C_1, C_2 and $\dot{\varepsilon}_{0_1}$, $\dot{\varepsilon}_{0_2}$. We assume the transition strain rate $\dot{\varepsilon}_t$ to be equal to 100 $(1/s)$ and set the scaling factor s equal to 400, which provides that 99.9% of the transition from the quasistatic region to the dynamic region will happen within $\pm 1\%$ vicinity of the

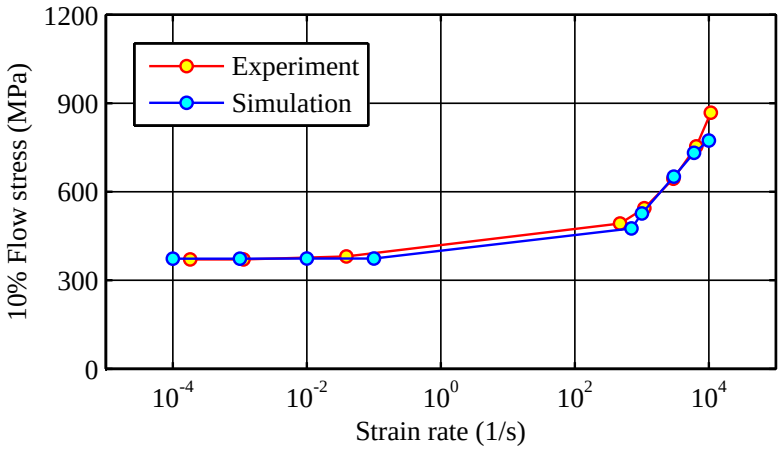

Figure 4.4: Flow stress dependence on strain rate.

transition strain rate $\dot{\varepsilon}_t = 100\ (1/s)$. Figure 4.4 demonstrates the rate dependence of the flow stress and compares simulation results with experimental observations. Through these simulations, values of C_1, C_2 and $\dot{\varepsilon}_{0_1}$, $\dot{\varepsilon}_{0_2}$ parameters are determined as follows:

$$\dot{\varepsilon}_{0_1} = 4 \times 10^{-5} \qquad C_1 = .00008 \qquad \dot{\varepsilon}_{0_2} = 344 \qquad C_2 = .385$$

Here we have one extra C and one extra $\dot{\varepsilon}_0$ to capture the rate dependence of the flow stress in pure iron properly. This is how Figure 4.4 is nicely comparable to Figure 4.1.

Finally we need to simulate the thermal softening effects in our simulations. This is the phenomena captured in the third and final term in the Johnson-Cook constitutive relation (4.1). In this term we have two unknown model parameters m and D as well as two extra parameters θ_r and θ_m. Temperature θ_m is the melting temperature and θ_r is a reference temperature. Figure 4.5 compares simulation results to the experimental observations on the dependence of the yield stress on temperature. Here we have assumed that $\theta_r = 295^o$K and $\theta_m = 1811^o$K. this figure completes the parametrization of the Johnson-Cook model by giving the following values for the remaining two parameters, m and D:

$$m = -9 \quad \text{and} \quad D = -4$$

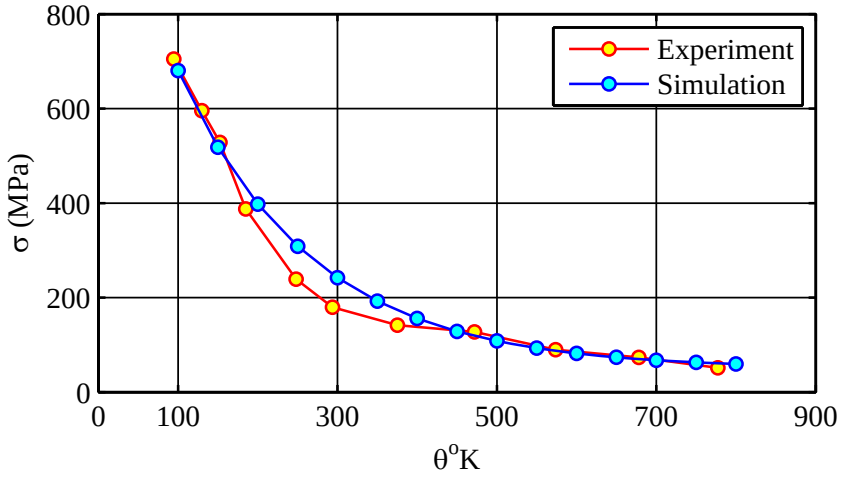

Figure 4.5: Temperature dependence of the yield stress.

Now we are ready to start our simulations using the Johnson-Cook model along with the phase transformation criteria and the temperature growth rule as presented in preceding sections. In order to include contribution of the plastic work in heating the material we also need to quantify factor β. As discussed earlier for dynamic conditions this factor is a function of strain and strain rate. Here we choose the following form for β to capture the rate and strain dependence of β qualitatively as suggested by experiments. Clearly we have made no attempt to be precise on β but rather qualitatively capture its dependence on strain and strain rate.

$$\beta \;=\; \frac{1}{2}\left(\frac{\dot{\varepsilon}_p}{\dot{\lambda}^+}\right)^2 (1 \,+\, 5\,\varepsilon\,(1 \,-\, \varepsilon)) \quad \text{for } \varepsilon \leq 1\,. \tag{4.9}$$

Figure (4.9) schematically shows β as a function of strain ε for three different strain rates. Note that here β is the equivalent to the β_{dif} as stated elsewhere. In (40) β_{dif} and β_{int} are defined as

$$\beta_{dif} \;=\; \frac{c_p\,\dot{\theta}}{\sigma\,\dot{\varepsilon}_p} \qquad \beta_{int} \;=\; \frac{c_p\,\theta}{\int \sigma\,\varepsilon_p\,\mathrm{d}\varepsilon_p}\,.$$

It should be noted that in absence of additional heat input it is expected that

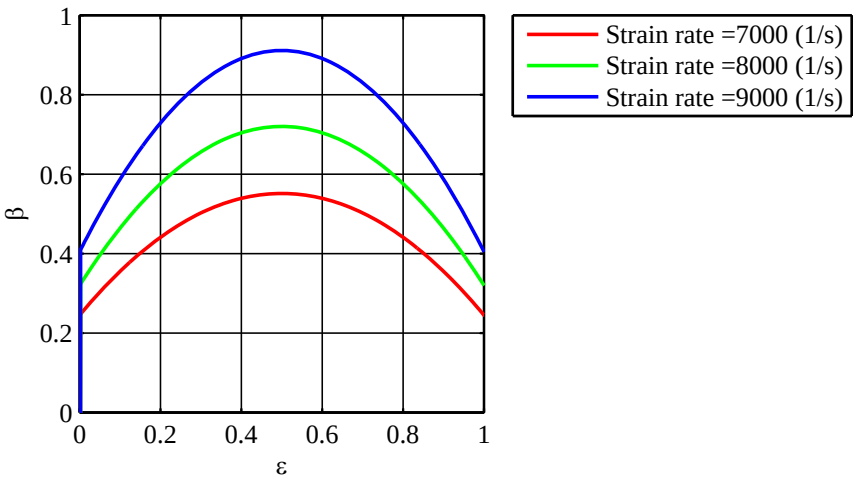

Figure 4.6: Schematic contribution of plastic work in generating heat as a function of strain and strain rate.

$\beta_{int} \leq 1$. Rittel et al. (41) however report that for high enough strain rates surprisingly β_{int} values above 1 are consistently reached. This would be meaningful if an internal heat source other than thermomechanical conversion of plastic work to heat existed.

As stated in (4.7) here we include thermal effects of the reversible phase transformation from α (bcc) to ε (hcp) phase of iron and modify the temperature growth rule. This extra factor would change the relation for the β_{dif} as

$$\beta_{dif} = \frac{c_p\,\dot{\theta}}{\sigma\,\dot{\varepsilon}_p} - \frac{\theta\,\dot{\lambda}\,\mathcal{L}}{\sigma\,\dot{\varepsilon}_p\,\theta_{cr}}\,. \tag{4.10}$$

4.3.3 Strain-controlled tests

We conclude this chapter by demonstrating the stress-strain response of pure iron for a wide range of strain rates. For each simulation we compare our results with experimental observations of Rittel et al. (41). Simulation results show that our model is consistent with the observed response of pure iron in strain-rate-controlled experiments.

As is apparent in the following simulations, the yield stress of iron increases by increasing strain rate. This has also been illustrated in Figure 4.4, where rate de-

pendency of the 10% flow stress is studied as a function of strain rate. It should be noted that at high enough strain rates thermal softening would overcome effects of strain hardening and material shows a gradual drop in the stress plateau as strain increases. This is demonstrated for the strain rates $\dot{\varepsilon} = 8400\ (1/s)$, $\dot{\varepsilon} = 9500\ (1/s)$ and $\dot{\varepsilon} = 10,000\ (1/s)$ in Figures 4.10, 4.13 and 4.14.

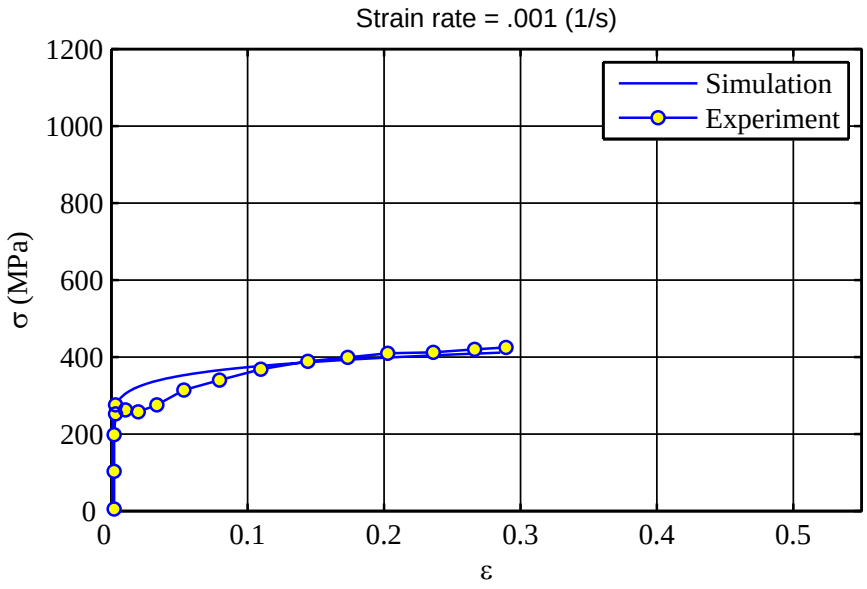

Figure 4.7: stress-strain response of pure iron for a quasistatic test.

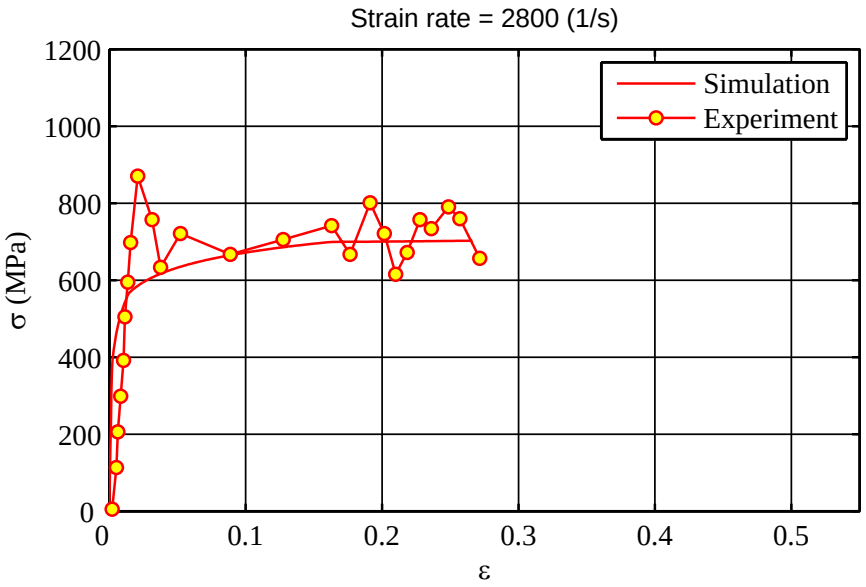

Figure 4.8: stress-strain response of pure iron for a dynamic test, $\dot{\varepsilon} = 2800(\frac{1}{s})$.

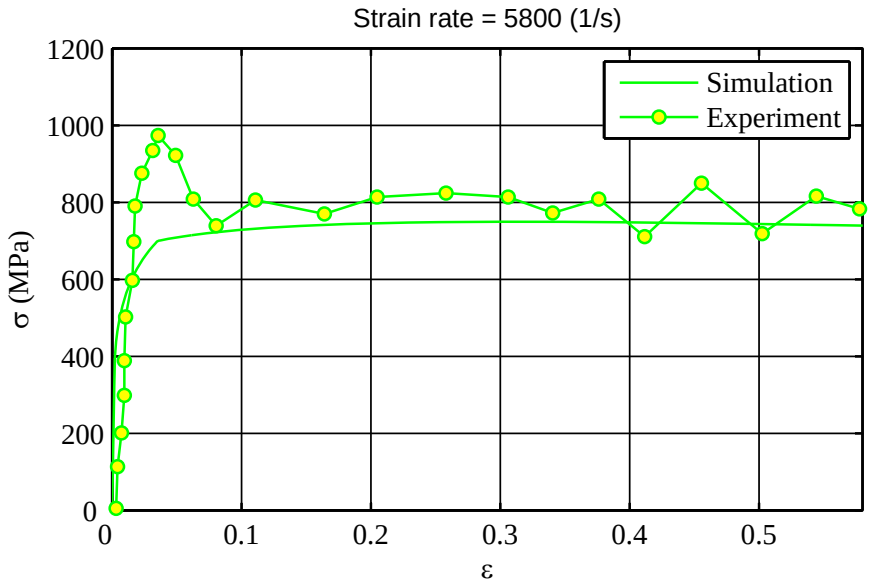

Figure 4.9: stress-strain response of pure iron for a dynamic test, $\dot{\varepsilon} = 5800(\frac{1}{s})$.

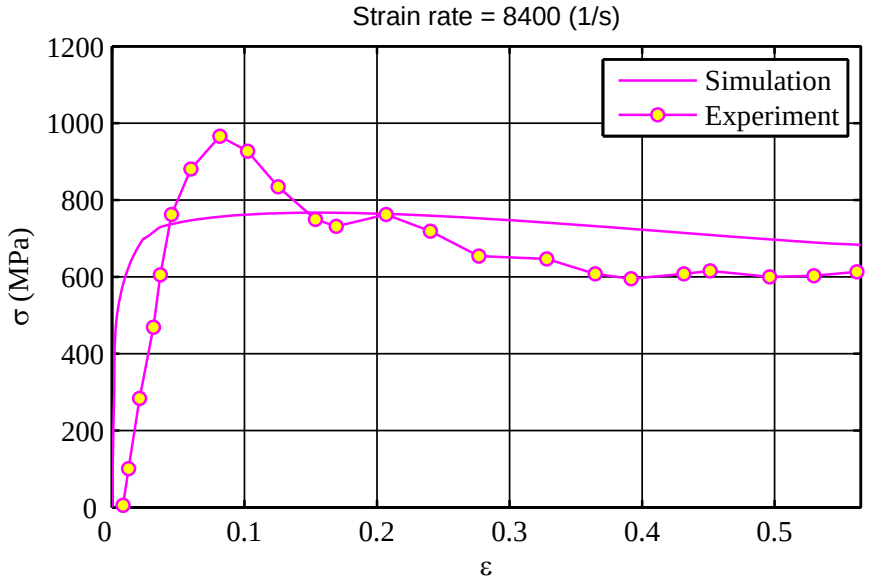

Figure 4.10: stress-strain response of pure iron for a dynamic test, $\dot{\varepsilon} = 8400(\frac{1}{s})$.

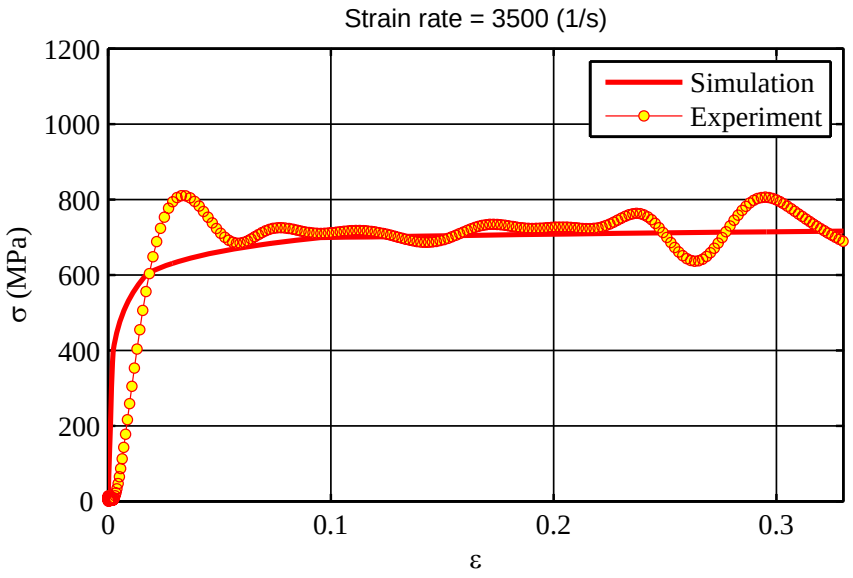

Figure 4.11: stress-strain response of pure iron for a dynamic test, $\dot{\varepsilon} = 3500(\frac{1}{s})$.

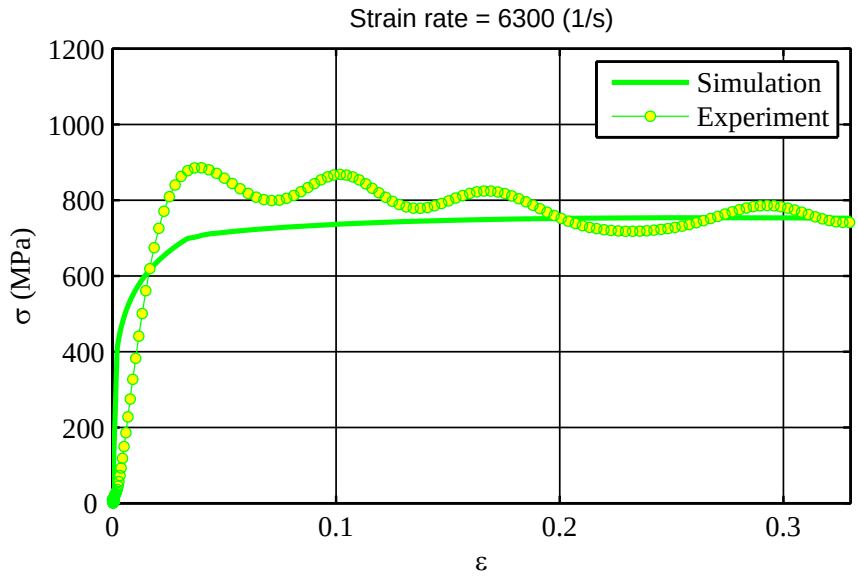

Figure 4.12: stress-strain response of pure iron for a dynamic test, $\dot{\varepsilon} = 6300(\frac{1}{s})$.

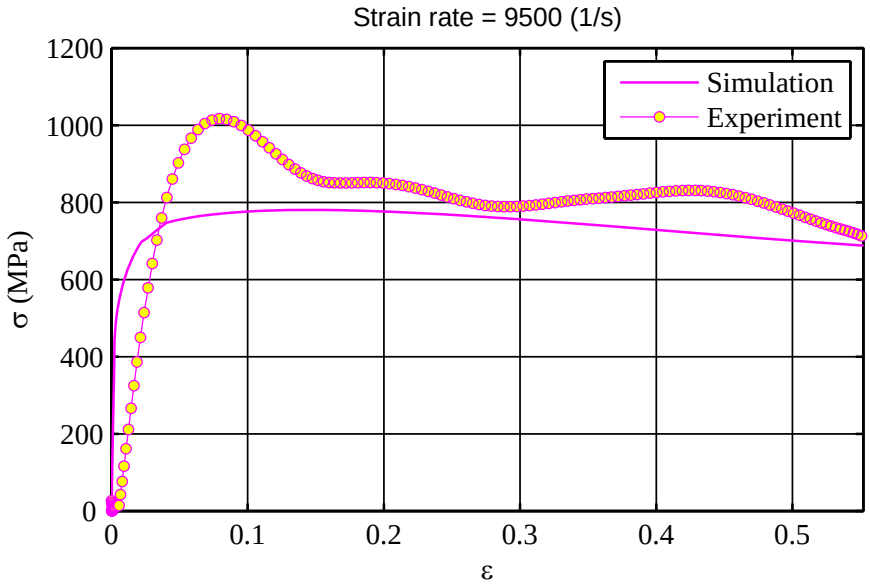

Figure 4.13: stress-strain response of pure iron for a dynamic test, $\dot{\varepsilon} = 9500(\frac{1}{s})$.

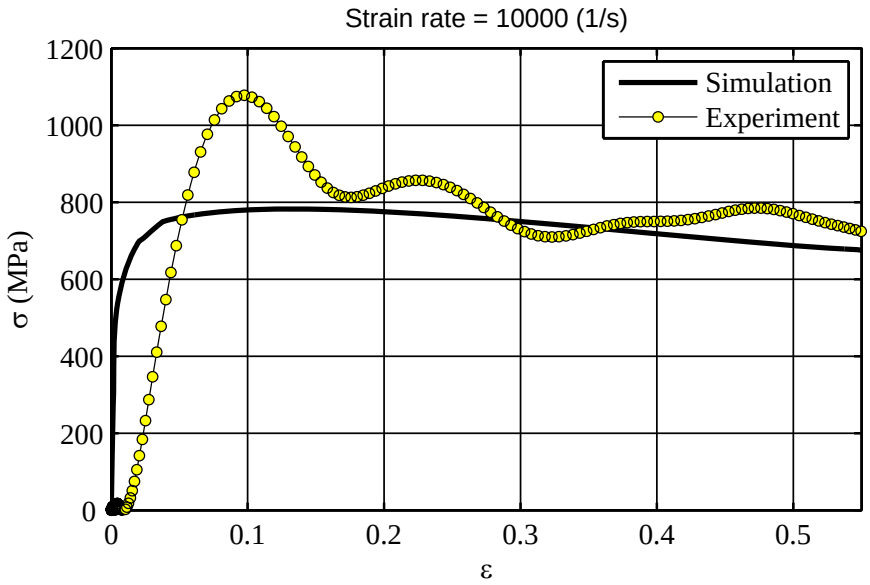

Figure 4.14: stress-strain response of pure iron for a dynamic test, $\dot{\varepsilon} = 10,000(\frac{1}{s})$.

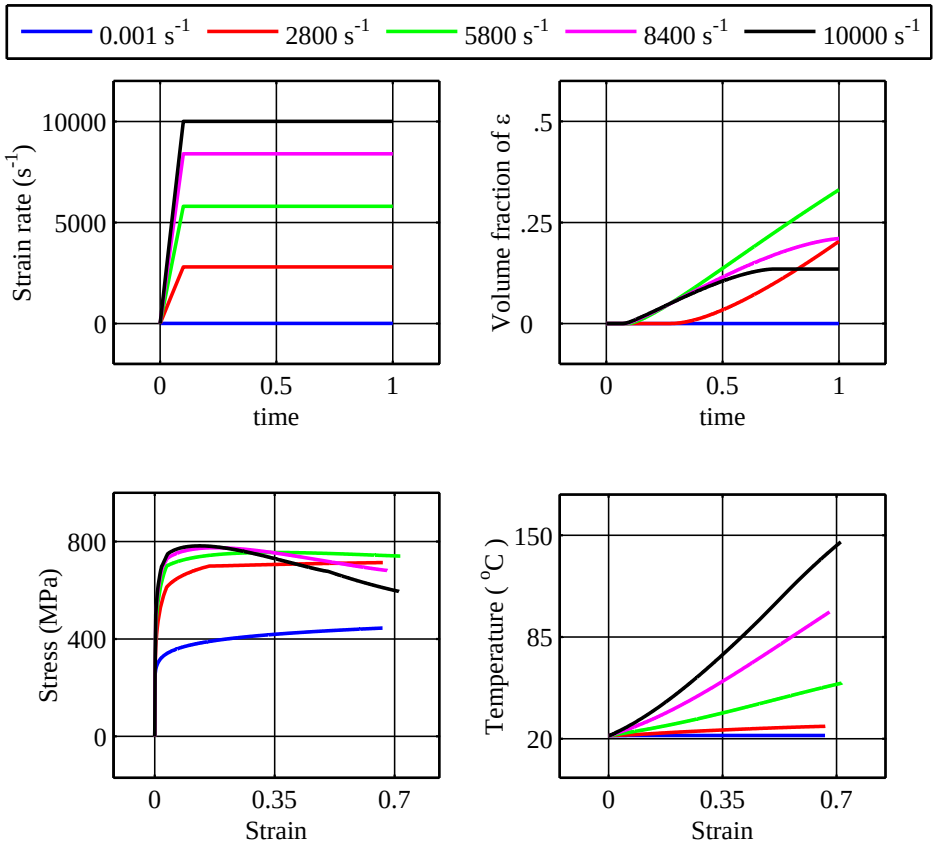

Figure 4.15: Phase transformation growth and temperature profile of pure iron for different strain rate experiments.

Here we also include a record of the phase transformation process along with the temperature growth in the material as a result of our simulations. As illustrated here for the quasistatic case, there is not much temperature increase observed in the material. This is qualitatively consistent with the observed phenomena in experiments that suggest at low strain rates material has enough time to diffuse the generated heat into the surroundings and temperature is almost constant in the deforming body. For higher strain rates, however, material does not get enough time to conduct out the generated heat and thus temperature of the body increases as deformation proceeds.

Figure 4.15 shows results of strain-controlled simulations for five different strain rates shown in the upper left corner, ranging from quasistatic to rates as high as $10,000(s^{-1})$. In the upper-right corner the growth of the volume fraction of the ε

phase with respect to the time duration of the simulation is pictured. It should be noted that the time duration of the test differs from one simulation to the other and the time axis is normalized by the duration time of each individual test. It is good to note that the release of thermal energy in the deforming body results in thermal softening which for the $\dot{\varepsilon} = 10,000\ s^{-1}$ results in a halt in the phase transformation process as shown with the black color.

Chapter 5

Conclusion

With their strongly nonlinear thermomechanical behavior, along with abrupt changes in their lattice structure, shape-memory alloys have found many applications in a wide variety of industries. These materials undergo a diffusionless solid to solid martensitic phase transformation from a high-temperature austenite phase to a low-temperature martensite phase. The martensite phase has a lower symmetry than austenite and as a result it has a number of symmetry related variants that make it difficult to fully describe the phase transformation process and the thermomechanically coupled behavior of these alloys. In this thesis a three-dimensional micromechanics-inspired constitutive model to describe the dynamic behavior of polycrystalline shape-memory alloys is developed.

In chapter 2 we start with a one-dimensional framework and present a model that builds on ideas generated from recent micromechanical studies of the underlying microstructure of shape-memory alloys. The two important concepts introduced in this chapter are the idea of the effective transformation strain and the use of kinetic relations. The different variants of martensite, along with the austenite, form complex microstructures that can evolve with load and temperature. A key difficulty in the constitutive modeling of these materials is to find an effective means of describing this evolution, especially in polycrystals. The effective transformation strain is the average transformation strain of the different variants averaged over a representative volume containing multiple grains after the material has formed an allowable microstructure. Another important idea in this model is the use of kinetic relations that cover a

wide range of strain rates. The usual balance laws do not fully determine the phase transformation growth and there is a need for additional constitutive information in the form of a kinetic relation. The kinetic relation is constructed such that the growth rate of the volume fraction of the martensitic phase is a constitutive function of the thermodynamic driving force and effectively of stress. The kinetic relation as proposed here is rate-dependent at larger driving forces and rate-independent at smaller driving forces, consistent with the experimental observations. This would make the model capable to capture the dynamic behavior of these alloys under a wide range of loading rates.

We demonstrated that the model captures both the superelasticity and the shape-memory effect and compared our simulations with experimental results. We also showed the ability of the model in capturing the tension-compression asymmetry and studied the effect of ambient temperature and loading rate on the response of the material. We note that adiabatic heating normally affects the stress-strain response of the deforming body and in order to interpret the effect of loading rate properly we examined the relative role of the two factors that lead to the apparent hardening at high rates. For this we considered two different kinetic relations, a rate-dependent and a rate-independent model. Through running a number of examples we showed that both the transition from isothermal to adiabatic conditions as well as inherent rate dependence of the kinetic relation can give rise to hardening of the response with increasing rate. However the former is limited to an increase of stress as described in chapter 2 and any further hardening is necessarily a manifestation of inherent rate dependence of the phase transformation process. Inspired by recent experimental observations, we discussed internal loops of the stress-strain hysteresis for a simple triangular applied stress function. Finally since phase transformation often competes with plasticity in shape-memory alloys, we incorporated that phenomenon into our model and studied the interplay of the plastic yield and the phase transformation process and their effects on the stress-strain response of the material.

In materials like shape-memory alloys that involve the evolution of internal variables, the stress-strain curve varies with the methodology of the experiment. A par-

ticularly popular means of measuring material properties at high deformation rates is the Kolsky or split-Hopkinson bar. We concluded chapter 2 by considering a simulation of the Kolsky bar experiment. We studied the effect of the pulse amplitude, pulse shape, pulse duration and the ambient temperature on the phase transformation process as well as the stress-strain response of the material. Our simulations emphasized how sensitively the stress-strain curve can depend on the input pulse and pointed to the importance of designing an appropriate pulse shape in experiments. The strain rate of the shape-memory alloy sample varies significantly as its microstructure changes, and obtaining a constant strain rate during the austenite to martensite phase transformation in experiments is fairly complicated. We addressed this by using the model to design a pulse that yields a desired strain rate history. We considered two desired strain rates: first a constant strain rate to investigate the loading and then a jump test to study the loading and unloading together.

Chapter 3 presents our micromechanics-inspired constitutive model for polycrystalline shape-memory alloys in three dimensions. The model is a generalization of the one-dimensional model and remains applicable in a wide range of temperatures and strain rates. It is able to reproduce stress-strain response for complex proportional and nonproportional loading patterns and can simulate the effect of texture on a polycrystal of shape-memory alloy. Micromechanics origins of the model, the concepts emerged from those analysis and their relation to macroscopic properties in both single and polycrystals are presented. A major player of the present model is the idea of the effective transformation strain. The role of the phase transformation surface in this context is similar to that of the yield surface in elasto-plastic materials. We considered three types of transformation criterion: the isotropic and symmetric, the isotropic and asymmetric, and the anisotropic and asymmetric. We also showed how one can extract the shape and size of the phase transformation surface using experimental data. We considered proportional and non-proportional loading and unloading experiments. We also demonstrate thermomechanical coupling by studying stress-strain behavior of uniaxial tension-compression, pure shear and biaxial tension-compression tests for different initial temperatures. We considered two

types of temperature evolutions: adiabatic and non-adiabatic. We demonstrated the sensitivity of the stress-strain response to the changes of the convective heat transfer coefficient of the air for non-adiabatic thermal conditions. In order to study the effects of texture on the shape-memory response we chose an anisotropic framework and demonstrated how our model is able to predict the qualitative behavior of a polycrystal alloy and its dependence on texture. We carefully studied the phase transformation process, evolution of the internal variables and the stress-strain response for a number of non-proportional loading experiments under stress-controlled and strain-controlled conditions. Finally in chapter 4 we presented an extension of our constitutive model to study the martensitic phase transformations in pure iron under a wide range of loading rates ranging from quasistatic to high rate dynamic loading. We used our model to describe the evolution of the microstructure as a reversible phase transformation occurs from a (bcc) structure α to an (hcp) ε crystallographic structure. We studied two phenomena: rate hardening and thermal softening, and demonstrated their effects on the phase transformation and the stress-strain response of the material.

Chapter 6

Appendix A

6.1 An example of a MATLAB code for the stress controlled full-dimensional analysis of anisotropic shape-memory alloys

```
C ========================================
C  This program calculates strain, temperature and internal variables.
C ========================================
function Stress3D
clear all;
global A Tzero dplus parameterA parameterB parameterC eVector timestep duration w alpha tol power Dplus Dminus Tcirt cp LambdaDotPlus LambdaDotMinus LatentHeat

C ----------------------------------------
C    Material parameters
C ----------------------------------------
E = 65*10 ** 9;
nu = .33;
Ms = -51.55 + 273;
```

```
As = -6.36 + 273;
Tcrit = (Ms + As) / 2;
cp = 5.4*10 ** 6;
LatentHeat = 79*10 ** 6;
parameterA = 1.035;
parameterB = 0.000045;
parameterC = .6;
eVector = ((  1 1 0  ));
tol=parameterB / 10000;

C ------------------------------------------------------
C  Parameters of the kinetic relations
C ------------------------------------------------------
LambdaDotPlus = 10 ** 4;
LambdaDotMinus = -LambdaDotPlus;
power = 2;
alpha = 0.001;
dplus = LatentHeat * ( As - Ms ) / ( Ms + As );
dminus = -dplus;
Dplus = 1;
Dminus = -Dplus;

C ------------------------------------------------------
C  Loading parameters; sigma = A*sin(w*t)
C ------------------------------------------------------
A = 800*10 ** 6;
duration = 50 / LambdaDotPlus;
w = 2*pi / duration;
timestep = .0005 * duration;
Tzero = 295;
```

```
C ------------------------------------------------
C  Initial values for the internal variables
C ------------------------------------------------
index = 1;
time(index) = 0;
g(index) = -parameterB;
LambdaDot(index) = 0;
lambda(index) = 0;
s=stress(time(index));
sigma(: , : , index) = s(: , :);
epsilon(: , : , index) = zeros(3);
epsm(: , : , index) = zeros(3);
temperature(index) = Tzero;
D(index) = -WellEnergy(temperature(index)) / dplus;

C ------------------------------------------------
C  Time Procedure for the next time increments
C ------------------------------------------------
while time(index) < duration
index=index + 1;
time(index) = time(index-1) + timestep;

C ------------------------------------------------
C  Reading of stress
C ------------------------------------------------
s=stress(time(index));
sigma(: , : , index) = s(: , :);
```

```
C ------------------------------------------------
C  Calculation of phase transformation strain
C ------------------------------------------------
(( epsm(: , : , index) , g(index) )) = epsmfunc ( g(index-1) , epsm(: , : , index-1) , sigma(: , : , index) );

C ------------------------------------------------
C  Calculation of the driving force
C ------------------------------------------------
D(index) = drivingforce(sigma(: , : , index) , temperature(index-1) , epsm(: , : , index));

C ------------------------------------------------
C  Calculation of martensite volume fraction
C ------------------------------------------------
(( lambda(index) , LambdaDot(index) )) = lambdafunc(D(index) , lambda(index-1));

C ------------------------------------------------
C  Calculation of total strain
C ------------------------------------------------
epsilon(: , : , index) = lambda(index) * epsm(: , : , index) + ((1 + nu) * sigma(: , : , index) - nu * trace(sigma(: , : , index)) * eye(3)) / E;

C ------------------------------------------------
C  Calculation of current temperature
C ------------------------------------------------
temperature(index) = tempfunc(lambda(index));
end
```

```
C ------------------------------------------------------
C  Prepeation to print
C ------------------------------------------------------
for ii = 1:1:index;
sigm11(ii) = sigma(1 , 1 , ii);
sigm12(ii) = sigma(1 , 2 , ii);
sigm13(ii) = sigma(1 , 3 , ii);
sigm22(ii) = sigma(2 , 2 , ii);
sigm23(ii) = sigma(2 , 3 , ii);
sigm33(ii) = sigma(3 , 3 , ii);
epsm11(ii) = epsm(1 , 1 , ii);
epsm12(ii) = epsm(1 , 2 , ii);
epsm13(ii) = epsm(1 , 3 , ii);
epsm22(ii) = epsm(2 , 2 , ii);
epsm23(ii) = epsm(2 , 3 , ii);
epsm33(ii) = epsm(3 , 3 , ii);
epsi11(ii) = epsilon(1 , 1 , ii);
epsi12(ii) = epsilon(1 , 2 , ii);
epsi13(ii) = epsilon(1 , 3 , ii);
epsi22(ii) = epsilon(2 , 2 , ii);
epsi23(ii) = epsilon(2 , 3 , ii);
epsi33(ii) = epsilon(3 , 3 , ii);
end

set(0 , 'DefaultFigureColor' , (( 1 1 1 )) , 'DefaultAxesFontName' , 'Times New
Roman' , 'DefaultAxesFontSize' , 11 , 'DefaultAxesFontWeight' , 'normal' , 'Default-
AxesLineWidth' , 1)
LineWidthSize = 1.5;
LineStyleFormat='-';
```

```
C ---------------------------------------
C  Printing a sample
C ---------------------------------------
figure(1)
plot(time / duration , sigm11 / 10 ** 6 , 'LineWidth' , LineWidthSize , 'LineStyle' ,
LineStyleFormat , 'Color' , (( c1 , c2 , c3 )))
xlabel('time')
ylabel('sigma11 (MPa)')
xlim((( 0 , 1 )))
ylim((( -1000 , 1000 )))
grid on
hold on
ax1=gca;
set(ax1 , 'XTick' , (( 0 , .5 , 1 )) , 'YTick' , (( -1000 , 0 , 1000 )) , 'GridLineStyle' , '-');

C =======================================
C  current stress
C =======================================
function stressT=stress(t)
global w A duration

stressT(1 , 1) = 0; stressT(1 , 2) = 0; stressT(1 , 3) = 0;
stressT(2 , 2) = 0; stressT(2 , 3) = 0; stressT(3 , 3) = 0;
t1 = duration / 4; t2 = 2 * t1; t3= 3 * t1; t4 = 4 * t1;

if t<=t1
stressT(1 , 1) = A * (t / t1);
stressT(2 , 2) = 0;
```

```
elseif and(t<=t2 , t>t1);
stressT(1 , 1) = A;
stressT(2 , 2) = -A * (t-t1) / (t2-t1);
elseif and(t<=t3 , t>t2);
stressT(1 , 1) = A;
stressT(2 , 2) = -A * (t3-t) / (t3-t2);
elseif and(t<=t4 , t>t3);
stressT(1 , 1) = A * (t4-t) / (t4-t3);
stressT(2 , 2) = 0;
else
stressT(1 , 1) = 0;
stressT(2 , 2) = 0;
end
for i = 1:1:3
for j = i:1:3
stressT(j , i) = stressT(i , j);
end
end


C ========================================
C  the yield criterion
C ========================================
function gfunction=gfunc(M)
global parameterA parameterB parameterC eVector

gfunction = (1 / 2 * trace(M*M)) ** (3 / 2) - parameterA * det(M) - parameterC * (eVector * (eVector*M)') ** 3 - parameterB;
```

```
C ========================================
C  current epsm
C ========================================
function ((  NewEpsm , NewG  )) = epsmfunc(gval , epsmval , sigmaval);
global timestep alpha tol

C ----------------------------------------
C  Growth rate of epsm
C ----------------------------------------
epsmdot = alpha * ( sigmaval - trace(sigmaval) / 3 * eye(3) );
epsmdot = trfree(epsmdot);

C ----------------------------------------
C  First guess on epsm
C ----------------------------------------
epsmstar = epsmval + epsmdot * timestep;
epsmstar = trfree(epsmstar);

C ----------------------------------------
C  Evaluate yield criteria based on the 1st guess
C ----------------------------------------
NewG = gfunc(epsmstar);

C ----------------------------------------
C  Check to see if yield boundry has been reached
C ----------------------------------------
if NewG<=0
NewEpsm=epsmstar;
if NewG>=-tol
NewG = 0;
```

```
end
else

C ---------------------------------------
C  Correct epsm if yield boundary is crossed
C ---------------------------------------
if gval = 0
zzettaa = 0;
epsmA = epsmval;
else
((  epsmA , zzettaa  )) = epsmAfinder ( sigmaval , epsmval );
epsmA=trfree(epsmA);
end
epsmB = epsmA + epsmADot ( sigmaval , epsmA ) * ( 1 - zzettaa ) * timestep;
epsmB = trfree(epsmB);
NewEpsm = epsmFinal(epsmB);
NewEpsm = trfree(NewEpsm);
NewG = 0;
end



C =======================================
C  find epsm moving on the yield boundary
C =======================================
function ((  epsmA , zzettaa  )) = epsmAfinder(sT , eT)
global timestep parameterA parameterC eVector alpha tol

m = 1;
zzettaaV(m) = .1;
Dzzettaa = 1;
```

```
Tolzzettaa = .01;
while Dzzettaa>Tolzzettaa
epsmA=eT + (zzettaaV(m ) * timestep ) * alpha*trfree(sT);
Cofprime = (cof(epsmA))';
eDOTepsmDOTe = 0;

for i = 1:1:3
for j=i:1:3
eDOTepsmDOTe = eDOTepsmDOTe + eVector(i ) * epsmA(i , j ) * eVector(j);
end
end
trfreeST = trfree(sT);
dgdz = 0;

for i = 1:1:3
for j = i:1:3
dgdz = dgdz + alpha*timestep * (3 / ( 8 ** (1 / 2) ) * normt(epsmA ) * epsmA(i ,
j) - 3 * parameterC * (eDOTepsmDOTe) ** 2 * eVector(i) * eVector(j)) * trfreeST(i
, j) - parameterA * Cofprime(i , j);
end
end

if abs(gfunc(epsmA))<=tol
zzettaaV(m + 1) = zzettaaV(m);
Dzzettaa = 0;
else
zzettaaV(m + 1) = zzettaaV(m)-gfunc(epsmA) / dgdz;
if zzettaaV(m + 1)>=1
zzettaaV(m + 1) = 1;
elseif zzettaaV(m + 1)<=0
```

```
zzettaaV(m + 1) = 0;
end
Dzzettaa = abs ( zzettaaV ( m + 1 ) - zzettaaV(m) );
end
m = m + 1;
if m>10000
pause
end
end
zzettaa = zzettaaV(m);



C ==========================================
C  growth rate of epsmA
C ==========================================
function epsmADotT = epsmADot( stressA , epsmA )
global parameterA parameterB parameterC eVector alpha

normM = normt(epsmA);
cofacM = cof(epsmA);
eDOTepsmDOTe = 0;
for i = 1:1:3
for j = i:1:3
eDOTepsmDOTe = eDOTepsmDOTe + eVector(i ) * epsmA(i , j ) * eVector(j);
end
end
AMatrix = 3 / (8 ** (1 / 2) ) * normM*epsmA-parameterA*cofacM'-3*parameterC
* (eDOTepsmDOTe) ** 2*eVector'*eVector;
AMatrixNorm = normt(AMatrix);
AMatrixstressA = product(AMatrix , stressA);
```

```
BMatrix = stressA - AMatrix / AMatrixNorm ** 2 * AMatrixstressA;
epsmADotT = alpha * trfree(BMatrix);



C ========================================
C  finding new epsm via Newton Raphson
C ========================================
function epsmNR=epsmFinal(epsmB)
global parameterA parameterB parameterC eVector tol

Dbeta = 1;
Tolbeta = .00001;
m = 1;
betaV(m) = 1;
while Dbeta>Tolbeta
betaV(m + 1) = 2*betaV(m) / 3 + parameterB / (3 * (betaV(m)) ** 2 * (gfunc(epsmB)
+ parameterB));
Dbeta = abs(betaV(m + 1)-betaV(m));
m = m + 1;
if m>10000
pause
end
end
beta = betaV(m-1);

gepsmNR = beta ** 3 * ( gfunc(epsmB) + parameterB ) - parameterB;
if abs(gepsmNR)>tol
pause
end
epsmNR = beta * epsmB;
```

```
C ========================================
C  driving force
C ========================================
function Dval = drivingforce(stressval , tempval , epsmval)
global dplus

Dval = ( product ( epsmval , stressval ) - WellEnergy(tempval) ) / dplus;



C ========================================
C  current lambda
C ========================================
function ((  lambdaval , lambdadotval  )) = lambdafunc(Dval , lambdaval)
global timestep power Dplus Dminus LambdaDotPlus LambdaDotMinus

if and(Dval>Dplus , lambdaval<1)
lambdadotval = LambdaDotPlus * (1 + (Dval-Dplus) ** (-1)) ** (-1 / power);
elseif and(Dval<Dminus , lambdaval>0)
lambdadotval = LambdaDotMinus * (1 + (Dminus-Dval) ** (-1)) ** (-1 / power);
else
lambdadotval = 0;
end
lambdaval = lambdadotval * timestep + lambdaval;
if lambdaval<0
lambdaval = 0;
elseif lambdaval>1
lambdaval = 1;
end
```

```
C ========================================
C  jump in the free energy between two phases
C ========================================
function wellval = WellEnergy(temp)
global Tcrit LatentHeat
wellval = LatentHeat / Tcrit * (temp-Tcrit);

C ========================================
C  current temperature
C ========================================
function tempval=tempfunc(lambdaval)
global Tzero Tcrit LatentHeat cp

tempval = (exp( LatentHeat * lambdaval / cp / Tcrit) ) * Tzero;


C ========================================
C  deviatoric tesnor
C ========================================
function tracefree=trfree(T)

tracefree = T - trace(T) / 3* eye(3);


C ========================================
C  norm of a tesnor
C ========================================
function tensorialnorm=normt(M)
```

```
sum = 0;
for i = 1:1:3;
for j = 1:1:3;
sum = sum + M(i , j) ** 2;
end
end
tensorialnorm = sum ** (1 / 2);


C ========================================
C  product of two tensors
C ========================================
function tensorialproduct = product(M , N)

sum = 0;
for i = 1:1:3;
for j = 1:1:3;
sum = sum + M(i , j) * N(i , j);
end
end
tensorialproduct = sum;


C ========================================
C  cofactor of a tesnor
C ========================================
function cofactor=cof(M)

for i = 1:1:3;
for j = 1:1:3;
```

```
N = M;
N(i , :) = ((  ));
N(: , j) = ((  ));
cofactor(i , j) = (-1) ** (i + j) * det(N);
end
end
```

Bibliography

[1] R. Abeyaratne, C. Chu and R.D. James, Kinetics of materials with wiggly energies: Theory and application to the evolution of twinning microstructure in a Cu-Al-Ni alloy, *Phil. Mag. A* **73** 457-497 (1996).

[2] R. Abeyaratne and J.K. Knowles, A continuum model of a thermoelastic solid capable of undergoing phase-transitions, *J. Mech. Phys. Solids* **41** 541-571 (1993).

[3] F. Auricchio, R.L. Taylor and J. Lubliner, Shape-memory alloys: macromodelling and numerical simulations of the superelastic behavior, *Comp. Meth. Appl. Mech. Engng.* **146** 281-312 (1997).

[4] F. Auricchio and L. Petrini, A three-dimensional model describing stress-temperature induced solid phase transformations: solution algorithm and boundary value problems, *Int. J. Num. Meth. Engng.* **61** 807-836 (2004).

[5] J.M. Ball and R.D. James, Fine phase mixtures as minimizers of energy *Arch. Rat. Mech. Anal.* **100** 13-52 (1987).

[6] J.M. Ball, C. Chu and R.D. James, Hysteresis during stress-induced variant rearrangement, *J. de Phys. IV* **5** 245-251 (1995).

[7] K. Bhattacharya, Phase boundary propagation in heterogeneous bodies. *Proc. Royal Soc. London A* **455** 757-766 (1999).

[8] K. Bhattacharya, *Microstructure of martensite*, Oxford (2003).

[9] K. Bhattacharya and R.V. Kohn, Energy minimization and the recoverable strains of polycrystalline shape-memory alloys, *Arch. Rat. Mech. Anal.* **139** 99-180 (1997).

[10] K. Bhattacharya, P. Purohit and B. Craciun, The mobility of twin and phase boundaries. *J. de Phys. IV* **112** 163-166 (2003).

[11] K. Bhattacharya and A. Schlömerkemper, Transformation yield surface of shape-memory Alloys, *J. de Phys. IV* **115**, 155-162 (2004).

[12] A. Bhattacharyya, D.C. Lagoudas, Y. Wang and V.K. Kinra, On the role of thermoelectric heat transfer in the design of SMA actuators: theoretical modelling and experiments, *Smart Mater. Struct.* **4** 252-263 (1995).

[13] J.G. Boyd and D.C. Lagoudas, A thermodynamic constitutive model for shape memory materials: 1. The monolithic shape memory alloy, *Int. J. Plast.* **12** 843-873 (1996)

[14] L.C. Brinson, One dimensional constitutive behavior of shape memory alloys: thermo-mechanical derivation with non-constant material functions, *J. Intell. Mater. Syst. Struct.* **4** 22942 (1993).

[15] L.C. Brinson and R. Lammering, Finite element analysis of the behavior of shape memory alloys and their applications *Int. J. Solids Struct.* **30** 326180 (1993).

[16] L.C. Brinson and M.S. Huang, Simplifications and comparisons of shape memory alloy constitutive models *J. Intell. Mater. Syst. Struct.* **7** 10814 (1996).

[17] M. Brocca, L.C. Brinson and Z. Bazant Three-dimensional constitutive model for shape memory alloys based on microplane, *J. Mech. Phys. Solids* **50** 1051-1077 (2002).

[18] G. Chen and T.J. Ahrens, High pressure melting of iron-New experiments and calculations, *Phil. Trans. R. Soc. Lond.* **A354** 1251-1263 (1996).

[19] B.D. Coleman and W. Noll, The thermodynamics of elastic materials with heat conduction and viscosity, *Arch. Rat. Mech. Anal.* **13** 167-183 (1963).

[20] W.S. Farren and G.I. Taylor, The heat developed during plastic extension of metals, *Proc. Roy. Soc. London* **A107** 422-451 (1925).

[21] Y. Huo and I. Müller, Nonequilibrium thermodynamics of pseudoelasticity, *Cont. Mech. Thermodyn.* bf 5 163-204 (1993).

[22] M. Huang and L.C. Brinson, Multivariant model for single crystal shape memory alloy behavior, *J. Mech. Phys. Solids* **46** 1379-1409 (1998).

[23] H. Inoue, N. Miwa and N. Inakazu, Texture and shape memory strain in TiNi alloy sheets, *Acta Mat.* **44** 4825-4834 (1996).

[24] Y.J. Jung, P. Papadopoulos and R.O. Ritchie, Constitutive modelling and numerical simulation of multivariant phase transformation in superelastic shape-memory alloys, *Int. J. Num. Meth. Engng.* **60** 429-460 (2004).

[25] C. Lexcellent and P. Blanc, Phase transformation yield surface determination for some shape memory alloys *Acta Mat.* **52** 2317-2324 (2004).

[26] C. Lexcellent, B.C. Goo, Q.P. Sun and J. Bernardini, Characterization, thermomechanical behaviour and micromechanical-based constitutive model of shape-memory Cu-Zn-Al single crystals. *Acta Mat.* **44** 3773-3780 (1996).

[27] C. Lexcellent, A. Vivet, C. Bouvet, S. Calloch and P. Blanc, Experimental and numerical determinations of the initial surface of phase transformation under biaxial polycrystalline shape-memory alloys *J. Mech. Phys. Solids* **50** 2717-2735 (2002).

[28] C. Liang and C.A. Rogers, One-dimensional thermomechanical constitutive relations for shape memory material *J. Intell. Mater. Syst. Struct.* **1** 20734 (1990).

[29] Z.K. Lu and G.J. Weng, Martensitic transformation and stress-strain relations of shape-memory alloys, *J. Mech. Phys. Solids* **45** 1905 (1997).

[30] F. Marketz and F.D. Fischer, Modelling the mechanical behavior of shape memory alloys under variant coalescence, *Comp. Mat. Sci.* bf 5 210-226 (1996).

[31] J.M. McNaney, V. Imbeni, Y. Jung, P. Papadopoulos and R.O. Ritchie, An experimental study of the superelastic effect in a shape-memory Nitinol alloy under biaxial loading, *Mech. Mater.* **35** 969-986 (2003).

[32] H. Naito, Y. Matsuzaki and T. Ikeda, A unified constitutive model of phase transformations and rearrangements of shape memory alloy wires subjected to quasistatic load, *Smart Mat. Struct.* **13** 535-543 (2004).

[33] S. Nemat-Nasser, J.Y. Choi, W.G. Guo, J.B. Isaacs and M. Taya High strain-rate, small strain response of a NiTi shape-memory alloy *J. Engng. Mat. Tech.* **127** 83-89 (2005).

[34] C. Niclaeys, T. Ben Zineb, S. Arbab-Chirani and E. Patoor, Determination of the interaction energy in the martensitic state, *Int. J. Plast.* **18** 1619-1647 (2002).

[35] K. Otsuka and C. M. Wayman, Shape Memory Materials, Cambridge University Press (1998).

[36] A. Paiva, M.A. Savi, A.M.B. Braga and P.M.CL. Pacheco, A constitutive model for shape memory alloys considering tensile-compressive asymmetry and plasticity, *Int. J. Sol. Struct* **42** 3439-3457 (2005).

[37] E. Patoor, C. Niclaeys, S. Arbab-Chirani and T. Ben Zineb, IUTAM Symposium on Mechanics of Martensite Phase Transformation in Solids. *New York: Kulwer Academic Publishers* p. 131 (2002).

[38] P.K. Purohit, Dynamics of phase transformations in strings, beams and atomic chains, Ph.D Thesis, California Institute of Technology (2002).

[39] M.A. Qidwai and D.C. Lagoudas, Numerical implementation of a shape memory alloy thermomechanical constitutive model using return mapping algorithms, *Int. J. Num. Meth. Engng.* **47** 1123-1168 (2000).

[40] D. Rittel and G. Ravichandran, High-strain-rate behavior of α-iron under shear dominant loading conditions, *15th Technical Meeting DYMAT.* Metz 1-2 June (2005).

[41] D. Rittel, G. Ravichandran and A. Venkert, The mechanical response of pure iron

at high strain rates under dominant shear, *Acta Mater.* accepted for publication, (2006).

[42] P. Rosakis , A.J. Rosakibs, G. Ravichandran and J. Hodowany, A thermodynamic internal variable model for the partition of plastic work into heat and stored energy in metals, *J. Mech. Phys. Solids* **48** 581-607 (2000).

[43] A. Sadjadpour and K. Bhattacharya, A micromechanics inspired constitutive model for shape-memory alloys: The one-dimensional case. *Smart Mat. Struct.* accepted for publication, (2006).

[44] A. Sadjadpour and K. Bhattacharya, A micromechanics inspired constitutive model for shape-memory alloys. In preparation (2005)

[45] A. Sadjadpour, D. Rittel, G. Ravichandran and K. Bhattacharya, Dynamic deformation of iron under shear. In preparation (2005)

[46] J. A. Shaw and S. Kyriakides, Thermomechanical aspects of NiTi. *J. Mech. Phys. Solids* **43 (8)**, 12431281 (1995).

[47] Y. C. Shu and K. Bhattacharyya, The influence of texture on the shape-memory effect in polycrystal, *Acta Mater.* **46** 5457-5473 (1998).

[48] P. Sittner, Y. Hara and M. Tokuda, Experimental study on the thermoelastic martensitic transformation in shape memory alloy polycrystal induced by combined external forces, *Metall. Mat. Trans.* **26** 29232935 (1995).

[49] V. Stoilov and A. Bhattacharyya A theoretical framework of one-dimensional sharp phase fronts in shape memory alloys, *Acta Mater.* **50** 4939-4952 (2002).

[50] Q.P. Sun and K.C. Hwang, Micromechanics modeling for the constitutive behavior of polycrystalline shape-memory alloys: 1. Derivation of general relations and 2. Study of individual phenomena, *J. Mech. Phys. Solids* **41** 1-17 and 19-33 (1993).

[51] K. Tanaka, A thermomechanical sketch of shape memory effect: one-dimensional tensile behavior, *Res. Mech.* **18** 25163 (1986).

[52] G.I. Taylor and H. Quinney, The latent heat remaining in a metal after cold working, *Proc. Roy. Soc. London* **A163** 157-181 (1937).

[53] P. Thamburaja and L. Anand, Polycrystalline shape-memory materials: effect of crystallographic texture. *J. Mech. Phys. Solids* **49** 709-737 (2001).

[54] M. Vural, D. Rittel and G. Ravichandran, Large strain mechanical behavior of 1018 cold-rolled steel over a wide range of strain rates, *Metal. Mat. Trans. A* **34A** 2873-2885 (2003).

[55] Y.H. Wang and D.N. Fang, A three-dimensional constitutive model for shape memory alloys, *Int. J. Nonlin. Sc. Num. Sim.* **4** 81-87 (2003).

[56] J.J. Zhu, N.G. Huang, K.M. Liew and Z.H. Zhu, A thermodynamic constitutive model for stress induced phase transformation in shape memory alloys, *Int. J. Sol. Struct.* **39** 741-763 (2002).